PREDICTION OF CUTTING FORCES IN THREE AND FIVE-AXIS BALL-END MILLING WITH TOOL INDENTATION EFFECT

by

OGUZHAN TUYSUZ
B.Sc. Istanbul Technical University, Turkey, 2009

A THESIS SUBMITTED IN PARTIAL FULFILLMENT OF
THE REQUIREMENTS FOR THE DEGREE OF

MASTER OF APPLIED SCIENCE

in

The Faculty of Graduate Studies
(Mechanical Engineering)

THE UNIVERSITY OF BRITISH COLUMBIA
(Vancouver)

January 2012
© Oguzhan Tuysuz, 2012

Abstract

In machining, the desired final shape is created in Computer Aided Design (CAD) environment and this information is forwarded to Computer Aided Manufacturing (CAM) phase in which the toolpath is generated and converted to machine specific commands for part manufacturing. The steps in CAD/CAM environments are geometry dependent only, and do not include the physics of the process. However, mathematical modeling of the machining operation gives the flexibility of identifying and resolving process related issues i.e. tool breakage, chatter vibrations and tolerance violations beforehand, which in turn leads to increased productivity.

The first step of process modeling is to model the mechanics of the operation that leads to the prediction of the cutting forces experienced by the cutting tool and the workpiece. In this study the mechanics of ball-end tool which is commonly used to machine parts with free-form geometric features are studied. The main problem in ball-end milling mechanics is tool indentation which leads to inaccurate force prediction in tool axial direction, and has previously been solved experimentally only for specific cases. This thesis presents a generalized ball-end tool indentation detection and indentation force prediction model for any kind of work material and cutting tool geometry combinations. The static ball-end milling forces with indentation forces are predicted by developing an analytical cutting edge indentation model. The proposed model utilizes indentation mechanics of punch and wedge shape indenters, describes the required conditions for indentation occurrence and evaluates plastic and elastic contact pressures at the cutting edge and workpiece interface using the material properties of the workpiece.

Cutting edge indentation mechanism is also studied through finite element (FE) modeling. A general FE model is obtained for the problem and results are reported only for the material cut in the thesis.

The model proposed in the thesis has been verified experimentally. After integrating the developed indentation force prediction model into the cutting force model, predictions in tool axial direction are improved by 15-40% depending on type of the operation. The contribution of the thesis can be used in cutting force based ball-end milling process optimization and analysis for industrial applications.

Table of Contents

Abstract .... **ii**
Table of Contents .... **iv**
List of Tables .... **vi**
List of Figures .... **vii**
Nomenclature .... **x**
Acknowledgements .... **xvii**
1 Introduction **1**
2 Literature Review **5**
- 2.1 Introduction 5
- 2.2 Cutting Force Models for Three and Five-Axis Ball-End Milling 5
- 2.3 Cutting Tool Indentation in Ball-End Milling and Indentation Modeling 10
- 2.4 Summary 15

3 Mechanics of Ball-End Milling **16**
- 3.1 Introduction 16
- 3.2 Indentation Free Mechanics of Ball-End Milling 17
  - 3.2.1 Ball-End Mill Geometry 17
  - 3.2.2 Mechanics of Three-Axis Ball-End Milling 21
  - 3.2.3 Mechanics of Five-Axis Ball-End Milling 31
- 3.3 Indentation Problem in General Ball-End Milling 40
- 3.4 Summary 45

4 Modeling the Mechanics of Indentation in Ball-End Milling **46**
- 4.1 Introduction 46
- 4.2 Modeling Cutter Indentation for Ball-End Mills with Positive Rake Angle 51
  - 4.2.1 Elastic Contact Pressure Model for Positive Rake Angle Ball-End Cutter 51
  - 4.2.2 Plastic Contact Pressure Model for Positive Rake Angle Ball-End Cutter 60
- 4.3 Modeling Cutter Indentation for Ball-End Mills with Negative Rake Angle 63
  - 4.3.1 Elastic Contact Pressure Model for Negative Rake Angle Ball-End Cutter 64
  - 4.3.2 Plastic Contact Pressure Model for Negative Rake Angle Ball-End Cutter 68

4.4 Effect of Workpiece Temperature on Indentation Models 70
4.5 Integration of Cutting Tool Indentation Model into Cutting Force Model in Three and Five-Axis Ball-End Milling 74
4.6 Summary 79
5 Finite Element (FE) Modeling of Cutting Edge Indentation 80
5.1 Introduction 80
5.2 Finite Element Model of Contact Pressure Due to Cutting Edge Indentation 80
5.2.1 Finite Element Model 81
5.2.2 Calibration of Coefficient *C* for AL7050 86
5.3 Finite Element Model of Workpiece Temperature Rise Due to Cutting Edge Indentation 94
5.4 Summary 98
6 Experimental Verification 100
6.1 Introduction 100
6.2 Exprimental Results 101
6.2.1 Plunge Milling Experiments 101
6.2.2 Three-Axis Inclined Surface Experiments 103
6.2.3 Three-Axis Free-Form Surface Experiment 106
6.2.4 Five-Axis Free-Form Surface (Airfoil) Experiment 109
6.3 Summary 114
7 Conclusions 115
Bibliography 118

List of Tables

Table 3.1: The summary of additional cutting tests with related peak to peak error in F_z for different inclination angles 44

Table 5.1: Details of different meshing strategies used at FE model development stage 82
Table 5.2: Selected feasible range for geometrical quantities 87
Table 5.3: Maximum indentation depths domain for feasible local inclination angles and feed per tooth values 88

Table 6.1: Details of model verification experiments 100
Table 6.2: Specifications of the tool used in verification experiments 100
Table 6.3: Summary of verification experiments results for z-forces 113

List of Figures

Figure 1.1: Sample three-axis sculptured surface ball-end milling toolpath 2
Figure 1.2: Machining process optimization flow chart [7] 3

Figure 2.1: Schematic diagrams of contact for different cases, regenerated from [33] 13
Figure 2.2: Tilted wedge indenter, regenerated from [37] 14

Figure 3.1: Geometry and tool coordinate frame for a ball-end cutter [12] 18
Figure 3.2: Clearance and rake angle of cutting edge element 20
Figure 3.3: Unit outward vector for ball and cylindrical part of the tool 22
Figure 3.4: Flow chart for TWEs extraction and cutting force calculation along a toolpath 27
Figure 3.5: A sample 2D engagement map 28
Figure 3.6: A sample three-axis toolpath segment for free-form surfaces 29
Figure 3.7: (a) Position vectors of two consecutive map points; (b) orientation angle of TCS at MAP_i 30
Figure 3.8: Tool orientation, and TCS and MCS in five-axis ball-end milling 32
Figure 3.9: (a) Linear feed direction and tool axis vector; (b) definition of tool x-axis and linear feed direction 34
Figure 3.10: Orientation of $\left(\boldsymbol{x_T}\right)_i$ and $\left(\boldsymbol{y_T}\right)_i$ after $\left(\mathbf{z_T}\right)_i$ is aligned with Z_M 35
Figure 3.11: (a) Angular motion of the cutter in five-axis ball-end milling; (b) resultant rotation angle, rotation axis and angular speed 37
Figure 3.12: (a) Linear and angular feed components; (b) total feed vector at different z-levels, regenerated from [26] 39
Figure 3.13: Inclined surface ball-end milling experimental setup 40
Figure 3.14: (a) Schematic illustration of upward ramping case (b) comparison of experimental and predicted forces in upward direction inclined surface ball-end milling for following cutting conditions; $\mathrm{R_0 = 8\,mm, \alpha = 15^0}$ $\mathrm{f = 0.1\,mm/rev/tooth, a_p = 4\,mm,\ N = 2,\ n = 4000\,rpm, AL7050\ workpiece}$ 41
Figure 3.15: Two different cases for down-ramping with ball-end cutter, (a) case 1: tool tip is out of cut (back engagement); (b) case 2: tool tip is in cut 42
Figure 3.16: Comparison of experimental and predicted forces for 2 cases of downward direction inclined surface ball-end milling for $\mathrm{R_0 = 8\,mm,\ f = 0.1\,mm/rev/tooth, N = 2}$ $\mathrm{n = 4000\,rpm, AL7050\ workpiece\ \ a)\,\alpha = 45^0, a_p = 2\,mm\ \ \ b)\ \alpha = 30^0,\ a_p = 5\,mm}$ 43
Figure 3.17: Feed components of the tool in inclined surface milling 44

Figure 4.1: Chip thickness distribution in x-z plane, (a) for horizontal feed; (b) for vertical feed 47
Figure 4.2: Shearing and indentation regions on the cutter due to vertical feed 48
Figure 4.3: Max and min indentation values and locations along the cutting flute 48
Figure 4.4: Variation of cutting speed at points close to and at the tool tip 49
Figure 4.5: Variation of the indentation along the cutting flute 50
Figure 4.6: Horizontal $\left(\mathrm{P_o}\right)$ and normal ($\mathrm{P_n}$) planes definitions and cutting edge element at point A 51
Figure 4.7: (a) Cutting edge element for ball-end tool with positive rake angle (b) geometric similarity between inclined punch with rounded edges and cutting edge element 51
Figure 4.8: Punch indentation analogy and cutting edge coordinate system 52
Figure 4.9: Indentation of cutting edge element into workpiece for positive rake angle 53
Figure 4.10: Indentation of inclined punch with rounded corners into material, adapted from [33] 54
Figure 4.11: Indentation related dimensions for both conditions 56
Figure 4.12: Dimensionless elastic contact pressure distribution for punch [33] and cutting edge indentations for; $\mathrm{h_{ind} = 5\,\mu m, R_{edge} = 10\,\mu m, d = 9.5\,\mu m, L = 66.2\,\mu m,}$ nominal $\alpha_n = 5^0$ and AL7050 work material 58
Figure 4.13: Dimensionless pressure distribution due to cutting edge indentation 58
Figure 4.14: Indentation of actual and dummy cutting edges 60
Figure 4.15: General total contact pressure distribution for positive rake angle ball-end cutter.. 62
Figure 4.16: Dimensionless total contact pressure distribution for different edge radii (for each radius $h_{ind} = \left(R_{edge}\right)_{actual}$) and conditions; $\mathrm{R_{edge} = 10\,\mu m, \alpha_n = 5^0, \gamma_n = 12^0}$ $\phi 16\,\mathrm{mm\ ball-end\ cutter}$ and AL7050 workpiece 63
Figure 4.17: Geometrical similarity between a wedge with rounded tip and cutting edge element 64
Figure 4.18: Wedge indentation analogy and cutting edge coordinate system 64
Figure 4.19: Indentation of cutting edge element into workpiece for negative rake angle 65
Figure 4.20: Dimensionless elastic pressure distribution due to cutting edge indentation for different $\left(\mathrm{r}/\left(\mathrm{d_1 + d_2}\right)\right)$ values for; $\mathrm{R_{edge} = 10\,\mu m, \alpha_n = 5^0, \gamma_n = 12^0}$ $\phi 16\,\mathrm{mm\ ball-end\ cutter\ and}$ AL7050 workpiece 68
Figure 4.21: General total contact pressure distribution for negative rake angle ball-end cutter. 69
Figure 4.22: Dimensionless total contact pressure distribution for different indentation depths $\mathrm{R_{edge} = 10\,\mu m, \alpha_n = 5^0, \gamma_n = -12^0,}$ $\phi 16\,\mathrm{mm\ ball-end\ cutter\ and\ AL7050\ workpiece}$ 69
Figure 4.23: An example of workpiece temperature rise distribution under the flank face for; $\mathrm{f = 0.1\,mm/rev/tooth, n = 7000\,rpm, \alpha = 30^0, \alpha_n = 5^0, \gamma_n = 12^0}$ $\phi 16\,\mathrm{mm}$ 2-fluted ball-end cutter and AL7050 workpiece 73
Figure 4.24: Indentation occurrence condition in three-axis ball-end milling 74

Figure 4.25: Indentation occurrence condition in five-axis ball-end milling 75
Figure 4.26: Flow chart for integration of indentation model into three and five-axis cutting force models 77
Figure 4.27: Comparison of experimental and predicted forces for 2 cases of downward direction inclined surface ball-end milling for $R_0 = 8\,\mathrm{mm},\ f = 0.1\,\mathrm{mm/rev/tooth}, \mathrm{N} = 2$ $\mathrm{n} = 4000\,\mathrm{rpm}$, AL7050 workpiece a) $\alpha = 45^0, a_p = 2\,\mathrm{mm}$ b) $\alpha = 30^0,\ a_p = 5\,\mathrm{mm}$ 78

Figure 5.1: A sample meshing strategy for workpiece and dimensions of work material........... 83
Figure 5.2: Dimensionless total contact pressure for AL7050 with one mesh element around edge radius.. 84
Figure 5.3: Dimensionless total contact pressure for AL7050 with two mesh elements around edge radius 84
Figure 5.4: A sample deformation around edge radius; (a) with 1-element quadrilateral mesh (b) with 2-element quadrilateral mesh.. 85
Figure 5.5: Sample FE simulation result for C calibration 89
Figure 5.6: The calibration results for AL7050 extracted from FE simulations.......................... 90
Figure 5.7: Details of FE calibration results for $h_{ind}/R_{edge} = 14$ 91
Figure 5.8: Original FE results and fitted function 93
Figure 5.9: Comparison of FE and analytical total contact pressure distribution for; $h_{ind} = 50\,\mu\mathrm{m},\ \gamma_n = 10^0,\ \alpha_n = 5^0$ 93
Figure 5.10: Comparison of FE and analytical total contact pressure distribution for; $h_{ind} = 50\,\mu\mathrm{m},\ \gamma_n = -15^0,\ \alpha_n = 5^0$ 94
Figure 5.11: FE simulation of workpiece temperature rise for; AL7050, $h_{ind} = 50\,\mu\mathrm{m},\ \gamma_n = 10^0,\ \alpha_n = 10^0$ 96
Figure 5.12: FE workpiece temperature rise results for AL7050 with different cutting edge geometries 96
Figure 5.13: Comparison of workpiece temperature rise for 2 different geometries and materials 97

Figure 6.1: Drilling test workpiece (left) and its 3D CAD model (right) 102
Figure 6.2: Comparison of experimental and predicted cutting forces in the first drilling experiment for; n=3000 rpm, f = 0.04 mm/rev, half hole 20 mm in depth, AL7050 workpiece 102
Figure 6.3: Comparison of experimental and predicted cutting forces in the second drilling experiment for; n=3000 rpm, f = 0.1 mm/rev, half hole 20 mm in depth, AL7050 workpiece 103
Figure 6.4: Inclined plane test surface and workpiece (left), and CAM model of cutting (right) 104

Figure 6.5: Comparison of experimental and predicted cutting forces for; n=4000 rpm, $\alpha = 15^0$ $f = 0.1$ mm/rev/tooth, a_p =5 mm, AL7050 workpiece 105
Figure 6.6: Comparison of experimental and predicted cutting forces for; n=7000 rpm, $\alpha = 30^0$ $f = 0.1$ mm/rev/tooth, a_p =5 mm, AL7050 workpiece 106
Figure 6.7: Three-axis free-form surface cutting test workpiece (left), and CAM model of cutting (right) 107
Figure 6.8: Sample 2D engagement maps for three-axis free-form surface test 108
Figure 6.9: Comparison of experimental and predicted cutting forces for; n=4000 rpm, $f = 0.1$ mm/rev/tooth, $(a_p)_{max} = 6$ mm, AL7050 workpiece.. 108
Figure 6.10: Comparison of experimental and predicted z-forces for; n=4000 rpm, $f = 0.1$ mm/rev/tooth, $(a_p)_{max} = 6$ mm, AL7050 workpiece... 109
Figure 6.11: Variation of tool orientation angles along the toolpath... 110
Figure 6.12: Five-axis airfoil surface cutting test workpiece (left), and CAM model of cutting (right) 110
Figure 6.13: Sample 2D engagement maps for five-axis airfoil surface test............................. 111
Figure 6.14: Comparison of experimental and predicted cutting forces for; (a) first pass (b) second pass (c) third pass (d) fourth pass, for; n=4000 rpm, $f = 0.1$ mm/rev/tooth, $(a_p)_{max} = 4$ mm, AL7050 workpiece.. 112

Nomenclature

a_p	axial depth of cut
a	thermal diffusivity of work material
A_q	(no subscript) material dependent coefficient in non-linear cutting force coefficient models, (q=1…6) coefficients in curve fitting
b_c	width of cut in milling
b	projected length of total indentation length, half width of rounded apex for symmetrical wedge
c	projected length of indentation of straight part in punch indentation
c_p	specific heat
C	the constant characterizes the onset of plastic flow
dz	height of differential element defined along the cutter axis
dF_q	(q=r,t,a) differential radial, tangential and axial milling cutting forces, (q=x,y,z) differential milling cutting forces in Cartesian coordinates
db	projected length of an differential cutting flute in the direction along the cutting velocity
dS	length of an differential element defined along the cutting flute
d	projected length of rounded part of cutting edge in punch indentation
D	tool diameter
E	Young's modulus
f(x)	the function defining the shape of punch indenter
f	feed per tooth

$\boldsymbol{f}_v$	linear vertical feed per tooth vector
$\boldsymbol{f}_\mathrm{h}$	linear horizontal feed per tooth vector
$\left(\boldsymbol{f}_{tot}\right)_i$	the total feed/tooth vector of the cutter in five-axis ball-end milling at i^{th} engagement map
$\left(\boldsymbol{f}_v\right)_{indentation}$	vertical feed per tooth vector contributing to indentation
$\left(\boldsymbol{f}_v\right)_{\mathrm{shear}}$	the portion of the vertical feed per tooth contributing to chip generation
$\left(\mathbf{f}_{\mathbf{L}}\right)_i$	the linear feed direction vector at i^{th} engagement map
$\left(\mathbf{f}_{\mathbf{Lu}}\right)_i$	the unit linear feed direction vector at i^{th} engagement map
$\left(\boldsymbol{f}_L\right)_i$	the linear feed per tooth vector at i^{th} engagement map
$\mathrm{F}_{\mathrm{ind}}$	indentation force in tool axial direction
F	linear feed speed
$\left(\mathbf{F}_{\mathbf{L}}\right)_{\mathbf{i}}$	linear feed vector at i^{th} engagement map
$\left(\mathbf{F}_{\mathbf{A}}\right)_{\mathbf{i}}$	angular feed vector in five-axis ball-end milling at i^{th} engagement map
$\left(\mathbf{F}_{\mathbf{T}}\right)_{\mathbf{i}}$	total feed vector in five-axis ball-end milling at i^{th} engagement map
$\left\|\mathrm{F}_{\mathrm{z}}\right\|$	the prediction error in z-forces
h	uncut chip thickness
$\mathrm{h}_{\mathrm{ind}}$	indentation depth
i_0	nominal helix angle of ball-end tool
i	local helix angle in ball part of ball-end tool, toolpath segment or engagement map number

$\mathbf{i}, \mathbf{j}, \mathbf{k}$	unit vectors in principal directions x,y,z
j	flute number
$\mathbf{k}_\mathbf{i}$	rotation axis vector in five-axis tool kinematics at i^{th} engagement map
K_{qc}	(q=r,t,a) radial, tangential and axial milling cutting force coefficients
K_{qe}	(q=r,t,a) radial, tangential and axial milling edge force coefficients
K_0	modified zero order Bessel Function of second kind
K_{ind}	indentation force coefficient (indentation force per unit cutting edge length)
L_{ind}	edge length in cut in mechanistic indentation model
m	cutter dependent coefficient in non-linear cutting force coefficient models
m_T, m_R	empirical constants in empirical cutting force models
n	spindle speed
$\mathbf{n}$	unit outward vector
N	total number of teeth in the cutter
p	contact pressure
L	projected length straight part of cutting edge in punch indentation
L_s	length of shear plane
$\mathbf{P}$	position vector of tool tip in machine coordinate system
$\mathbf{P}_\mathbf{f}$	the position vector representing a point on the flute
P_o	horizontal plane in which cutting edge element is define
P_n	normal plane in which cutting edge element is define
q_{pl}	the heat generation intensity of shear plane heat source

r_c	chip compression ratio
R_{edge}	cutting edge radius
R_0	radius of cylindrical part of ball-end tool
R	local tool radius in ball part of ball-end tool
$\left(\boldsymbol{T}_{\boldsymbol{Trans}}\right)_{\boldsymbol{i}}$	tool coordinates system translation vector from i^{th} to $(\mathrm{i}+1)^{\mathrm{th}}$ engagement map
$\left(\boldsymbol{T}_{\boldsymbol{rot_z}}\right)_{\boldsymbol{MCS\rightarrow TCS_i}}$	the first rotation matrix between machine tool and tool coordinate systems in five-axis tool kinematics at i^{th} engagement map
$\left(\boldsymbol{T}_{\boldsymbol{Rot}}\right)_{\boldsymbol{i}}$	tool coordinates system rotation vector from i^{th} to $(\mathrm{i}+1)^{\mathrm{th}}$ engagement map
$\left(\boldsymbol{T}_{\boldsymbol{TCS_i\rightarrow MCS}}\right)$	transformation matrix that transforms tool coordinate system to machine tool coordinate system at i^{th} engagement map
$\left(\boldsymbol{T}_{\boldsymbol{rot_{xy}}}\right)_{\boldsymbol{i}}$	the second rotation matrix between machine tool and tool coordinate systems in five-axis kinematics at i^{th} engagement map
$v(x)$	normal surface displacements
V_c	cutting speed
V_s	shear velocity
x_E, y_E, z_E	coordinate axes defining the cutting edge coordinate system
x_T, y_T, z_T	coordinate axes defining the cutter coordinate system
X_M, Y_M, Z_M	coordinate axes defining the machine tool coordinate system
z_{flute}	axial coordinate on the flute
$z_{parabola}$	axial coordinate on the parabolic indentation variation

$\mathbf{z_T}$	unit tool axis orientation vector
$(\times)$	cross product of vectors
$(\bullet)$	dot product of vectors
$[\ ]^{-1}$	matrix inverse operator
Δd_i	distance between $\mathrm{i^{th}}$ and $(\mathrm{i}+1)^{\mathrm{th}}$ engagement maps
Δt_i	estimated elapsed time $\mathrm{i^{th}}$ and $(\mathrm{i}+1)^{\mathrm{th}}$ engagement maps
$\Delta\theta_i$	resultant tool orientation angle in five-axis tool kinematics
$\Delta \mathrm{y}$	rigid body displacement
$\Delta \mathrm{T}$	temperature rise
$\Delta \mathrm{W}$	the work done during plastic deformation
$\Delta \mathrm{Q}$	the generated heat due to plastic deformation
α	inclination angle of inclined surfaces
α_{w}	tilt angle of asymmetrical wedge shape indenter
α_{o}	radial clearance angle defined in $\mathrm{P_o}$
α_{n}	normal clearance angle defined in $\mathrm{P_n}$
β_{a}	friction angle
β_{n}	normal friction angle
γ_{o}	radial rake angle defined in $\mathrm{P_o}$
γ_{n}	normal rake angle defined in $\mathrm{P_n}$
$(\gamma_{\mathrm{o}})_{\mathrm{cylindrical}}$	radial rake angle in the cylindrical part of ball-end tool
η	side angle of symmetrical wedge shape indenter

η_p	percent of the plastic work converted to heat
η_c	chip flow angle
θ	tool reference angle
θ_T	tool tilt angle
θ_L	tool lead angle
κ	axial immersion angle of ball-end cutter
λ_s	cutting edge inclination angle
λ	thermal conductivity
τ_s	shear stress
ϕ	rotation angle of the cutter
ϕ_p	pitch angle of the cutter
ϕ_c	shear angle
ϕ_{st}, ϕ_{ex}	radial start and exit angles in milling
φ	inclination angle of shear plane heat source
Φ	the angle between linear feed and unit cutter axis orientation vectors
ν	Poisson's ratio
ξ	indentation limit angle in punch indentation
ρ	density
σ_Y	yield strength of the work material
σ, ε	the true stress and strain
ψ	lag angle

ω_i	angular speed at i^th^ engagement map
Ω_i	orientation angle of tool coordinate system at i^th^ engagement map
CAD	Computer Aided Design
CAM	Computer Aided Manufacturing
FE	Finite elements
TWE	Tool-workpiece engagement
B-rep	Boundary representation
HB	Brinell hardness
TCS	Tool coordinate system
MCS	Machine tool coordinate system
STL	Streolithography
NC	Numerical control
CL	Cutter location
ISO	International Organization for Standardization
LSF	Linear shape function
QSF	Quadratic shape function

Acknowledgements

I would like to start sincerely stating my lifelong gratitude to my supervisor Dr. Yusuf Altintas for his guidance, support and sharing his research experience with me during the course of my studies. This work would not have been accomplished without his inspiration, patience and invaluable wisdom. Therefore, it was my pleasure to be a member of Manufacturing Automation Laboratory (MAL) and complete my MASc study under his supervision.

I would like to thank my co-supervisor Dr. Steve Feng for his time and effort throughout my studies and motivating me at the most stressful moments.

I also would like to thank to the NSERC CANRIMT for the financial support, Sandvik Coromant for generously providing the ball-end mills, and Machine Tools Technologies Research Foundation (MTTRF) for loaning Mori Seiki NMV5000 CNC machining center.

It was an invaluable experience to work in MAL with professional, helpful, friendly and brilliant colleagues. While doing research in a world popular international environment, we, all MAL members had too many precious memories. I would like to thank to all of my friends for their support, constructive discussions and friendship.

Lastly, and most importantly, I wish to thank to my parents; my dear mother Hulya, my dear father Mehmet and my dear elder brothers M.Ali and Fatih for allowing me to be as ambitious as I wanted and supporting me from the bottom of their hearts. Feeling their absolute confidence in me has always kept me motivated and helped me to become a capable individual. Also, I wish to express my special thanks to my friend Tugce for supporting me throughout this study.

I would like to dedicate this work to my family.

1 Introduction

Recent functionality requirements have led to development of components with varying free-form features. Sculptured surfaces have free-form features with both convex and concave regions that can be geometrically fitted by ball-end cutter. The parts with free from geometric features are generally machined using ball-end cutters, which are used to manufacture parts in die/mold, aerospace, biomedical and automotive industries where both part quality and manufacturing time are metrics for high productivity.

The ultimate goal of virtual machining process research is to identify process related issues and solve them before the costly physical trials in the shop. Modeling the process mathematically is necessary to achieve that goal in a reasonable amount of time, and the first step of process modeling is to model the mechanics of the operation that leads to the prediction of the cutting forces experienced by the cutting tool and the workpiece.

Although the generalized models in literature can predict cutting forces in x-y plane reasonably well, they cannot predict cutting force in tool axis (z) direction in the presence of tool indentation. The axial force component is significant for cutting force based process optimization, machining accuracy, and chatter stability prediction (depending on configuration of the machine tool). However, the axial forces are underestimated [1], [2], [3] or not even considered [4] using the existing cutting force models. Therefore, it is required to accurately model the axial force component including the tool indentation to complete the circle for force prediction in ball-end milling and to have a general predictive force model for any kind of machining conditions.

Ball-end cutter generates irregular and mostly random shape surfaces in free-form machining as shown Figure 1.1. The associated NC toolpaths consist of many straight and inclined segments. The indentation effect especially becomes important in machining inclined surface segments where the tool tip region contributes significantly to engagement of the cutter with the work material.

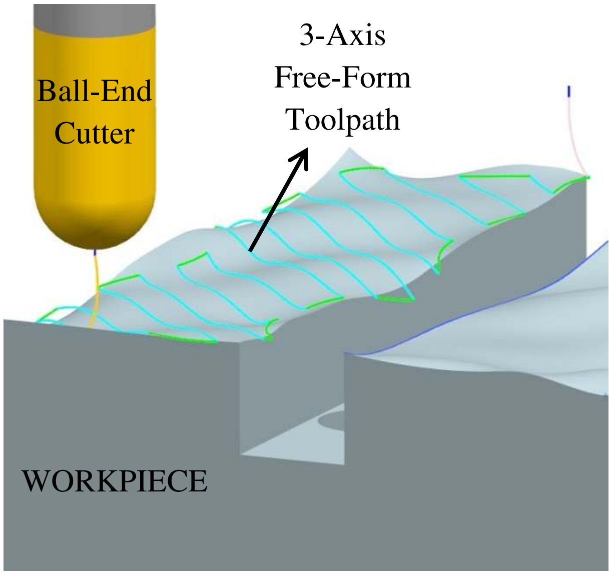

Figure 1.1: Sample three-axis sculptured surface ball-end milling toolpath

When the vibrations and run-out of the cutter are neglected, the tool axis is collinear with rotation axis of the spindle; which causes the ball-end mill to experience zero surface speed at the very tip due to its geometry. When the surface speed is zero, the cutting edge indents to the material as opposing to plastic shearing in regular metal cutting operations.

Although there are some studies published in literature that address the indentation problem in ball-end milling, a sound mechanics model has not been developed. The indentation effect has been either mechanistically modeled by calibrating empirical force constants from a series of cutting tests by assuming constant indentation force along the entire flute [1], or an analogy between cutting flute indentation and hardness tests has been made [5], [6]. Both methods require extensive amount of cutting or indentation tests to fine tune empirical constants without providing the mathematical model of the physical process.

The objective of this thesis is to develop a predictive model that calculates the effect of indentation on three and five-axis ball-end milling mechanics. The model needs to identify the conditions at which indentation takes place, and a fine separation between the indentation and shearing mechanisms must be made in order to predict ball-end milling forces accurately. The improved ball-end milling force model is later used in the simulation and improvement of productivity in the machining of parts with free form surfaces as outlined in [7]. The flow chart of productivity improvement (process optimization) through machining process simulation is shown in Figure 1.2.

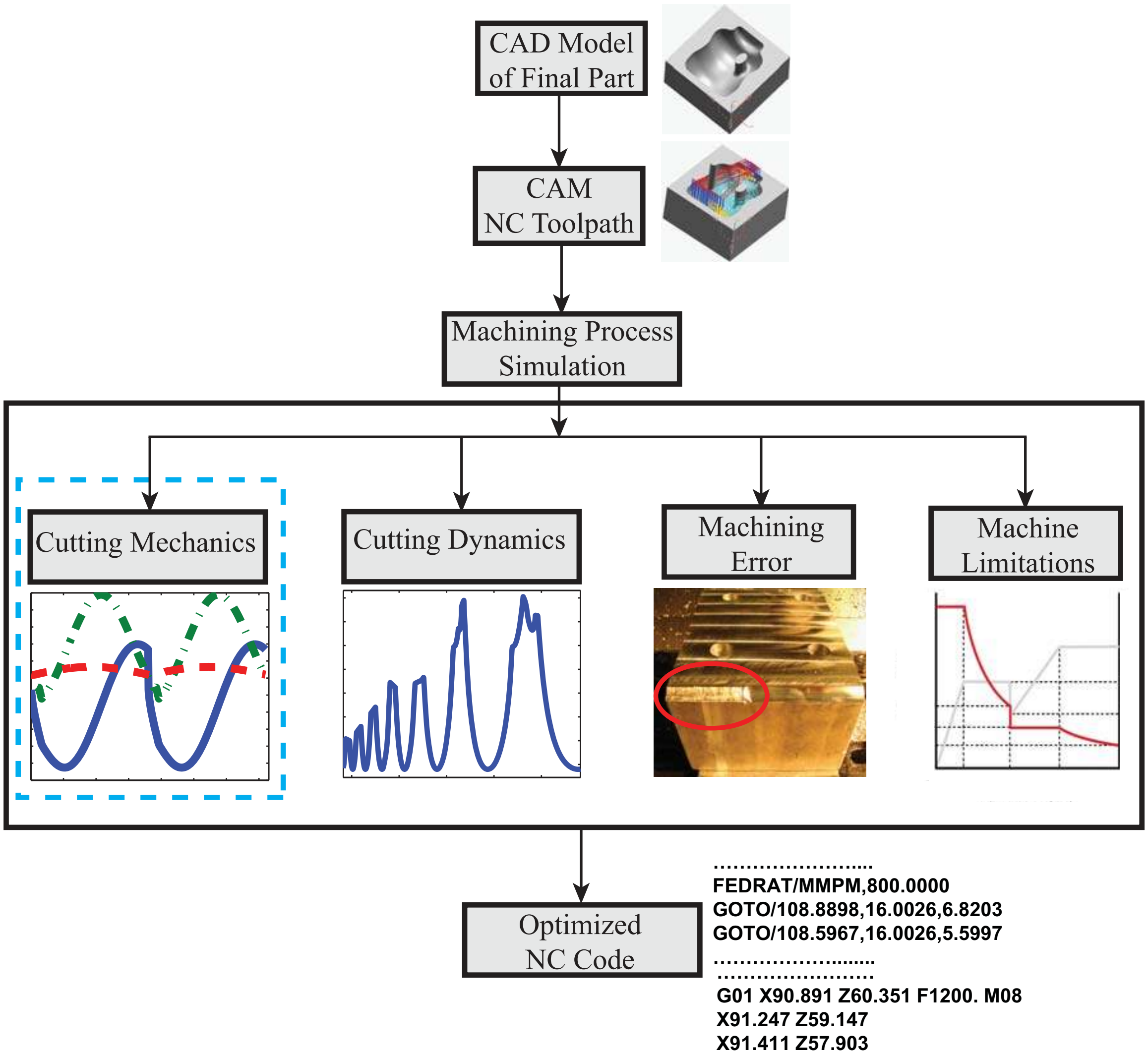
CAD Model of Final Part
CAM NC Toolpath
Machining Process Simulation
Cutting Mechanics
Cutting Dynamics
Machining Error
Machine Limitations
Optimized NC Code

```
........................
FEDRAT/MMPM,800.0000
GOTO/108.8898,16.0026,6.8203
GOTO/108.5967,16.0026,5.5997
........................
........................
G01 X90.891 Z60.351 F1200. M08
X91.247 Z59.147
X91.411 Z57.903
```

Figure 1.2: Machining process optimization flow chart [7]

This thesis is organized as follows: the related literature is reviewed in Chapter 2. The existing three and five-axis ball-end milling cutting force models with generalized chip thickness calculation are presented in Chapter 3. A novel indentation force calculation and indentation detection model both for three and five-axis ball-end milling operations is developed in Chapter 4. Chapter 5 presents the Finite Element (FE) simulations carried out to obtain a material dependent indentation constant. The FE results are also compared against the analytical results obtained from the model in Chapter 4. The experimental verification of developed model both for three and five-axis ball-end milling applications is given in Chapter 6. Conclusions and future research directions are given in Chapter 7.

2 Literature Review

2.1 Introduction

The importance of accurate modeling the mechanics of ball-end milling was discussed, and challenge in prediction of the axial force component; especially for the case of free-form surface milling was explained for improved cutting force prediction and the optimization of machining operations.

This chapter reviews the literature in the mechanics of ball end milling operations to justify the complimentary contributions of the thesis. Current cutting force models for three and five-axis ball-end milling are reviewed in Section 2.2 by classifying the models regarding the cutting in horizontal and inclined planes, and in free-form surfaces. Attempts to take the tool indentation into account in ball-end milling force prediction, and the indentation models employed in this thesis are presented in Section 2.3. In Section 2.3, the indentation models in available literature are classified regarding the indenter geometries i.e. punch and wedge shaped indenters. The chapter is concluded with a brief summary of the literature by Section 2.4.

2.2 Cutting Force Models for Three and Five-Axis Ball-End Milling

The main purpose of the cutting force prediction is to avoid tool breakage and tolerance violations before the actual operation. The prediction of cutting forces in milling applications has been studied by several researchers, and goes back to the late 1920s [7]. Cutting force prediction models require material and cutter geometry dependent force coefficients that are obtained from cutting tests. Mechanistic identification models can obtain cutting coefficients for specific cutting conditions, tool geometry and work material. Altering any of these parameters requires the force identification procedure to be repeated [8]. Sabberwal and Koenigsberger [9] used mechanistic model and expressed cutting forces as follows;

$$\begin{aligned} F_{\text{Cutting Force}} &= K\,a_p h \\ K &= A\,h^m \end{aligned} \tag{2.1}$$

where, $K\ (\mathrm{N/mm^2})$ is the cutting pressure, a_p (mm) is the depth of cut, h (mm) is uncut chip thickness, and A and m are material and cutter dependent coefficients.

Armerego [10], classified the forces as cutting (shearing) and edge (ploughing) forces, and expressed them as,

$$F_{\text{Total}} = \underbrace{K_c\,a_p h}_{\text{Cutting Force}} + \underbrace{K_e\,a_p}_{\text{Edge Force}} \tag{2.2}$$

where, K_c and K_e are cutting and edge force coefficients that can either be obtained by mechanistic model, or using the orthogonal to oblique transformation model [11]. In orthogonal to oblique transformation model, the material's shear stress, friction coefficient and shear angle are obtained from orthogonal cutting tests, and transformed to oblique cutting geometry using the geometry of the cutting tool. Thus, the orthogonal to oblique transformation model is much more general than the mechanistic approach, and hence it is used in this thesis.

The generalized geometric and mechanics models for ball-end cutter using the orthogonal to oblique transformation were developed by Lee and Altintas [12], and Engin and Altintas [13]. They [12] analytically evaluated the chip load based on Martelotti's approach [14] for constant lead cutters, and divided the tool into axial disc elements of height (*dz*) where orthogonal to oblique transformation is implemented. In the uncut chip thickness calculation, the circular toolpath assumption was made rather than using the exact milling kinematics. The model was verified only with horizontal plane ball-end milling experiments; however most of the ball-end milling applications are three dimensional, and it was not tested for three dimensional cases.

Researchers studied the inclined surface milling. Feng et al. [15], [16], [17] analytically calculated the tool-workpiece engagement (TWE) conditions and used the empirical uncut chip thickness-cutting force relationships that require several cutting tests at calibration stage. The empirical relationships between uncut chip thickness and differential cutting forces (*dF*) in tangential and radial directions are,

$$\begin{aligned} dF_T &= K_T\, t^{m_T} dz \\ dF_R &= K_R\, t^{m_R} dz \end{aligned} \tag{2.3}$$

where, K_T , K_R , m_T and m_R are empirical constants and obtained from horizontal slot cutting tests. However, notably in downward direction ball-end milling the magnitude of the force in tool axis direction is higher than that of forces in x-y plane, the force component in tool axial direction was ignored in the model. Ikua et al. [18], [19] considered the actual toolpath of the cutting edges while evaluating the uncut chip thickness, and predicted the forces in three Cartesian coordinates by just considering radial and tangential forces. Although, they machined convex and concave surfaces, they did not study the force prediction errors in z-direction. Fontaine et al. [20] modeled inclined surface ball-end milling forces utilizing the thermo-mechanical properties of the work material with tool run-out effect. Only upward direction cutting results were considered; hence, they did not report any problem in cutting force prediction in z-direction. In another study, Tsai et al. [5], [6] presented a geometry based force model by considering the effect of tool indentation onto cutting forces. They made an analogy between hardness test and tool indentation, and directly lumped the indentation force into z-direction.

Higher functionality requirements from machined parts have pushed researchers to predict cutting forces for relatively complex curved and free-form surfaces as well. Guzel et al. [1] developed a TWE calculation module for three-axis ball-end milling using z-map method, and evaluated the cutting forces in all three orthogonal coordinates using the model given in [12] with mechanistic force coefficients. The authors [1] recognized a remarkable discrepancy between measured and predicted forces in z-direction and represented this error by a mechanistically calibrated constant pressure over the workpiece while the cutter is moving downward. Lamikiz et al. [21] and Sun et al. [22] adapted the force model proposed in [12] for ball-end milling of sculptured surfaces. Researchers either relaxed the circular toolpath assumption [22], or performed a coordinate transformation so as to consider both feeding direction and slope effects [21] on chip load calculation for inclined segments of the toolpath. Merdol [7] developed virtual three-axis process simulation and optimization models for general end mills. In their models, the NC toolpath of the milling operation is specified as input, and cutting forces are obtained by explicit evaluation of integral equations in the force model given in [12] using the TWE information extracted along the toolpath via commercially available CAM verification software VeriCut®. In the model verification phase of [7], they noticed the less accuracy in z-forces with ball-end cutters and reported the discrepancy. In one study, Zeroudi et al. [3] extended the thermo-mechanical oblique cutting model of Fontaine [20] to ball-end milling of sculptured surface. Attention was drawn to the discrepancy between measured and predicted forces at start and end sections of the toolpath, and the error in z-direction forces was attributed to lack of edge force coefficients in calculations. However, the error observed in z-direction was about 35% which cannot be caused only by edge forces, and may be attributed to the indentation effect caused by the surface profile of the workpiece.

Present literature for three-axis ball-end milling do not adequately describe the error observed in z-direction, and researchers who realized the inaccuracy in predictions either calibrated the error directly from cutting tests or attributed the error to some other factors. The thesis is thus aims to fill this gap.

Five-axis ball-end milling mechanics is relatively newer than three-axis applications, and there have been few efforts to model it. One of the first five-axis ball-end milling force prediction studies was carried out by Clayton et al. [23] using mechanistically identified force coefficients. The authors discretized the cutting flute in spherical coordinates rather than in tool axial direction, and limited their model to the cases where certain cutting conditions and the cutter geometries are included in the neural network used at calibration stage. The cutting forces in all three Cartesian coordinates were predicted for a concave surface; but they did not experience a remarkable error in z-forces since they avoided contact of tool tip region. In another study, Fussel et al. [24] used discretized model for both the workpiece and the cutter to calculate TWE. They employed a discrete mechanistic force model that expresses cutting pressures as nonlinear functions of chip thickness by ignoring the edge forces. Their model was tested on a sinusoidal surface without considering z-forces; however, due to sinusoidal shape of the toolpath, the indentation phenomenon is quite important while the tool moves downward depending on the tool orientation. An analytical TWE calculation module for five-axis ball-end milling was introduced by Ozturk and Budak [25], and this module was used in the cutting force model with the force coefficients identified by orthogonal to oblique transformation. Many combinations of tool lead and tilt angles were tested in the experiments; however in the case of negative lead angle, the z-forces were under-predicted; since tool tip region indentation contributed to the forces. The five-axis flank milling force prediction model with tapered ball-end tool was proposed by Ferry [26] who considered the effect of extra degrees of freedom of the five-axis process on process mechanics for the first time. The model was tested on five-axis flank milling of impeller blades, and a drastic error in axial direction forces was obtained that was attributed to indentation of the tool tip region. One of the most recent studies in prediction of cutting forces in five-axis ball-end milling was carried out by Dongming et al. [27]. The researchers calculated the

TWE using Z-map method and the chip load considering the exact tool motion. The cutting forces were predicted employing the mechanistic force model, and the model was tested on horizontal and sinusoidal surfaces. In the horizontal surface experiments any negative tool lead angle that characterizes the tool indentation was not used as in [25], and in sinusoidal surface experiments the tool tip region remained out of cut. As a result, they did not experience any indentation problem. In another study, Boz and Lazoglu [28] also worked on five-axis ball-end milling force prediction using a B-rep based engagement calculation algorithm, and the mechanistic force model ignoring the effect of additional rotational degrees of freedom on process mechanics. The authors predicted cutting forces only in x-y plane; thus no indentation problem was reported.

In the available literature, modeling the indentation phenomenon which is the main goal of this work has been considered by few researchers [1], [5], [6], and these studies are detailed in Section 2.3 in order to demonstrate the need for a comprehensive cutter indentation model. Also, models for some classical indentation geometries that are used to model cutter indentation in Chapter 4 are introduced.

2.3 Cutting Tool Indentation in Ball-End Milling and Indentation Modeling

Guzel et al. [1] preferred to experimentally model the ball-end tool indentation by assuming a constant indentation force acting in z-direction along the entire cutting edge. Several cutting tests for a specific cutting tool-workpiece couple were conducted to characterize the behavior of the tool during downward movement at inclined segments of the toolpath. Also, the effect of vertical feed was included in calibration process by selecting a certain range for feedrate in the tests. In the experimental model, the difference between measured and predicted forces in z-direction was named as indentation forces, and was expressed as a function of vertical feedrate using a linear fitting as follows [1],

$$\frac{\mathrm{F_{ind}}}{\mathrm{L_{ind}}} = 0.3\left(\text{Vertical Feedrate}\right) + 4.5 \tag{2.4}$$

where, F_{ind} is the constant indentation force (N/mm) per unit edge length, and L_{ind} is the edge length (mm) in cutting. Using the empirical calibration (Eq. (2.4)) validation tests were conducted on different type of surfaces i.e. inclined flat, sinusoidal and ellipse shaped surfaces. Although the predictions matched well with measured forces for inclined flat surfaces that were used in calibration tests as well, under-prediction occurred in sinusoidal and ellipse shaped surface ball-end milling tests.

The main drawbacks of this model [1] can be listed as follows: due to the mechanistic nature of the model, it is only valid for the calibrated tool-workpiece couple, and feedrate range used in the calibration tests. Whenever one of these parameters is altered, the behavior of the tool indentation cannot be predicted. Also, constant indentation force assumption leads to the constant indentation depth along the cutting edges, and does not give the variation of the indentation force along the flute as the force is lumped even at the points where indentation does not take place. Due to the spherical shape of the cutter, indentation and related deformations occur in radial direction of the cutter; however this model directly lumps them in z-direction. Clearly, this is not a general model, and its performance is limited to calibration tests conditions. The model can be generalized by conducting calibration tests for numerous tool-workpiece couples, and cutting conditions; but that is impractical as it requires enormous amount of cutting tests to create this database.

The model proposed in [5], [6] geometrically explains the indentation problem; but does not give the physical reason behind it. The model directly lumps the indentation force into z-direction and expresses this force using the analogy between Brinell hardness test and cutting edge indentation as [6],

$$F_{ind} = HB\ \pi\ L_{ind}^2 \tag{2.5}$$

where, F_{ind} is the indentation force, HB is the Brinell hardness of the work material, and L_{ind} is the length of indentation along the cutting edge. This model treats the indentation of the cutting edge as indentation of sphere (as in Brinell hardness test); however the indentation takes place over the cutting edge not on the tool envelope. Also, the Brinell hardness of the materials is determined with certain force and indenter diameter ratios that are specified by ISO standards [29]. Therefore, when force and the indenter diameter ratio in cutting falls out of the range defined by [29] for a specific material, then the tabulated HB values do not characterize the actual indentation case.

In the light of previous studies summarized above, [1], [5], [6] are not general in nature; therefore this work is intended to complete the missing part in ball-end milling mechanics by treating the physical phenomenon of cutting edge indentation as equivalent to traditional penetration of punch and wedge geometries. By utilizing the indentation mechanics of these geometries a general analytical tool indentation model for ball-end milling is developed as explained in detail in Chapter 4. In the remainder of this section, the contact models for punch and wedge elements with sharp and rounded corners and tip are briefly introduced.

The analytical contact model for punch geometries have been studied by many researchers [30], [31], [32], [33], [34] under plane strain conditions. Johnson [30] solved the elastic contact pressure problem for a flat punch with sharp (square) corners, with and without friction, and showed how the pressure distribution over the contact area has singularity at both ends of the contact zone. Jaeger [31], [32] looked into solutions for two dimensional (2D) contact profiles with and without rounded corners. Rounded corner can be assumed analogues to the edge radius in cutting edge indentation. The linear superposition of contact pressure results in linear elasticity was used in order to obtain the elastic contact pressure distribution for punch and wedge geometries. The solution for flat punch with one square and one rounded edge was derived. Linear superposition of this result with flat punch with sharp corners led to the solution for indentation of rounded wedge. Also, indentation pressure for flat punch with rounded corners was solved using the superposition of two mirrored flat punches with one sharp and one rounded corner, and a flat punch with sharp corners. The solutions in these articles [31], [32] were limited to elastically similar indenters and indented materials, and the results were supported by finite element simulations for the mentioned circumstances. As shown in Figure 2.1, Goryacheva et al. [33] developed a general model that can handle any contact case regarding the contacting portions of a tilted punch with rounded corners which is similar to the problem investigated in this work.

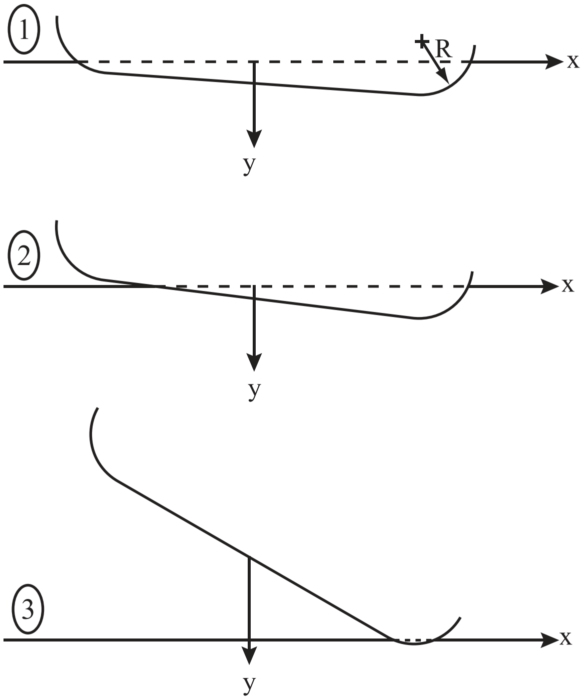

Figure 2.1: Schematic diagrams of contact for different cases, reproduced from [33]

The analytical expression for elastic contact pressure was derived for with and without friction conditions. It was also shown that, the contact pressure is asymmetrical for the cases given in Figure 2.1. Depending on the cutting flute geometry, the edge indentation problem can be treated as either punch or wedge penetration. Hence, the wedge indentation models available in literature are introduced in the following paragraphs.

2D indentation of wedge geometry has been attracting the attention of the researchers as its indentation is not a Hertzian contact. Truman et al. [35] investigated the mechanics of wedge and cone shaped elastic indenters. The pressure expression had a singularity at the tip (apex) of the wedge geometry due to the change in surface profile slope. It was shown that, only elastic contact cannot be obtained with the indentation of sharp tip wedge geometry. Following up this work, Ciavarella [36] extended the discussion to the rounded tip geometry for frictionless conditions. The contact was characterized by Hertzian when the rounded part forms the majority of the contact, and by wedge while the indentation of the straight part is dominant. In another study, Sackfield et al. [37] inclined the wedge geometry with sharp tip so as to obtain elastic contact pressure distribution for an asymmetrical wedge (wedge with unequal side angles, $\left(\eta+\alpha_w\right) \neq \left(\eta-\alpha_w\right)$) as shown in Figure 2.2. The contact pressure was derived for frictionless conditions. It was proved that the singularity in pressure distribution is still present.

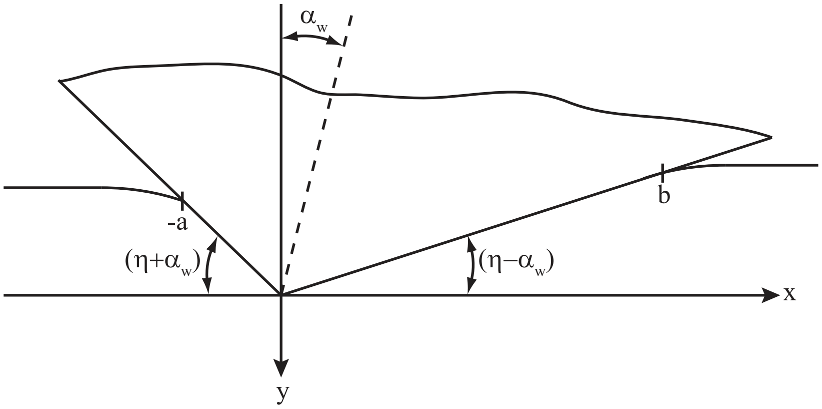

Figure 2.2: Tilted wedge indenter, regenerated from [37]

Since the infinite elastic pressure value cannot exist, Dini et al. [38] proposed a corrective term that can be used for any indentation problem involving pressure singularity. The idea depends on the linear superposition of elastic solutions. Once the singular pressure distribution is obtained, the singularity is simply removed by adding this corrective term to the pressure distribution expression.

In this thesis, a new ball-end milling cutting force model that considers indentation effect of tool tip region is developed. In the model, indentation of punch and wedge geometries are utilized in order to evaluate contact pressure at the interface of cutting edge and the workpiece. The details of the model are given in Chapter 4.

2.4 Summary

In this chapter, previous studies for modeling the three and five-axis ball-end milling mechanics, the challenges in force prediction especially in tool axial direction have been reviewed. Also, the past attempts to take the tool indentation into account in cutting force prediction, and indentation mechanics for certain geometries have been discussed. The force model used for three and five-axis ball-end milling in this thesis is detailed in the following chapter.

3 Mechanics of Ball-End Milling

3.1 Introduction

Machining productivity is mostly limited by the mechanics (cutting forces) and dynamics (chatter stability) of cutting operations. Mechanics of end milling operations have been studied by many researchers in the past [39], [40], [41], [12], [42], [13]. Commonly used mechanistic (or semi-mechanistic) models obtain the material dependent, empirical force coefficients from cutting tests, and employ them to predict cutting forces. The existing cutting force models for ball-end milling are capable of predicting forces in x-y plane for generic conditions; but they under-predict the force component in tool's axial (z) direction while the tool moves downward on the inclined toolpath segments encountered in free-form surface milling. This chapter introduces the cutting force models for three and five-axis ball-end milling, and to point out necessity of an improved cutting force model that can accurately predict cutting forces at any type of cutting conditions.

The mechanics of three and five-axis ball-end milling based on the previous studies [12] and [26] with a general chip load calculation are presented. The required tool-workpiece engagements (TWEs), which lead to the prediction of chip thickness distribution along the cutting edges are extracted from MACHpro-Virtual Machining System developed at UBC. Realizing the shortcomings of existing force models, the contribution of indentation to the total cutting forces is experimentally illustrated to justify the need for a new cutting force model that considers the indentation forces experienced by the cutter.

3.2 Indentation Free Mechanics of Ball-End Milling

3.2.1 Ball-End Mill Geometry

The generalized geometric model for ball-end mill was presented by Lee and Altintas [12], and Engin and Altintas [13]. The ball-end mill has both spherical and cylindrical body, and the cutting edges are usually helical as shown in Figure 3.1. The helix, rake and lag angles at the hemispherical section vary due to increasing diameter along its axis. End mills, in general, are ground either with a constant helix or constant lead. Throughout this thesis, the cutter with constant lead is taken as a base model. According to the geometrical model [12],

$$x^2 + y^2 + \left(R_0 - z\right)^2 = R_0^2 \tag{3.1}$$

where R_0 is the radius of cylindrical part of the tool and (x,y) are coordinates of the point on the flute in x-y plane as illustrated in Figure 3.1(a). Due to the helix angle, the points on a flute do not contact with the work material at the same time. Depending on the type of helix angle, time lag or lead occurs between the tool tip and the points along the cutting flute. The angle that considers lag/lead at axial position *z* is given by,

$$\psi\left(z\right) = \frac{z \tan i_0}{R_0}, \qquad \frac{\tan i_0}{R_0} = \frac{\tan i(z_1)}{R(z_1)} = \frac{\tan i(z_2)}{R(z_2)} = ... = \frac{\tan i(z_i)}{R(z_i)} = \text{Constant} \tag{3.2}$$

where, $R(z_i)$ and $i(z_i)$ are local cutter radius and local helix angle, respectively.

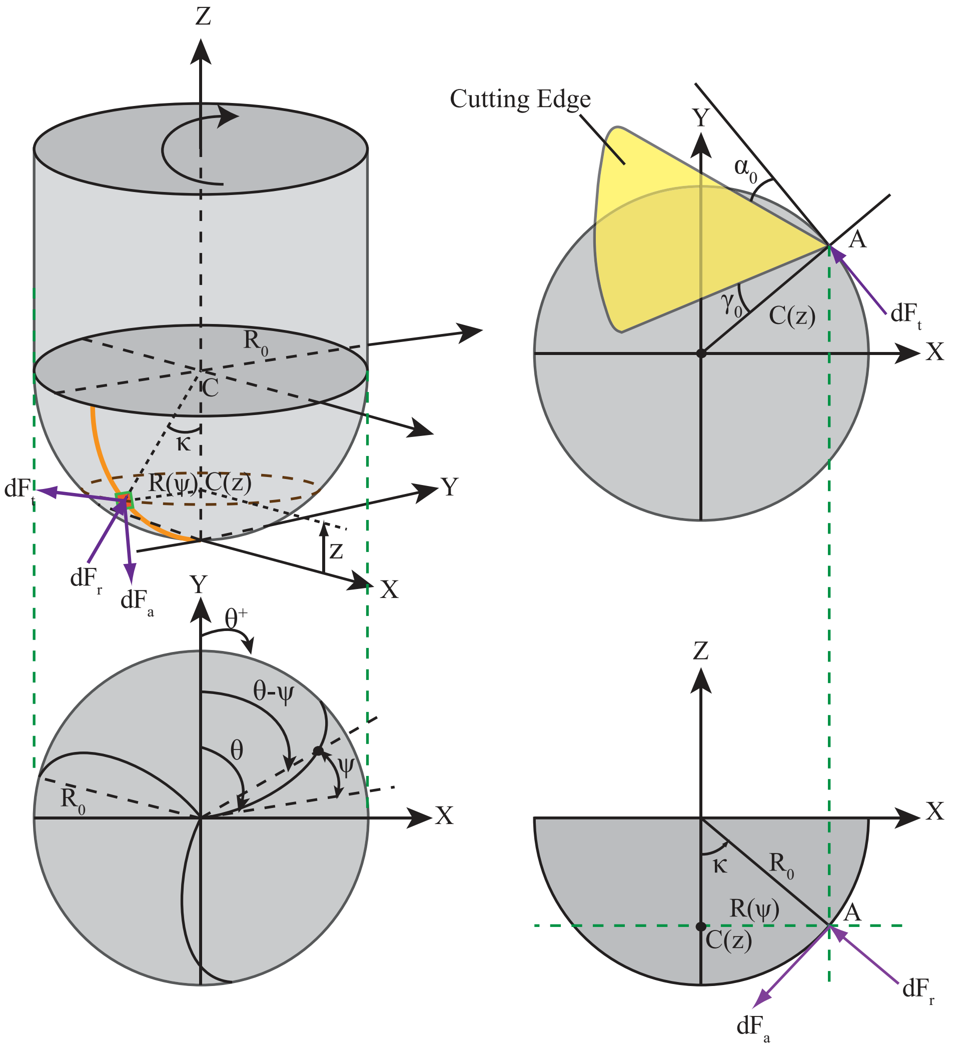
Z
R_0
C
κ
R(ψ), C(z)
dF_t
dF_r
dF_a
Y
Z
X
Y
θ+
θ-ψ
θ
ψ
R_0
X
Cutting Edge
Y
α_0
A
γ_0
C(z)
dF_t
X
Z
X
κ
R_0
R(ψ)
A
C(z)
dF_r
dF_a

(a) (b)

Figure 3.1: Geometry and tool coordinate frame for a ball-end cutter [12]

As seen in Eq.(3.2), the sign of the helix angle determines whether the points along the cutting edge lag or lead. The local cutter radius (R) and local helix angle (i) can be evaluated as follows,

$$R(z)=\begin{cases} R_0\sqrt{1-\left(1-\dfrac{z}{R_0}\right)^2} & \text{, for ball part} \\ R_0 & \text{, for cylindrical part} \end{cases} \tag{3.3}$$

$$i(z)=\begin{cases} \tan^{-1}\left(\dfrac{R(z)}{R_0}\tan i_0\right) & \text{, for ball part} \\ i_0 & \text{, for cylindrical part} \end{cases} \tag{3.4}$$

Once the flutes wrap around the cutter envelope, the position of a point on the flute can be expressed in cylindrical coordinate frame. If the tool tip is selected as the coordinate center (Figure 3.1), the position vector representing a point on the flute is,

$$\boldsymbol{P}_f(z) = R(z)\left[\sin\left(\psi(z)\right)\boldsymbol{i} + \cos\left(\psi(z)\right)\boldsymbol{j}\ \right] + R_0\,\psi(z)\cot i_0\,\boldsymbol{k} \tag{3.5}$$

where, $\boldsymbol{i}$, $\boldsymbol{j}$ and $\boldsymbol{k}$ are unit vectors for three orthogonal axes of tool coordinate system (TCS) shown in Figure 3.1. Since milling is an intermittent operation, angular position of flutes need to be known to check whether the flute is in or out of the cut at any instant. The angular position (immersion angle) of a point on cutting flute j at elevation z is evaluated in x-y plane in TCS as follows,

$$\phi_j(z) = \theta + (j-1)\,\phi_p - \psi(z) \tag{3.6}$$

where, θ and ϕ_p are rotation angle of the reference flute and pitch angle of the cutter, respectively. θ is positive in clockwise direction and measured form y-axis in TCS. The pitch angle defines how close the flutes are spaced in angular direction, and determined for N fluted cutter as,

$$\phi_p = \begin{cases} \dfrac{2\pi}{N} & , \quad \text{for uniform pitch cutters} \\ \phi_{p,j} & , \quad \text{for non-uniform pitch cutters} \end{cases} \tag{3.7}$$

The radial position (axial immersion angle) of a point on cutting flute j at elevation z is calculated as follows,

$$\kappa(z) = \sin^{-1}\left(\frac{R(z)}{R_0}\right) \tag{3.8}$$

Ideally, a flute is composed of infinite number of cutting edge elements, and each element has a different orientation while wrapping around the tool envelope. As shown in Figure 3.2, the orientation of cutting edge element is defined by rake and clearance angles. These angles can be defined either in horizontal or normal plane, and they are named as radial or normal angles depending on which plane they are defined in [43].

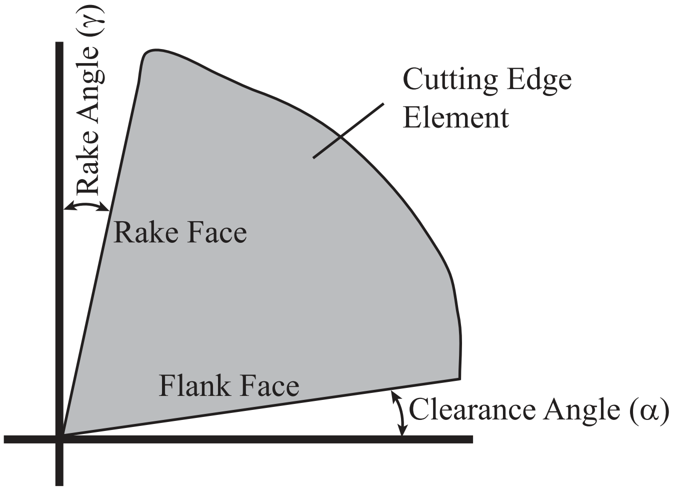

Figure 3.2: Clearance and rake angle of cutting edge element

Since normal rake angle is related to radial rake angle via inclination angle of cutting edge, the variation of normal rake angle at ball-part of the cutter can be expressed as [44],

$$\tan\gamma_n(z) = \tan\gamma_o(z)\cos i(z) \tag{3.9}$$

where, local inclination angle of cutting edge element can be taken as local helix angle (i) of the ball-end cutter [44]. Also, the radial rake angle of ball-end mill vary along tool axis in the ball part as [25],

$$\gamma_o(z) = \begin{cases} (\gamma_o)_{cylindrical}\sin\left(\kappa(z)\right) & \text{, for ball part} \\ (\gamma_o)_{cylindrical} & \text{, for cylindrical part} \end{cases} \tag{3.10}$$

Having introduced the geometrical model for ball-end mill, the semi-mechanistic cutting force model for three-axis ball-end milling is given in following section.

3.2.2 Mechanics of Three-Axis Ball-End Milling

The verified semi-mechanistic cutting force model proposed in [12] for helical ball-end mills is used throughout this study. In the model, forces are classified as cutting (shearing) and edge (ploughing) forces. In order to consider the effect of change in cutter geometry on process mechanics, the cutter is axially discretized and contribution of each axial element is summed to obtain the total cutting forces acting in radial, tangential and axial directions. The differential forces in radial, tangential and axial directions are expressed by,

$$dF_{i,j}(\phi) = K_{ic}(z)h_j\left(\phi, z\right)db(z) + K_{ie}(z)dS(z) \tag{3.11}$$

where, i is the index for direction of the force ($i = r, t, a$), j denotes the flute number ($j = 1....N$). $K_{ic}\left(\mathrm{N/mm^2}\right)$ is cutting force coefficient for shearing, and $K_{ie}\left(\mathrm{N/mm}\right)$ is edge force coefficient for ploughing. $h_j\left(\phi, z\right)$ is the instantaneous uncut chip thickness generated by j^{th} flute and measured in surface normal direction of the cutter. *db(z)* corresponds to the chip width in oblique cutting and *dS(z)* is the curved length of differential cutting flute. The resultant forces in Cartesian coordinates are obtained by introducing the transformation matrix $\mathbf{T}_{\mathrm{rta}\rightarrow\mathrm{xyz}}$,

$$\begin{gathered}\left\{dF_{xyz,j}\left(\phi\right)\right\} = \left[T_{rta\rightarrow xyz}\right]\left\{dF_{rta,j}\left(\phi\right)\right\}\\ \begin{Bmatrix} dF_{x,j}\left(\phi\right) \\ dF_{y,j}\left(\phi\right) \\ dF_{z,j}\left(\phi\right) \end{Bmatrix} = \begin{bmatrix} -\sin\left(\kappa(z)\right)\sin\left(\phi_j(z)\right) & -\cos\left(\phi_j(z)\right) & -\cos\left(\kappa(z)\right)\sin\left(\phi_j(z)\right) \\ -\sin\left(\kappa(z)\right)\cos\left(\phi_j(z)\right) & \sin\left(\phi_j(z)\right) & -\cos\left(\kappa(z)\right)\cos\left(\phi_j(z)\right) \\ \cos\left(\kappa(z)\right) & 0 & -\sin\left(\kappa(z)\right) \end{bmatrix} \begin{Bmatrix} dF_{r,j}\left(\phi\right) \\ dF_{t,j}\left(\phi\right) \\ dF_{a,j}\left(\phi\right) \end{Bmatrix}\end{gathered} \tag{3.12}$$

In order to obtain the individual contribution of each flute *j*, the differential cutting forces acting on discretized elements along a flute are summed between lower $z_{1,j}$ and upper $z_{2,j}$ axial engagement limits as,

$$\left\{F_{xyz,j}(\phi)\right\} = \int_{z_{1,j}}^{z_{2,j}} \left\{dF_{xyz,j}(\phi)\right\} dz \tag{3.13}$$

The total cutting forces acting on the cutter in x-y-z directions are obtained by summing the contribution of each flute,

$$\left\{F_{xyz}(\phi)\right\} = \sum_{j=1}^{N} \left\{F_{xyz,j}(\phi)\right\} \tag{3.14}$$

For ball-end tools, the uncut chip thickness varies both in radial and axial directions as,

$$h_j(\phi, z) = f \sin(\phi(z)) \sin(\kappa(z)) \tag{3.15}$$

where, f is feed per tooth value (mm/tooth/rev).

Alternatively, Merdol et al. [45] evaluated uncut chip thickness by projecting the feed per tooth vector onto unit outward vector of the cutter. The projection is carried out using dot product of the vectors. The unit outward vector for ball and cylindrical parts are different as shown in Figure 3.3, and they can be expressed as,

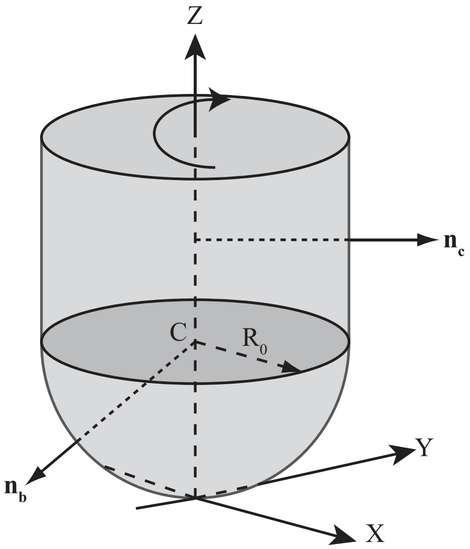

Figure 3.3: Unit outward vector for ball and cylindrical part of the tool

$$\boldsymbol{n(z)} = \begin{cases} \dfrac{R(z)\sin(\phi_j)}{R_0}\boldsymbol{i} + \dfrac{R(z)\cos(\phi_j)}{R_0}\boldsymbol{j} + \dfrac{\left(z - R_0\right)}{R_0}\boldsymbol{k} & \text{, for ball part} \\ \dfrac{R_0\sin(\phi_j)}{R_0}\boldsymbol{i} + \dfrac{R_0\cos(\phi_j)}{R_0}\boldsymbol{j} = \sin(\phi_j)\boldsymbol{i} + \cos(\phi_j)\boldsymbol{j} & \text{, for cylindrical part} \end{cases} \tag{3.16}$$

The uncut chip thickness can be obtained by projecting the feed motion vector of the tool onto unit outward vector at each point along cutting flutes as,

$$h_j(\phi, z) = \left(\boldsymbol{f}_L\right)_{\boldsymbol{TCS}} \bullet \boldsymbol{n(z)} \tag{3.17}$$

where, $\left(\boldsymbol{f}_L\right)_{\boldsymbol{TCS}}$ is the feed per tooth vector of the tool in TCS and expressed using its unit vector,

$$\left(\boldsymbol{f}_L\right)_{\boldsymbol{TCS}} = f\left(\boldsymbol{f}_{Lu}\right)_{\boldsymbol{TCS}} \tag{3.18}$$

Eq.(3.17) is employed throughout the thesis to calculate cutting forces in Eq.(3.11).

Chip width term, *db(z)*, in Eq.(3.11) can be found using differential cutting edge height *dz* and axial immersion angle $\kappa(z)$ as,

$$db(z) = \frac{dz}{\sin\left(\kappa(z)\right)} \tag{3.19}$$

The curved length of differential cutting edge element is calculated using Eq.(3.2) and Eq.(3.5) as follows,

$$\left.\begin{aligned} dS(z) &= \left\| d\boldsymbol{P}_f(z) \right\| = \sqrt{\left(R'(\psi)\right)^2 + \left(R(\psi)\right)^2 + R_0^2\cot^2 i_0}\, d\psi \\ R'(\psi) &= \frac{-R_0\left(\psi\cot i_0 - 1\right)\cot i_0}{\sqrt{1 - \left(\psi\cot i_0 - 1\right)^2}} \\ d\psi &= dz\frac{\tan\beta_0}{R_0} \end{aligned}\right\} \tag{3.20}$$

The cutting force model requires force coefficients which can be obtained either from mechanistic approach [46] or orthogonal to oblique transformation [8]. In the mechanistic approach, several cutting tests are conducted for specific tool and cutting conditions, and cutting force coefficients are calibrated using experimental force data. In the orthogonal to oblique transformation method, the cutting force coefficients are obtained from orthogonal cutting tests for a range of geometrical parameters of the tool and cutting conditions. Orthogonal coefficients are transformed to oblique cutting force coefficients using the geometry and material properties of the work material. Since the mechanistic approach is only valid for tested tool and work material pair, the latter method is a general approach and used throughout the thesis.

Using tangential force $\left(F_t\right)$, feed force $\left(F_f\right)$, chip compression ratio $\left(r_c\right)$ and rake angle $\left(\gamma_0\right)$ the shear stress $\left(\tau_s\right)$, the shear angle $\left(\phi_c\right)$ and the friction angle $\left(\beta_a\right)$ are obtained from orthogonal cutting tests as follows;

$$\tau_s = \frac{F_t \cos\phi_c - F_f \sin\phi_c}{\left(\dfrac{b_c h}{\sin\phi_c}\right)}, \quad \phi_c = \tan^{-1}\left(\frac{r_c \cos\gamma_0}{1 - r_c \sin\gamma_0}\right), \quad \beta_a = \gamma_0 + \tan^{-1}\left(\frac{F_f}{F_t}\right), \quad r_c = \frac{h}{h_c} \tag{3.21}$$

where, h_c is cut chip thickness. Orthogonal cutting tests are conducted for a series of cutting conditions (cutting speed V_c and chip thickness h) and tool geometries (rake angle γ_o). The parameters $\left(\tau_s\right), \left(\phi_c\right)$ and $\left(\beta_a\right)$ are expressed as functions of V_c, h and γ_o for each material type. The orthogonal cutting force coefficients can be expressed as,

$$\begin{aligned} K_{tc} &= \tau_s \frac{\cos\left(\beta_a - \gamma_0\right)}{\sin\phi_c \cos\left(\phi_c + \beta_a - \gamma_0\right)} \\ K_{fc} &= \tau_s \frac{\sin\left(\beta_a - \gamma_0\right)}{\sin\phi_c \cos\left(\phi_c + \beta_a - \gamma_0\right)} \end{aligned} \tag{3.22}$$

where, $K_{tc}\left(\text{N/mm}^2\right)$ and $K_{fc}\left(\text{N/mm}^2\right)$ are tangential and feed force coefficients respectively. Once the orthogonal coefficients are found, they can be transformed into oblique cutting using the approach proposed by Budak et al.[11] as,

$$
\begin{aligned}
K_{tc} &= \frac{\tau_s}{\sin\phi_n}\frac{\cos\left(\beta_n-\gamma_n\right)+\tan i\tan\eta_c\sin\beta_n}{\sqrt{\cos^2\left(\phi_n+\beta_n-\gamma_n\right)+\tan^2\eta_c\sin^2\beta_n}} \\
K_{rc} &= \frac{\tau_s}{\sin\phi_n\cos i}\frac{\sin\left(\beta_n-\gamma_n\right)}{\sqrt{\cos^2\left(\phi_n+\beta_n-\gamma_n\right)+\tan^2\eta_c\sin^2\beta_n}} \\
K_{ac} &= \frac{\tau_s}{\sin\phi_n}\frac{\cos\left(\beta_n-\gamma_n\right)\tan i+\tan\eta_c\sin\beta_n}{\sqrt{\cos^2\left(\phi_n+\beta_n-\gamma_n\right)+\tan^2\eta_c\sin^2\beta_n}}
\end{aligned}
\tag{3.23}
$$

where, sub-index n denotes oblique (normal) value of corresponding parameter. Using Stabler's chip flow rule [47], the chip flow angle η_c can be assumed to be equal to the local helix angle i. Also, the orthogonal shear angle is assumed to be equal to normal shear angle $\left(\phi_c \equiv \phi_n\right)$.

Since the local geometry of ball-end mill varies at the spherical section, the local values of geometric parameters have to be used in Eq.(3.23). Local helix and normal local rake angle can be evaluated from Eq.(3.4) and Eq.(3.9), respectively. Local normal friction angle is calculated as,

$$
\beta_n(z) = \tan^{-1}\left(\tan\beta_a\cos i(z)\right) \tag{3.24}
$$

The Eq.(3.23) can be re-written as follows;

$$
\begin{aligned}
K_{tc}(z) &= \frac{\tau_s}{\sin\phi_n}\frac{\cos\left(\beta_n(z)-\gamma_n(z)\right)+\tan i(z)\tan\eta_c(z)\sin\beta_n(z)}{\sqrt{\cos^2\left(\phi_n+\beta_n(z)-\gamma_n(z)\right)+\tan^2\eta_c(z)\sin^2\beta_n(z)}} \\
K_{rc}(z) &= \frac{\tau_s}{\sin\phi_n\cos i}\frac{\sin\left(\beta_n(z)-\gamma_n(z)\right)}{\sqrt{\cos^2\left(\phi_n+\beta_n(z)-\gamma_n(z)\right)+\tan^2\eta_c(z)\sin^2\beta_n(z)}} \\
K_{ac}(z) &= \frac{\tau_s}{\sin\phi_n}\frac{\cos\left(\beta_n(z)-\gamma_n(z)\right)\tan i(z)+\tan\eta_c(z)\sin\beta_n(z)}{\sqrt{\cos^2\left(\phi_n+\beta_n(z)-\gamma_n(z)\right)+\tan^2\eta_c(z)\sin^2\beta_n(z)}}
\end{aligned}
\tag{3.25}
$$

Edge force coefficients $\left(K_{te},K_{re}\right)$ are calibrated from cutting experiments for workpiece-cutter pairs, and transformed to oblique cutting. Since there is no force component in axial direction in orthogonal cutting, the axial edge force coefficient $\left(K_{ae}\right)$ is assumed to be zero, and transformation of $\left(K_{ae}\right)$ gives zero axial edge force coefficient in oblique cutting. Since the value of $\left(K_{ae}\right)$ is known to be very small in oblique cutting, the transformation does not affect the accuracy of oblique force prediction [44].

The cutting force model is applied to three-axis free-form toolpaths in the following section.

In ball-end milling, the engagement conditions between the cutter and the work material determines the chip thickness, the angles at which the cutter enters $\left(\phi_{st}\right)$ and leaves the cutting zone $\left(\phi_{ex}\right)$ at each axial level along the cutter axis. These geometric parameters are used to calculate cutting forces at each tool rotation angle using Eq. (3.14).

Extracting tool-workpiece engagements (TWEs) off-line is not within the scope of this study, and it is obtained from the commercially available software MACHpro-Virtual Machining System developed at the Manufacturing Automation Laboratory at UBC. The point where TWE is calculated called map point (MAP). Once the streolithography file (STL) of the blank geometry and NC toolpath are given as inputs, MAP information is obtained at user defined sampled points and stored in .xml file as shown in Figure 3.4. Also, further steps for cutting force calculation are shown in Figure 3.4.

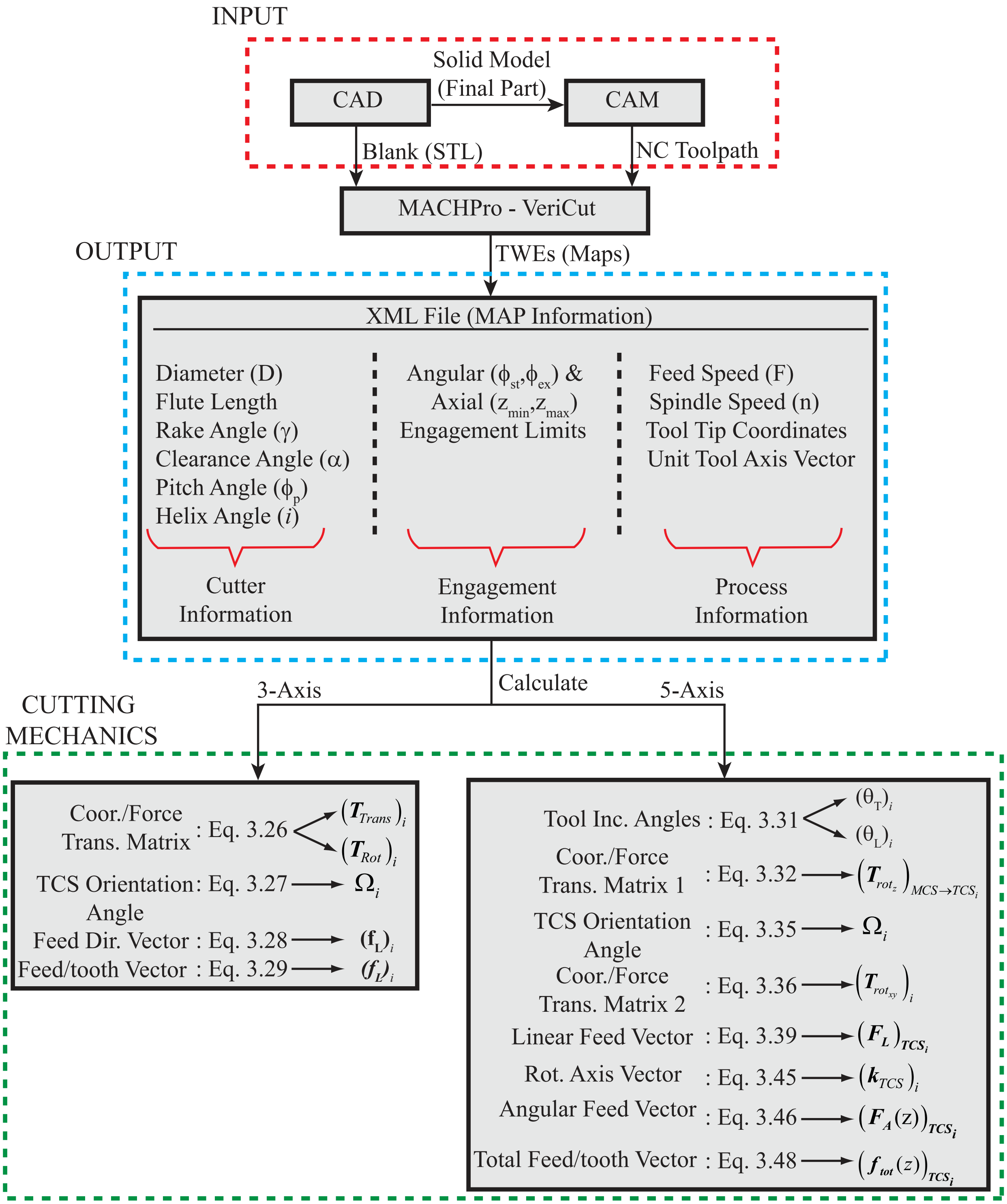
INPUT
Solid Model
(Final Part)
CAD
CAM
Blank (STL)
NC Toolpath
MACHPro - VeriCut
OUTPUT
TWEs (Maps)
XML File (MAP Information)
Diameter (D)
Flute Length
Rake Angle (γ)
Clearance Angle (α)
Pitch Angle (ϕ_p)
Helix Angle (i)
Angular (ϕ_{st},ϕ_{ex}) &
Axial (z_{min},z_{max})
Engagement Limits
Feed Speed (F)
Spindle Speed (n)
Tool Tip Coordinates
Unit Tool Axis Vector
Cutter
Information
Engagement
Information
Process
Information
Calculate
3-Axis
5-Axis
CUTTING
MECHANICS
Coor./Force
Trans. Matrix : Eq. 3.26
$(T_{Trans})_i$
$(T_{Rot})_i$
TCS Orientation: Eq. 3.27 Ω_i
Angle
Feed Dir. Vector : Eq. 3.28 $(f_L)_i$
Feed/tooth Vector : Eq. 3.29 $(f_L)_i$
Tool Inc. Angles : Eq. 3.31
$(\theta_T)_i$
$(\theta_L)_i$
Coor./Force
Trans. Matrix 1 : Eq. 3.32 $(T_{rot_z})_{MCS \to TCS_i}$
TCS Orientation
Angle : Eq. 3.35 Ω_i
Coor./Force
Trans. Matrix 2 : Eq. 3.36 $(T_{rot_{xy}})_i$
Linear Feed Vector : Eq. 3.39 $(F_L)_{TCS_i}$
Rot. Axis Vector : Eq. 3.45 $(k_{TCS})_i$
Angular Feed Vector : Eq. 3.46 $(F_A(z))_{TCS_i}$
Total Feed/tooth Vector : Eq. 3.48 $(f_{tot}(z))_{TCS_i}$

Figure 3.4: Flow chart for TWEs extraction and cutting force calculation along a toolpath

In MACHpro, the 3D engagement on the cutter is represented by rectangles in angular and axial engagement domains in 2D, and the angular engagement boundaries for each rectangle along the cutter axis are given as demonstrated in Figure 3.5.

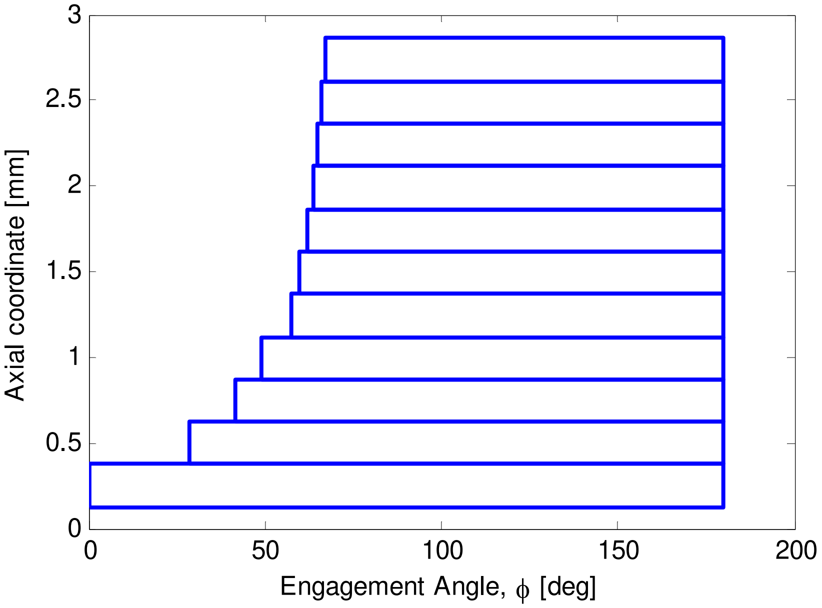

Figure 3.5: A sample 2D engagement map

For free-form surfaces, a sample toolpath segment and movements of cutter between map points are shown in Figure 3.6. $X_M Y_M Z_M$ represents machine (fixed) coordinate system (MCS) and $(x_T)_i - (y_T)_i - (z_T)_i$ represents tool coordinate system at i^{th} map point (TCS_i). As shown in Figure 3.6, the feed direction vector $(\mathbf{f_L})_i$ at each map point stays in $(x_T)_i$ - $(z_T)_i$ plane, and the motion of the cutting tool between map points is approximated by linear segments. This approximation holds true for three-axis milling in which the toolpath is approximated by small linear segments by machine tool interpolator. Furthermore, as long as the sampling distance is kept as small as possible, the error introduced by small linear segments approximation becomes negligible.

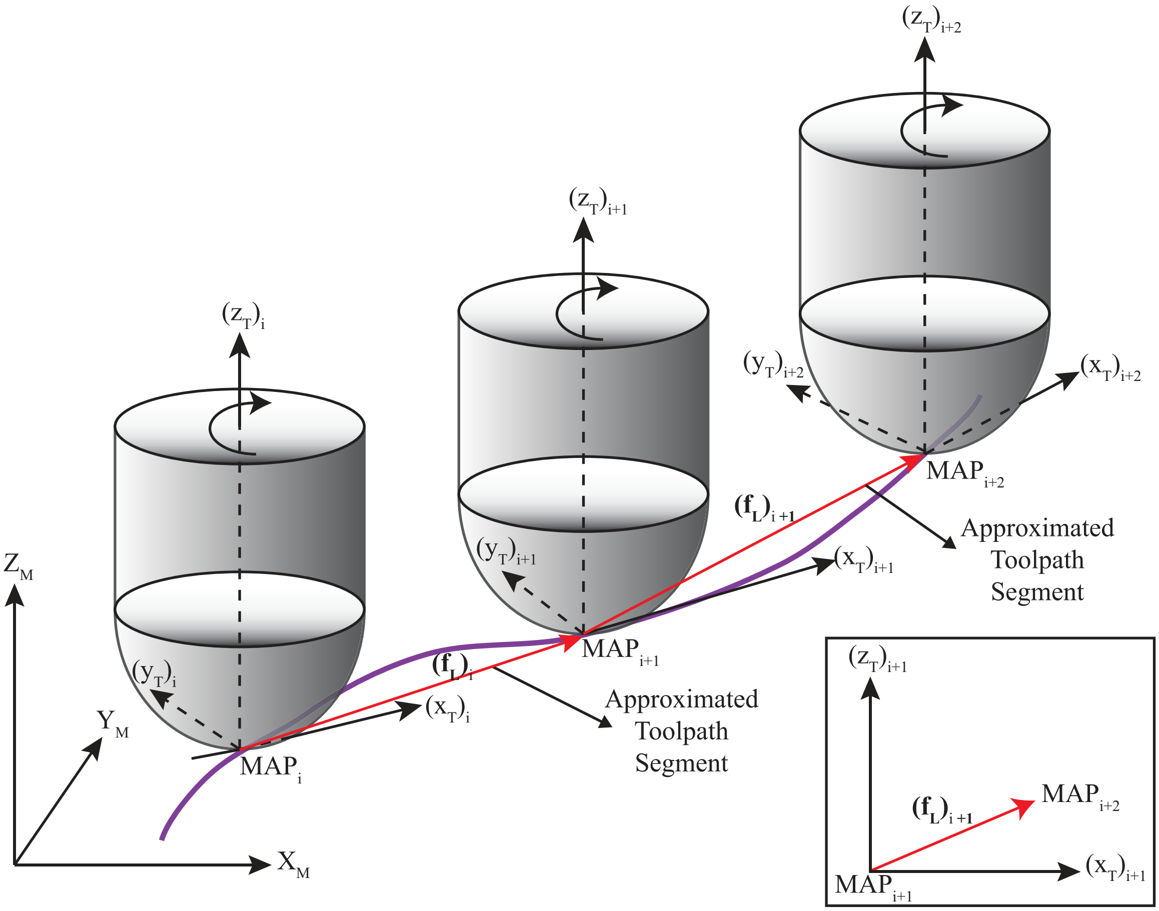
(z_T)_{i+2}
(z_T)_{i+1}
(z_T)_i
(y_T)_{i+2}
(x_T)_{i+2}
MAP_{i+2}
(f_L)_{i+1}
Approximated Toolpath Segment
(y_T)_{i+1}
(x_T)_{i+1}
Z_M
MAP_{i+1}
(f_L)_i
(y_T)_i
Y_M
(x_T)_i
Approximated Toolpath Segment
MAP_i
X_M
(z_T)_{i+1}
(f_L)_{i+1}
MAP_{i+2}
MAP_{i+1}
(x_T)_{i+1}

Figure 3.6: A sample three-axis toolpath segment for free-form surfaces

Calculation of the cutting forces along three axis toolpath is similar, except that, some parameters i.e. engagement conditions, coordinate transformation matrices, TCS orientation with respect to MCS, feed/tooth vector, have to be calculated at each map point as they change along the path (Figure 3.4). Coordinate transformation matrices can be evaluated as,

$$\begin{gathered}
\left(T_{Trans}\right)_i = \begin{bmatrix} X_{i+1}-X_i \\ Y_{i+1}-Y_i \\ Z_{i+1}-Z_i \end{bmatrix} \\
\left(T_{Rot}\right)_i = \begin{bmatrix} \cos(\Omega_i) & \sin(\Omega_i) & 0 \\ -\sin(\Omega_i) & \cos(\Omega_i) & 0 \\ 0 & 0 & 1 \end{bmatrix}
\end{gathered} \tag{3.26}$$

where, X_i, Y_i, Z_i are tooltip coordinates in MCS, $\left(T_{Trans}\right)_i$ translates MCS to TCS_i and also gives the feed direction vector $\left(\mathbf{f}_L\right)_i$ at MAP_i in MCS. Ω_i represents the orientation angle of TCS_i with respect to MCS as shown in Figure 3.7.

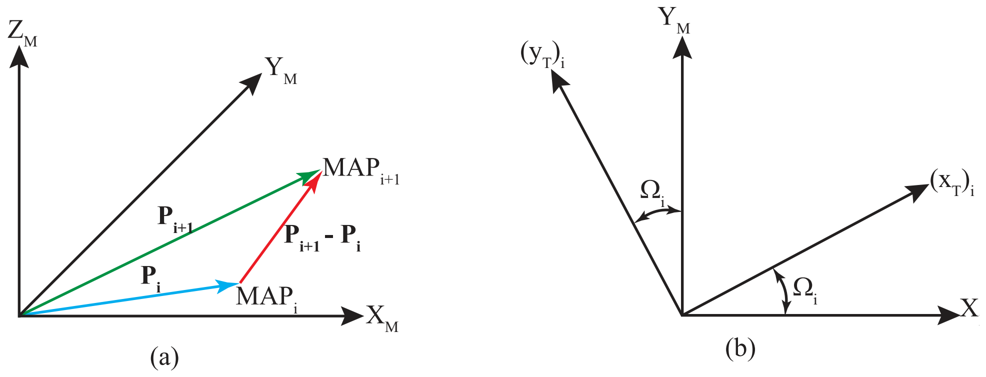

Figure 3.7: (a) Position vectors of two consecutive map points; **(b)** orientation angle of TCS at MAP_i

As position vectors of MAP_i and $\text{MAP}_\text{i+1}$ are known in MCS, Ω_i can be expressed by,

$$\Omega_i = \tan^{-1}\left[\frac{\left(\boldsymbol{P}_{i+1} - \boldsymbol{P}_i\right)_Y}{\left(\boldsymbol{P}_{i+1} - \boldsymbol{P}_i\right)_X}\right] \tag{3.27}$$

where, indices X and Y denotes coordinates of tool tip displacement vector in MCS. The feed direction vector from MAP_i to $\text{MAP}_\text{i+1}$ in TCS_i can be expressed as,

$$\left(\mathbf{f}_L\right)_i = \left(T_{Rot}\right)_i \left(T_{Trans}\right)_i = x_i\,\boldsymbol{i}_{TCS} + y_i\,\boldsymbol{j}_{TCS} + z_i\,\boldsymbol{k}_{TCS} \tag{3.28}$$

where, $\boldsymbol{i}_{TCS}$, $\boldsymbol{j}_{TCS}$ and $\boldsymbol{k}_{TCS}$ are unit vectors of TCS_i, and feed/tooth vector in TCS_i can be written as,

$$\left(\boldsymbol{f}_L\right)_i = f_i\left(\mathbf{f}_{Lu}\right)_i = \frac{f_i}{\sqrt{\left(\text{x}_\text{i}\right)^2 + \left(y_\text{i}\right)^2 + \left(z_\text{i}\right)^2}}\left(\mathbf{f}_L\right)_i = f_{x_i}\boldsymbol{i}_{TCS} + f_{y_i}\,\boldsymbol{j}_{TCS} + f_{z_i}\,\boldsymbol{k}_{TCS} \tag{3.29}$$

where, $\left(\mathbf{f}_{Lu}\right)_i$ is unit feed direction vector and f_i is feed/tooth value (mm/rev/tooth).

The chip thickness at each map point is calculated by substituting Eq.(3.29) into Eq.(3.17), and the cutting forces are calculated at each MAP_i using Eqs.(3.11), (3.12), (3.13), (3.14) and the engagement information. These forces can be transformed into a fixed coordinate frame for comparison purpose. When the fixed coordinate system is selected as MCS, the transformation can be carried out by,

$$\begin{aligned} \left(T_{TCS_i \to MCS}\right) &= \begin{bmatrix} \cos(\Omega_i) & -\sin(\Omega_i) & 0 \\ \sin(\Omega_i) & \cos(\Omega_i) & 0 \\ 0 & 0 & 1 \end{bmatrix} \\ \left\{F_{xyz}(\phi)\right\}_{MCS} &= \left(\boldsymbol{T}_{TCS_i \to MCS}\right)\left\{F_{xyz}(\phi)\right\}_{TCS_i} \end{aligned} \tag{3.30}$$

As the cutting force model for five-axis ball-end milling is the same as three-axis case, and the model will be extended to include five-axis motion using the approach proposed in [26] with modifications for a free-form surface in the subsequent section.

3.2.3 Mechanics of Five-Axis Ball-End Milling

The geometric model of ball-end mill is the same regardless of how many axes are used. On cutting mechanics side, the most important difference between five-axis and three-axis machining is two additional rotational degrees of freedom included in the five–axis case, and the sequence of the cutting force calculation scheme is summarized in Figure 3.4 . The cutter can make simultaneous linear and angular motions in five axis cutting; therefore the tool kinematics differs from that of three-axis. Although these additional motions of the cutter enable the machining of complex parts on a single setup, they bring further challenges to ball-end milling mechanics by leading to varying feedrate along the tool axis. Varying feedrate affects process mechanics as the chip thickness is a function of feedrate (Eq.(3.17)), and the cutting forces are chip thickness dependent (Eq.(3.11)).

In five-axis milling, the cutter can incline according to $X_M - Y_M$ plane and orientation of the cutter is determined by the rotational motions about X_M and Y_M as illustrated in Figure 3.8. The rotation (or inclination in $Y_M - Z_M$ plane) angle around X_M is called as tilt (θ_T), and the rotation (or inclination in $X_M - Z_M$ plane) angle around Y_M is named as the lead angle (θ_L). The positive direction for orientation angles is found by right-hand rule.

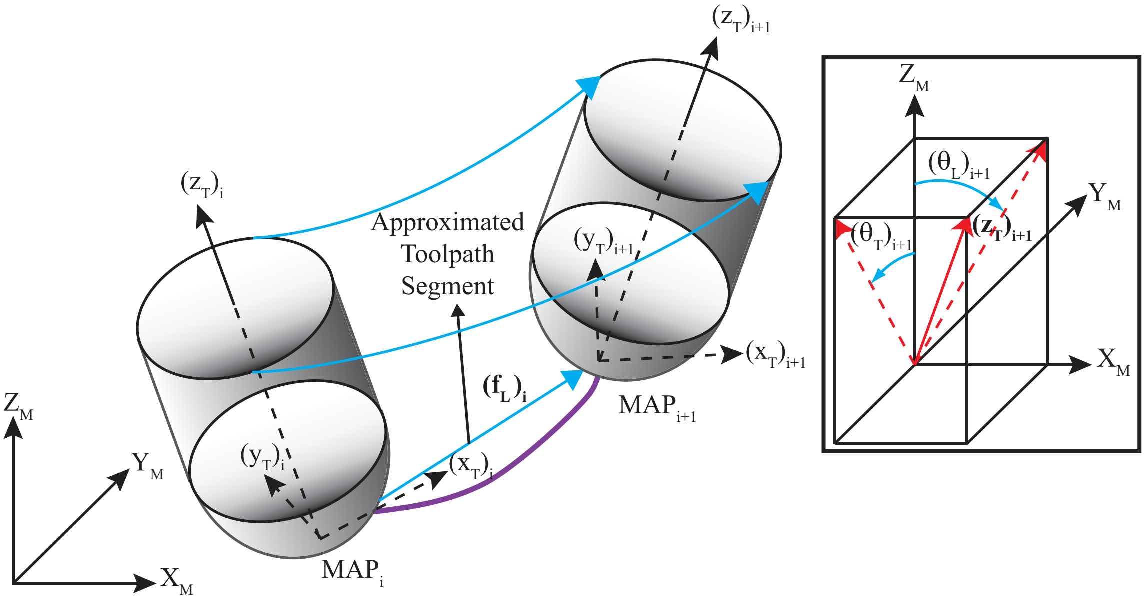

Figure 3.8: Tool orientation, and TCS and MCS in five-axis ball-end milling

A typical five-axis cutter location (CL) file includes the tool tip position and unit tool axis orientation vector in MCS as shown below,

```
GOTO/1.6193,90.8763,0.3937,0.6126733,0.2630138,0.7452886
GOTO/1.6293,90.8497,0.4047,-0.6146300,0.2630986,0.7436458
GOTO/1.6393,90.8231,0.4157,-0.6165827,0.2631817,0.7419981
```

Tool Tip Positon Unit Tool Axis Orientation Vector

The tool tip position and unit tool axis orientation vectors can be obtained from the original CL file; however when the sampling distance at TWEs extraction stage is different than the distance between CL points, both the tool tip position and unit tool axis orientation vector have to be interpolated. This interpolation is already done inside MACHpro; hence these two vectors are known once the sampling distance is defined.

The orientation angles of the cutter at each map point $\mathrm{Map_i}$ can be found as [28],

$$\begin{aligned}(\mathbf{z_T})_i &= a\boldsymbol{i} + b\boldsymbol{j} + c\boldsymbol{k}\\ (\theta_L)_i &= \mathrm{atan2}\left(a, \sqrt{b^2+c^2}\right)\\ (\theta_T)_i &= \mathrm{atan2}(-b, c)\end{aligned} \tag{3.31}$$

where $(\mathbf{z_T})_i$ is the unit tool axis orientation vector in MCS for $\mathrm{Map_i}$.

In five-axis ball-end milling, aligning MCS with $\mathrm{TCS_i}$ is a two-stage process. First, z-axis of MCS and $\mathrm{TCS_i}$ are aligned using θ_T and θ_L, then another rotation has to be carried out for complete mapping. Respecting the sign convention for lead and tilt angles, the first rotation matrix between MCS and TCS at $\mathrm{MAP_i}$ can be defined by superposing the effect of orientation angles,

$$\left(T_{rot_z}\right)_{MCS\to TCS_i} = \begin{bmatrix} 1 & 0 & 0 \\ 0 & \cos\left((\theta_T)_i\right) & \sin\left((\theta_T)_i\right) \\ 0 & -\sin\left((\theta_T)_i\right) & \cos\left((\theta_T)_i\right) \end{bmatrix} \begin{bmatrix} \cos\left((\theta_L)_i\right) & 0 & -\sin\left((\theta_L)_i\right) \\ 0 & 1 & 0 \\ \sin\left((\theta_L)_i\right) & 0 & \cos\left((\theta_L)_i\right) \end{bmatrix} \tag{3.32}$$

Eq. (3.32) only ensures alignment of $(z_T)_i$ and Z_M.

In Figure 3.9(a), the linear feed direction and cutter axis vectors form a plane. As in three-axis ball-end milling, the unit vector in x-direction $(\boldsymbol{x_T})_i$ is positioned in this plane, and the unit vector in y-direction $(\boldsymbol{y_T})_i$ is automatically placed in perpendicular direction as illustrated in Figure 3.9(b). Defining $(\boldsymbol{x_T})_i$ in the same plane with linear feed direction is significant in sense of using the engagement data extracted via MACHpro. The unit vectors representing $\left(\boldsymbol{x_T}\right)_i$ and $\left(\boldsymbol{y_T}\right)_i$ can be obtained using tool tip position vectors in MCS as follows,

$$\begin{aligned} \left(\boldsymbol{y_T}\right)_i &= \left(\boldsymbol{z_T}\right)_i \times \frac{\left(\boldsymbol{P_{i+1}} - \boldsymbol{P_i}\right)}{\left\|\left(\boldsymbol{P_{i+1}} - \boldsymbol{P_i}\right)\right\|} \\ \left(\boldsymbol{x_T}\right)_i &= \left(\boldsymbol{y_T}\right)_i \times \left(\boldsymbol{z_T}\right)_i \end{aligned} \tag{3.33}$$

where, $(\times)$ denotes cross product, $\boldsymbol{P_i}$ and $\boldsymbol{P_{i+1}}$ are the position vectors (defined in MCS) of two consecutive map points along the toolpath.

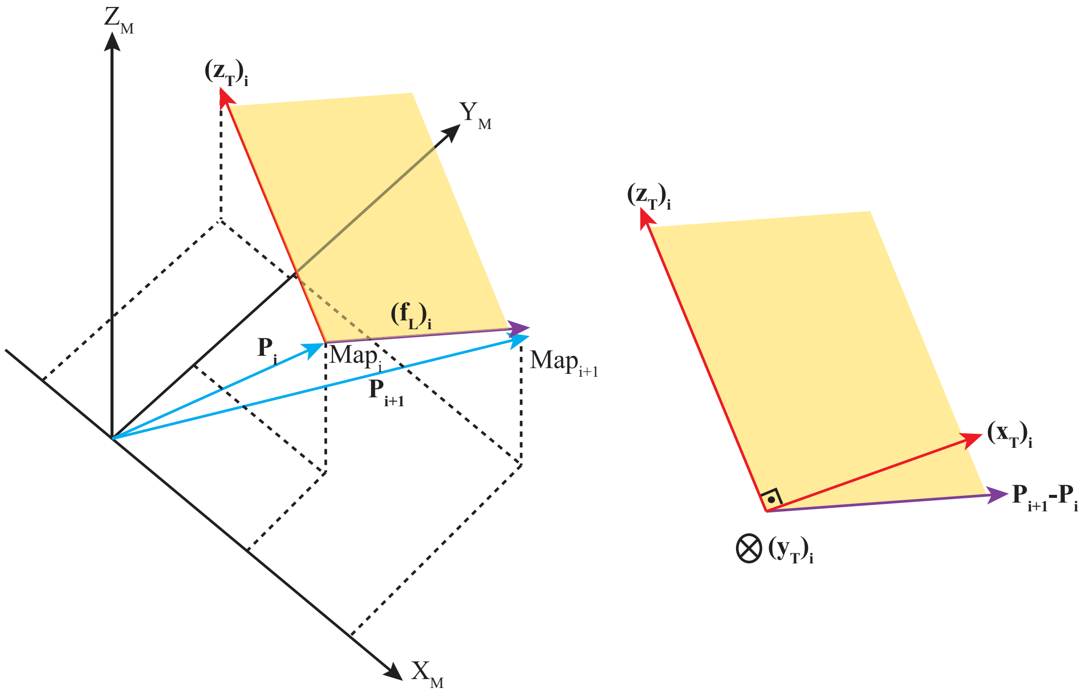

(a) (b)

Figure 3.9: **(a)** Linear feed direction and tool axis vector; **(b)** definition of tool x-axis and linear feed direction

In order to fully map MCS onto TCS_i, the orientation angle between MCS and TCS needs to be calculated. After the first rotation, the orientation of MCS and TCS in horizontal plane is illustrated in Figure 3.10. The rotated cutter axis vectors can be evaluated by,

$$\begin{aligned}\left(\boldsymbol{x}_{\boldsymbol{T}_i}\right)_{\boldsymbol{rotated}} &= \left[\left(T_{rot_z}\right)_{MCS\rightarrow TCS_i}\right]^{-1}\left(\boldsymbol{x}_{\boldsymbol{T}_i}\right) = a_x\boldsymbol{i} + b_x\boldsymbol{j} + c_x\boldsymbol{k} \\ \left(\boldsymbol{y}_{\boldsymbol{T}_i}\right)_{\boldsymbol{rotated}} &= \left[\left(T_{rot_z}\right)_{MCS\rightarrow TCS_i}\right]^{-1}\left(y_{\boldsymbol{T}_i}\right) = a_y\boldsymbol{i} + b_y\boldsymbol{j} + c_y\boldsymbol{k}\end{aligned} \tag{3.34}$$

and the orientation angle in Figure 3.10 can be expressed by,

$$\Omega_i = \tan^{-1}\left(\frac{b_x}{a_x}\right) = \tan^{-1}\left(\frac{a_y}{b_y}\right) \tag{3.35}$$

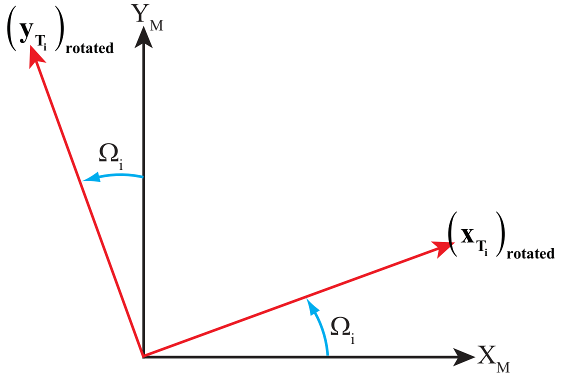

$\left(\mathbf{y}_{\mathrm{T_i}}\right)_{\mathbf{rotated}}$
$\mathrm{Y_M}$
Ω_i
$\left(\mathbf{x}_{\mathrm{T_i}}\right)_{\mathbf{rotated}}$
Ω_i
$\mathrm{X_M}$

Figure 3.10: Orientation of $\left(\boldsymbol{x}_{\boldsymbol{T}}\right)_i$ and $\left(\boldsymbol{y}_{\boldsymbol{T}}\right)_i$ after $\left(\mathbf{z}_{\mathbf{T}}\right)_i$ is aligned with Z_M

Since the rotation matrices defining relative position of MCS with respect to $\mathrm{TCS_i}$ are all defined, now MCS can be transformed into TCS at each $\mathrm{MAP_i}$ by using coordinate transformation,

$$\begin{gathered}\boldsymbol{T} = \left(\boldsymbol{T}_{\boldsymbol{rot_z}}\right)_{\boldsymbol{MCS\rightarrow TCS_i}}\left(\boldsymbol{T}_{\boldsymbol{rot_{xy}}}\right)_{\boldsymbol{i}} \\ \left(T_{rot_{xy}}\right)_i = \begin{bmatrix}\cos(\Omega_i) & \sin(\Omega_i) & 0 \\ -\sin(\Omega_i) & \cos(\Omega_i) & 0 \\ 0 & 0 & 1\end{bmatrix}\end{gathered} \tag{3.36}$$

Since simultaneous linear and angular motions of the tool are superposed, there are two feed components; linear and angular feed. In each toolpath segment, the linear and angular feed can be assumed to be constant [26]. Since the cutter makes a rigid-body motion during linear (translational) movement, any point on the cutter translates the same amount. The linear feed direction vector in Figure 3.9(b) is assumed to stay in $\mathrm{x_T - z_T}$ plane as three-axis case, and can be expressed in $\mathrm{TCS_i}$ as,

$$\left(\mathbf{f_L}\right)_{TCS_i} = \left(\boldsymbol{T}_{rot_z}\right)_{MCS \to TCS_i} \left(\boldsymbol{T}_{rot_{xy}}\right)_i \left(\boldsymbol{T}_{trans}\right)_{MCS \to TCS_i} \tag{3.37}$$

and unit linear feed direction vector is,

$$\left(\mathbf{f_{Lu}}\right)_{TCS_i} = \frac{\left(\mathbf{f_L}\right)_{TCS_i}}{\left\|\left(\mathbf{f_L}\right)_{TCS_i}\right\|} \tag{3.38}$$

The linear feed vector in $\mathrm{TCS_i}$ can be expressed using its unit vector as,

$$\left(\boldsymbol{F_L}\right)_{TCS_i} = F_i \left(\mathbf{f_{Lu}}\right)_{TCS_i} \tag{3.39}$$

where, F_i is linear feed speed (mm/min) at $\mathrm{MAP_i}$.

In order to calculate the angular feed vector resulting from rotational motions of the tool (that shown in Figure 3.11(a)), the angular speed, the total rotation angle, and the distance travelled by the cutter and approximate elapsed time between $\mathrm{MAP_i}$ and $\mathrm{MAP_{i+1}}$ need to be calculated.

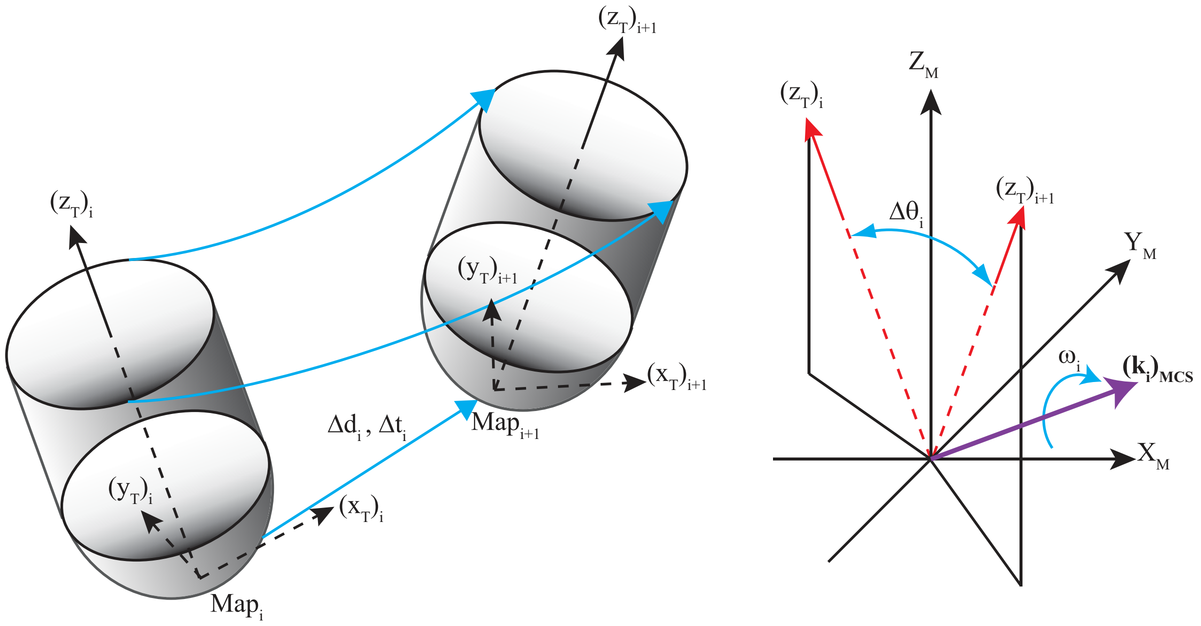
$(z_T)_{i+1}$
$(z_T)_i$
$(y_T)_{i+1}$
$(x_T)_{i+1}$
Map$_{i+1}$
Δd_i, Δt_i
$(y_T)_i$
$(x_T)_i$
Map$_i$
Z_M
$(z_T)_i$
$\Delta\theta_i$
$(z_T)_{i+1}$
Y_M
ω_i
$(\mathbf{k}_i)_{\mathbf{MCS}}$
X_M

(a) (b)

Figure 3.11: **(a)** Angular motion of the cutter in five-axis ball-end milling; **(b)** resultant rotation angle, rotation axis and angular speed

The distance between MAP$_i$ and MAP$_{i+1}$ can be estimated as follows,

$$\Delta d_i = \left\| \boldsymbol{P}_{i+1} - \boldsymbol{P}_i \right\| \tag{3.40}$$

Estimated elapsed time (s) between MAP$_i$ and MAP$_{i+1}$ is,

$$\Delta t_i = \frac{\Delta d_i}{F_i} \tag{3.41}$$

As a result of tool orientation angles, the cutter has a resultant rotation angle $\Delta\theta_i$ as shown in Figure 3.11(a). This resultant angle can be found using the change in unit tool axis orientation vector as,

$$\Delta\theta_i = \text{atan2}\left\{ \frac{\left\| (z_T)_i \times (z_T)_{i+1} \right\|}{(z_T)_i \bullet (z_T)_{i+1}} \right\} \tag{3.42}$$

Since the translational and rotational motions take place simultaneously, angular speed for i^{th} map point can be approximated as,

$$\omega_i \cong \frac{\Delta\theta_i}{\Delta t_i} \tag{3.43}$$

Due to angular motion of the cutter, the axis of rotation has to be known to evaluate the angular feed along the tool axis. It is assumed that the additional rotations are made around an axis passing through the tool tip (Figure 3.11(b)) [26]. This assumption holds when the tool axis orientation does not change drastically between two consecutive, discrete engagement points. The error introduced by the assumption is minimized by selecting the sampling distance as small as possible. Unit rotation axis vector in MCS can be written as,

$$\left(\boldsymbol{k}_{WCS}\right)_i = \frac{\left(\boldsymbol{z_T}\right)_{\boldsymbol{i}} \times \left(\boldsymbol{z_T}\right)_{\boldsymbol{i+1}}}{\left\|\left(\boldsymbol{z_T}\right)_{\boldsymbol{i}} \times \left(\boldsymbol{z_T}\right)_{\boldsymbol{i+1}}\right\|} \tag{3.44}$$

which can be transformed to $\mathrm{TCS_i}$ as,

$$\left(\boldsymbol{k}_{TCS}\right)_i = \left(\boldsymbol{T}_{\boldsymbol{rot}_z}\right)_{\boldsymbol{MCS \to TCS_i}} \left(\boldsymbol{T}_{\boldsymbol{rot}_{xy}}\right)_i \left(\boldsymbol{k}_{WCS}\right)_i \tag{3.45}$$

The angular feed vector in $\mathrm{TCS_i}$ can be found by,

$$\left(\boldsymbol{F_A}(\mathrm{z})\right)_{\boldsymbol{TCS_i}} = \left(\omega_i \left(\boldsymbol{k}_{TCS}\right)_i\right) \times \left(z\ \left(\boldsymbol{z_T}\right)_{\boldsymbol{i}}\right) \tag{3.46}$$

where $\left(\boldsymbol{z_T}\right)_{\boldsymbol{i}} = \begin{bmatrix} 0 \\ 0 \\ 1 \end{bmatrix}$.

The total feed vector at elevation z can be written as,

$$\left(\boldsymbol{F_T}(z)\right)_{\boldsymbol{TCS_i}} = \left(\boldsymbol{F_A}(z)\right)_{\boldsymbol{TCS_i}} + \left(\boldsymbol{F_L}\right)_{\boldsymbol{TCS_i}} \tag{3.47}$$

For regular pitch cutters, the total feed/tooth vector of the cutter in $\mathrm{TCS_i}$ can be evaluated by,

$$\left(\boldsymbol{f}_{\boldsymbol{tot}}(z)\right)_{\boldsymbol{TCS_i}} = \frac{\phi_p}{2\pi n}\left(\boldsymbol{F_T}(z)\right)_{\boldsymbol{TCS_i}} \tag{3.48}$$

where, ϕ_p is pitch angle (rad) of the cutter and n is spindle speed (rpm).

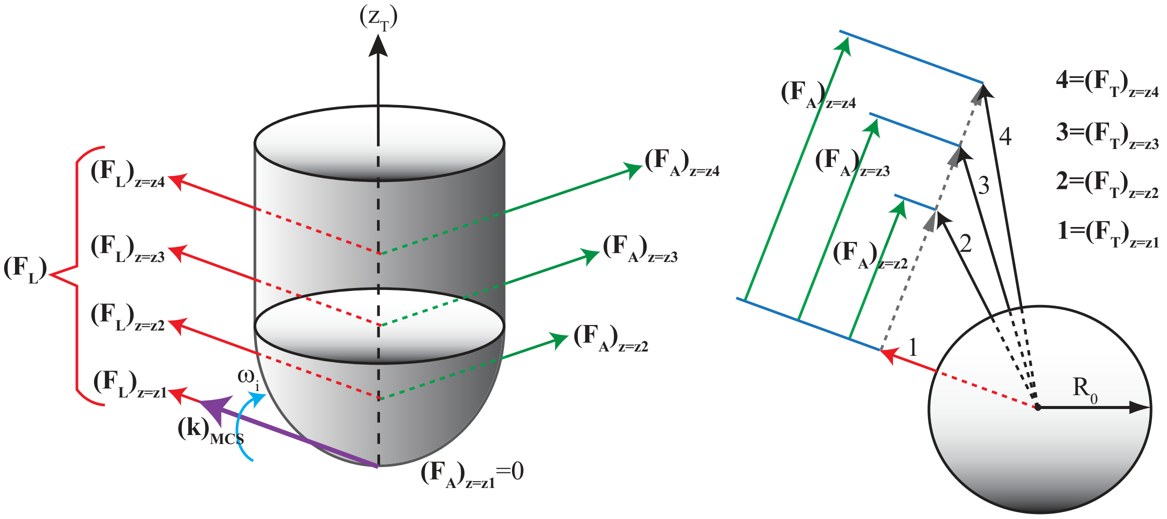

(z_T)
$(F_L)_{z=z4}$
$(F_L)_{z=z3}$
$(F_L)_{z=z2}$
$(F_L)_{z=z1}$
(F_L)
ω_i
$(k)_{MCS}$
$(F_A)_{z=z4}$
$(F_A)_{z=z3}$
$(F_A)_{z=z2}$
$(F_A)_{z=z1}=0$
$(F_A)_{z=z4}$
$(F_A)_{z=z3}$
$(F_A)_{z=z2}$
4
3
2
1
$4=(F_T)_{z=z4}$
$3=(F_T)_{z=z3}$
$2=(F_T)_{z=z2}$
$1=(F_T)_{z=z1}$
R_0

(a) (b)

Figure 3.12: (a) Linear and angular feed components; **(b)** total feed vector at different z-levels, regenerated from [26]

As shown in Figure 3.12(a), the translational feed is constant along the cutter axis; but the magnitude of the angular feed is different at each z-level. Thus, the total feed/tooth vector at each elevation z has different magnitude and direction as illustrated in Figure 3.12(b).

Once the total feed vector is found, the chip thickness generated can be calculated from Eq.(3.18). The cutting forces acting on the cutter (or workpiece) can be evaluated by inserting the chip thickness and force coefficients into Eq.(3.11). These forces can be transformed into MCS by,

$$\left\{F_{xyz}(\phi)\right\}_{MCS} = \boldsymbol{T}^{-1}\left\{F_{xyz}(\phi)\right\}_{TCS_i} \tag{3.49}$$

Having introduced the geometrical and mechanics models for three and five-axis ball-end milling, the justification of indentation problem and its effect on cutting mechanics are presented in Section 3.3.

3.3 Indentation Problem in General Ball-End Milling

The mechanics of three-axis ball-end milling introduced in Section 3.2.2 was verified by Lee and Altintas [12] only at single axis, horizontal plane cutting experiments; hence the researchers did not experience the indentation problem. More experiments were conducted to understand the effects of process parameters on the cutting forces when the surface is inclined as shown in Figure 3.13. The cutting forces were measured in x, y and z directions using 3-component Kistler 9257B table type dynamometer. In Figure 3.13, α is the surface inclination angle, and sub-index D stands for dynamometer.

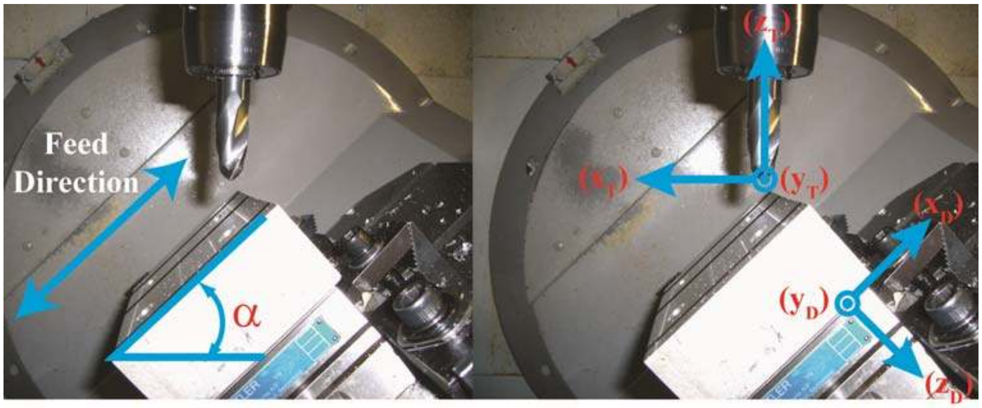

Figure 3.13: Inclined surface ball-end milling experimental setup

Cutting tests at different conditions have been carried out both in upward and downward directions. In up-ramping experiments, the predicted forces in x, y and z directions agreed well with the measured forces as shown in Figure 3.14. Since the tool tip region does not get in contact with the work material in upward direction cutting, the good agreement between experimental and predicted forces is expected.

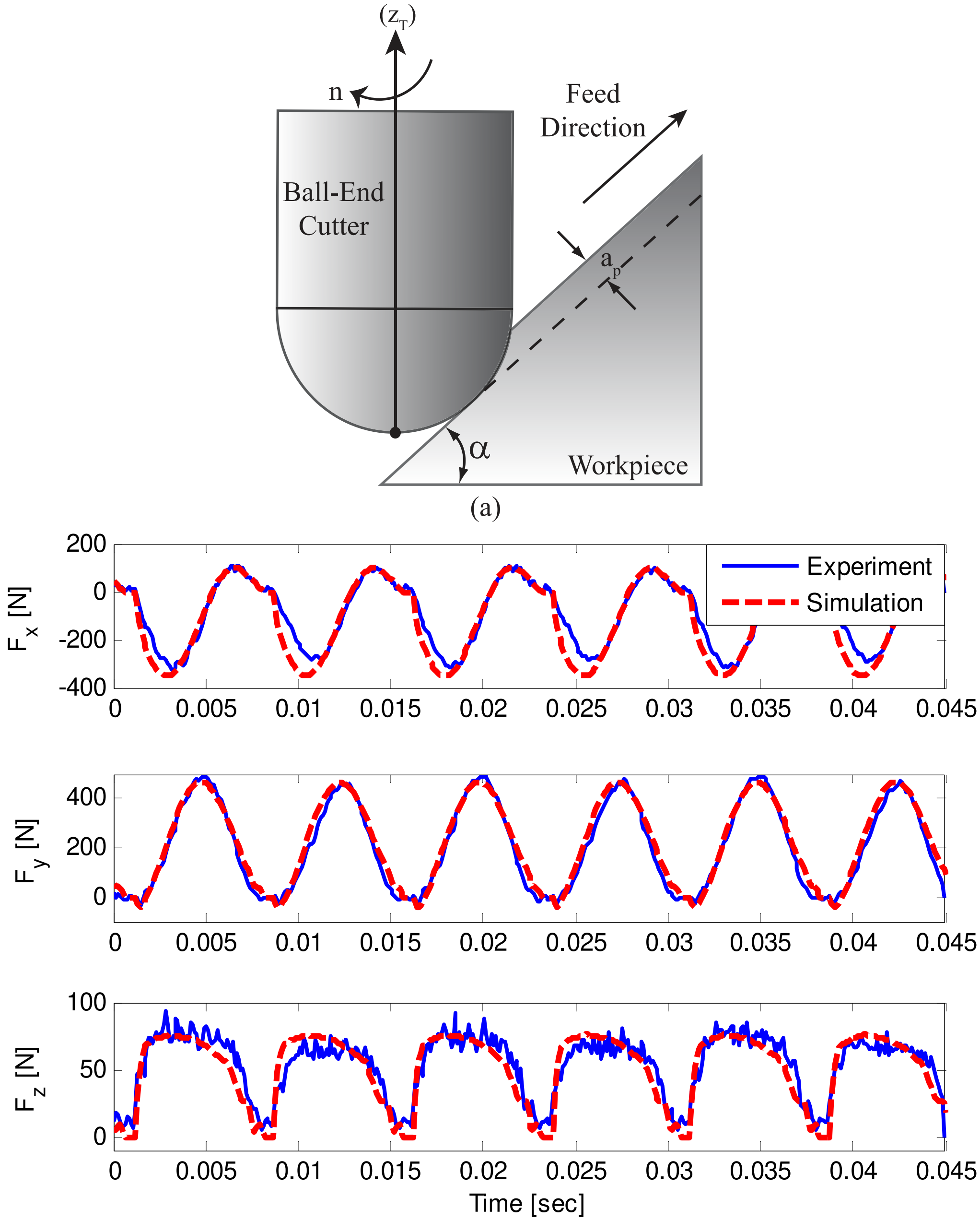
(a)

(b)

Figure 3.14: (a) Schematic illustration of upward ramping case **(b)** comparison of experimental and predicted forces in upward direction inclined surface ball-end milling for following cutting conditions; $R_0 = 8\,\text{mm}, \alpha = 15^0$

$f = 0.1\,\text{mm / rev / tooth}, a_p = 4\,\text{mm},\ N = 2,\ n = 4000\,\text{rpm}, \text{AL7050 workpiece}$

There are two possible engagement regions on the cutter in down-ramping case as illustrated in Figure 3.15. When the surface inclination angle (α) is large enough, or axial depth of cut $\left(a_p\right)$ is small enough, only back side of the cutter cuts the work material (back engagement); otherwise both front and back sides cut together. Experiments were conducted to verify the cutting force model for either cases, and a sample result is given in Figure 3.16.

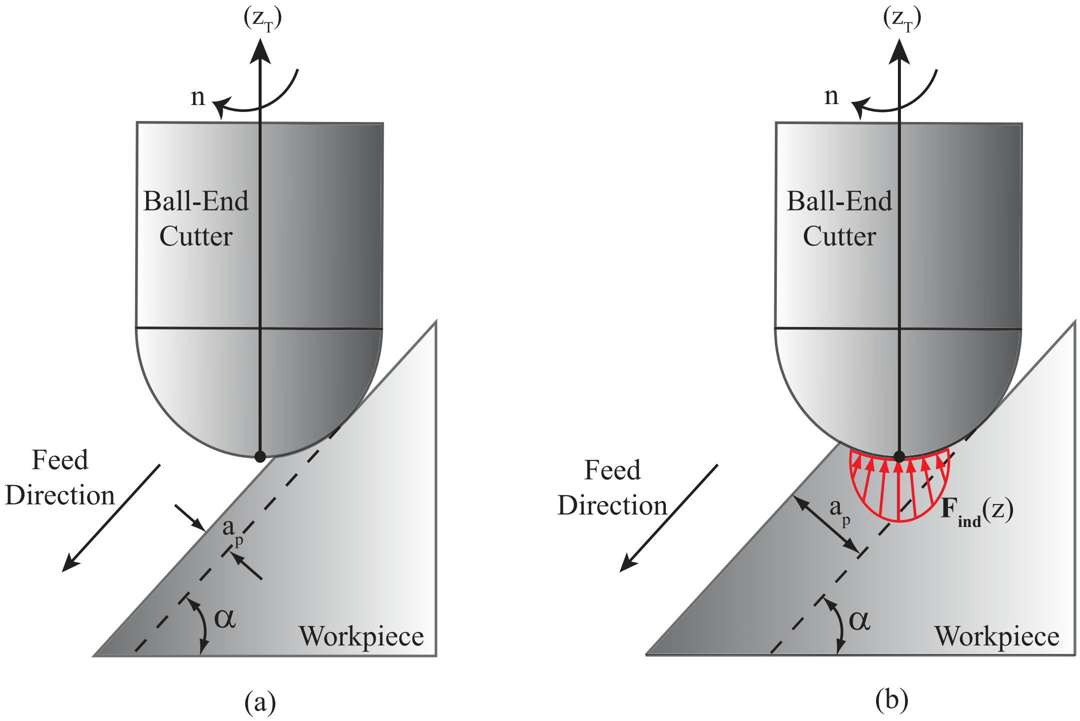

(z_T)
n
Ball-End Cutter
Feed Direction
a_p
α
Workpiece
(a)
(z_T)
n
Ball-End Cutter
Feed Direction
a_p
$\mathbf{F}_{\mathbf{ind}}(z)$
α
Workpiece
(b)

Figure 3.15: Two different cases for down-ramping with ball-end cutter, **(a)** case 1: tool tip is out of cut (back engagement); **(b)** case 2: tool tip is in cut

For the first case (Figure 3.15(a)), the predicted and measured forces match quite well in all three directions as in up-ramping experiments (Figure 3.16(a)); however in the second case (Figure 3.15(b)), although the predictions in x and y directions closely match with experimental forces, the cutting force in z-direction, that is much higher than forces in x and y-directions, was underestimated by $\left|F_z\right| \sim 50\%$ (Figure 3.16(b)). Clearly, existing force model is inadequate for the situation where both sides (both front and back sides) of the cutter engage with the workpiece.

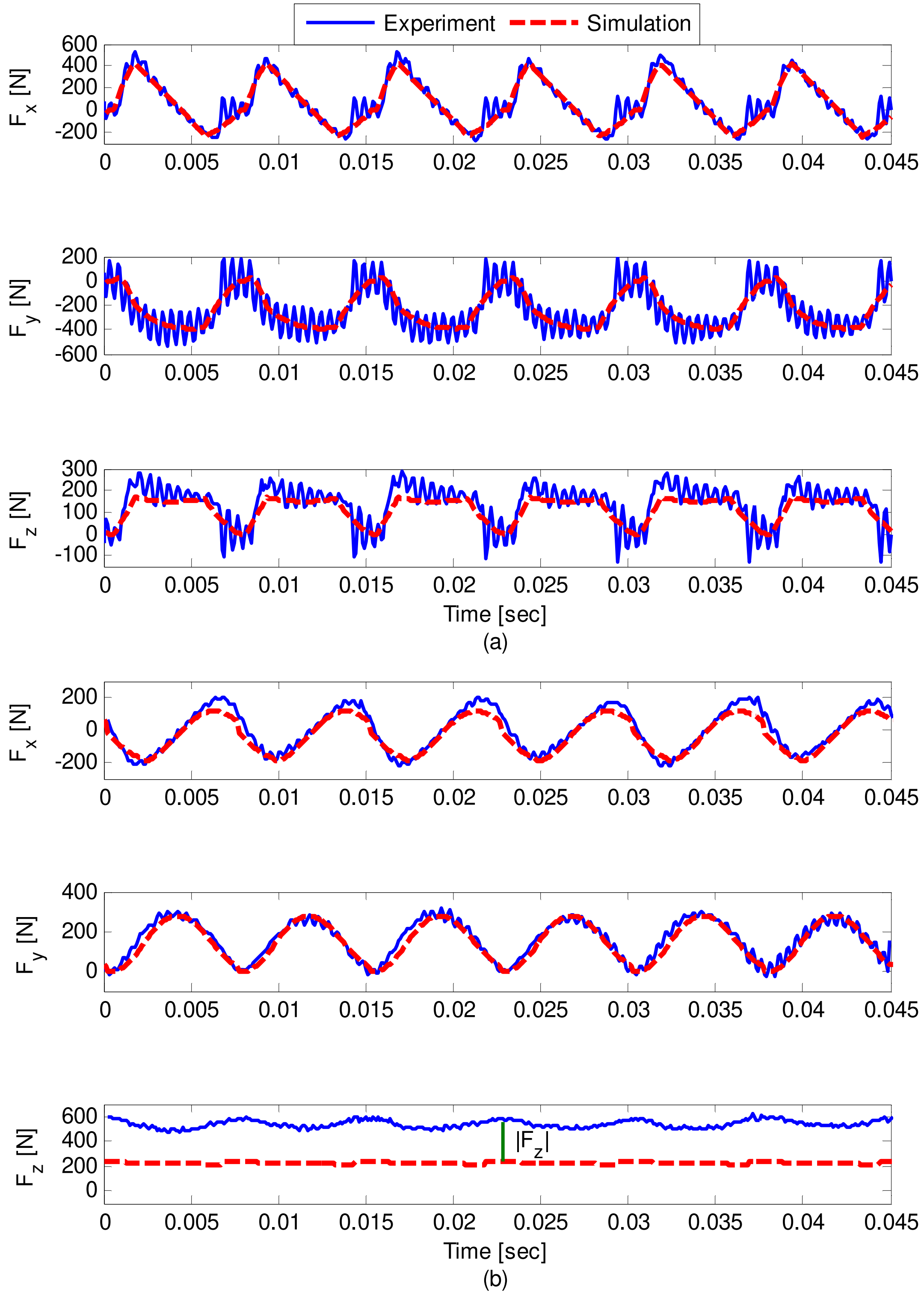

Figure 3.16: Comparison of experimental and predicted forces for 2 cases of downward direction inclined surface ball-end milling for $R_0 = 8\,\text{mm}$, $f = 0.1\,\text{mm/rev/tooth}$, $N = 2$ $n = 4000\,\text{rpm}$, AL7050 workpiece a) $\alpha = 45^0$, $a_p = 2\,\text{mm}$ b) $\alpha = 30^0$, $a_p = 5\,\text{mm}$

Additional cutting tests were conducted to understand which of the process parameters affect the force prediction error in the z-direction. The prediction errors are summarized in **Error! Not a valid bookmark self-reference.**, which indicates that the change in surface inclination angle affects the force prediction error in z-direction.

Table 3.1: The summary of additional cutting tests with related peak to peak error in F_z for different inclination angles

Cutting Tool	**Work Material**	**Feed/tooth (mm/rev/tooth)**	**Axial Depth of Cut (mm)**	**Cutting Type**	**Spindle Speed (rpm)**	**Error $\lvert F_z \rvert$ for $\alpha = 15^0$**	**Error $\lvert F_z \rvert$ for $\alpha = 30^0$**
$\phi 16\,\mathrm{mm}$ $2-$fluted Ball-End	AL7050	0.1	3	Slot Cutting	4000	53.3%	59.8%
					7000	53.3%	58.5%
					10000	54.1%	59.4%
					13500	53.6%	57.3%

The surface inclination affects the vertical feed component of the inclined motion of the cutter as shown in Figure 3.17. Since the vertical feed component exists, the ball-end mill moves into the workpiece during downward direction milling.

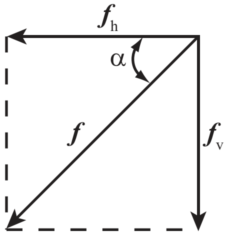

Figure 3.17: Feed components of the tool in inclined surface milling

In back engagement case (Figure 3.15(a)), the tool tip is out of cut; however in the more common case the ball-end tip is in contact with the workpiece as illustrated in Figure 3.15(b). When structural vibrations and cutter run-out are ignored, the tool tip theoretically lies on the rotation axis of the cutter; hence the surface speed (cutting speed) at the tip is zero. In order to remove material, there must be a relative motion between the tool and the workpiece. Since the surface speed (cutting speed) at the tool tip is zero, and the work material is fixed, cutting does not take place. On the other hand, the cutting tool is forced to provide plastic deformation even at the tip point; therefore the desired deformation is realized by indentation (penetration) of the tool instead of cutting. However, the indentation effect is not included in the existing cutting force models; hence the tool indentation brings extra forces in the radial direction as shown in Figure 3.15. The mechanics of tool indentation is studied in Chapter 4.

The indentation problem is classified for two cases regarding the cutting edge geometry: ball-end cutter with positive and negative rake angles. In order to have a general model, indentation force prediction models are proposed for these two cases, and the models are presented in Section 3.4 and Section 3.5.

3.4 Summary

In this chapter, the geometrical and mechanics models for three and five-axis ball-end milling are presented with implementation of both models into three and five-axis toolpaths. It is shown how the process kinematics (additional rotational motions of the cutter) affects the process mechanics via varying feed rate (both in magnitude and direction) along the cutter axis in five-axis ball end milling case. The chip thickness evaluation in five-axis ball-end milling given in [26] is replaced with a vectorial chip load calculation that is general for any type of end mill. Also, the indentation problem resulting from local downward motion of the ball-end cutter at inclined segments is presented with experimental data.

The following chapter is dedicated to the developed general ball-end tool indentation model that characterizes additional forces experienced in three and five-axis ball-end millling, and how it is combined with cutting force models.

4 Modeling the Mechanics of Indentation in Ball-End Milling

The mechanics of the tool indentation into the work material around the tool tip zone where the cutting speed is negligibly small are studied in this chapter. The goal is to develop the mechanics of ball-end milling when the tool indents into the work-material along three and five-axis toolpaths. The plastic deformation zone around the ball-end mill tip is divided into pure indentation, mixed indentation and shearing, and pure shearing zones. The indentation mechanics differ in tools having positive and negative rake angles. A comprehensive model of indentation is presented with experimental validations in the following sections. The chapter is finalized by showing the effect of workpiece temperature on the indentation model, and integration of the proposed model into three and five-axis force models.

4.1 Introduction

Although some researchers tried to solve the indentation problem [1], [6], they did not investigate the physical reason behind the process which can be interpreted through Figure 4.1. For pure horizontal feed, the contribution of points close to the tool tip to chip thickness generation is almost negligible; however for pure vertical feed case, the contribution from those points is significant.

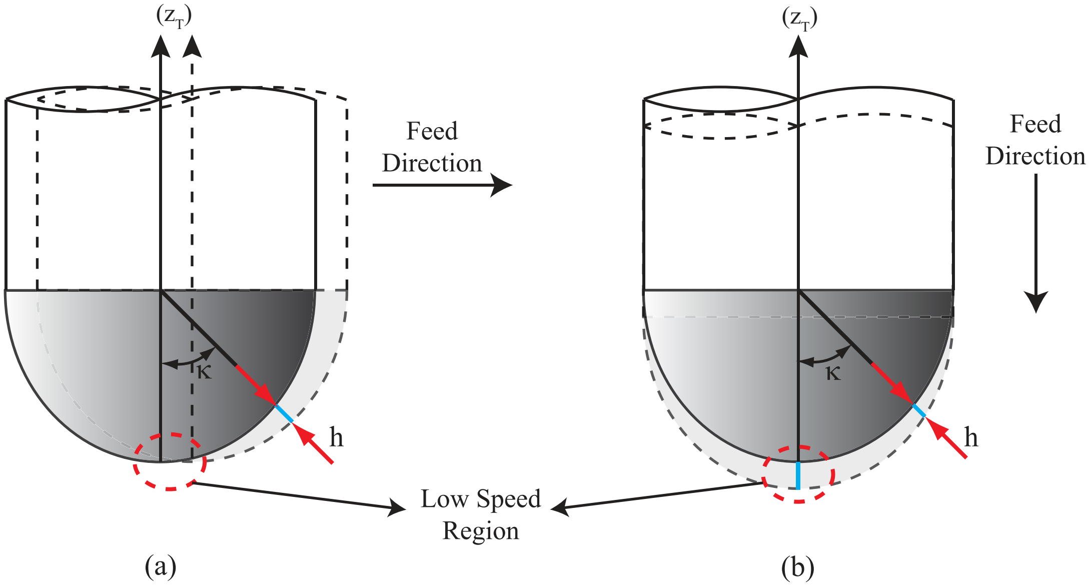

Figure 4.1: Chip thickness distribution in x-z plane, (a) for horizontal feed; (b) for vertical feed

Another fact is the increase in intended chip thickness towards the tool tip in vertical feeding case. Lower the cutting speed towards the tip, higher the expected chip thickness will be. Since the chip generation capability of a point on the flute is directly related to the speed at that point, the points close to the tip cannot generate such a large material removal by shearing. In the meantime, machine tool is commanded to provide that plastic deformation. Therefore, the tool partially shears and indents the work material to accomplish the commanded motion. This leads to some material to be spread by indentation (penetration) of the cutting flute rather than cutting. As a result of this forced mechanism, the indentation effect is quite important in a region that includes the tool tip. Hence, the regions are classified into different material deformation zones as shown in Figure 4.2.

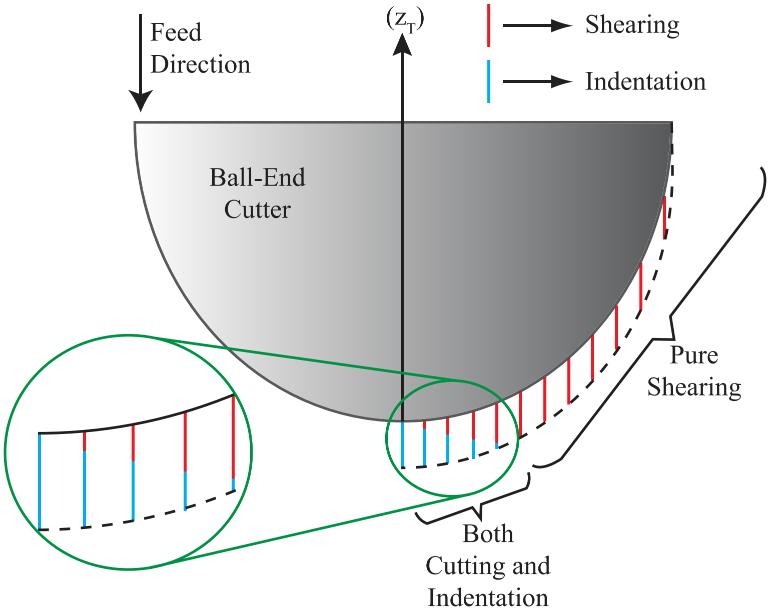
Feed
Direction
(z_T)
Shearing
Indentation
Ball-End
Cutter
Pure
Shearing
Both
Cutting and
Indentation

Figure 4.2: Shearing and indentation regions on the cutter due to vertical feed

Additionally, in such contact problems the variation of depth of indentation is difficult to determine theoretically [30]. In Figure 4.3, the maximum indentation occurs at the tool tip that is equal to the vertical feed/tooth value (f_v), and indentation disappears at $z = f_v$ level. In between these two points, the indentation gradually diminishes along the cutting flute.

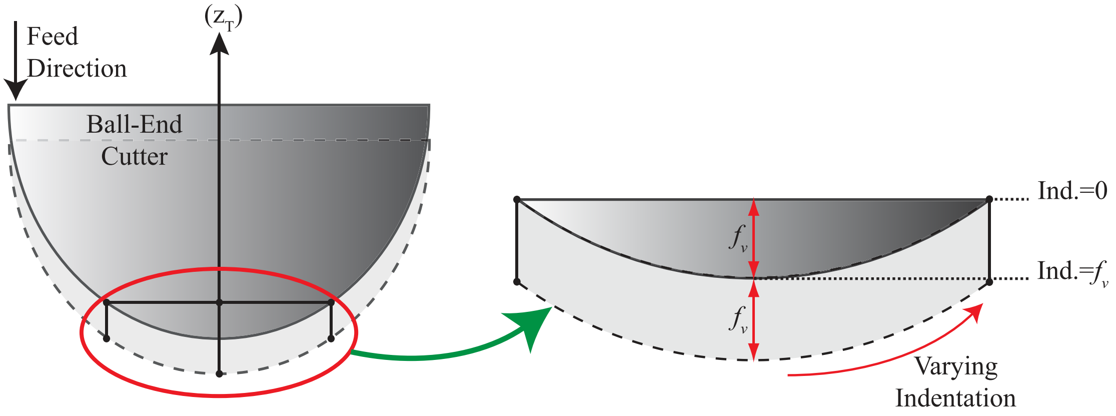
Feed
Direction
(z_T)
Ball-End
Cutter
Ind.=0
f_v
Ind.=f_v
f_v
Varying
Indentation

Figure 4.3: Max and min indentation values and locations along the cutting flute

In the proposed model, the variation of depth of indentation along the cutting flute is modeled by a parabolic distribution similar to the variation of surface speed in the region of interest as given in Figure 4.4. Since the cutting speed is used as a direct measure of indentation, the indentation variation is assumed to show the same variation behaviour.

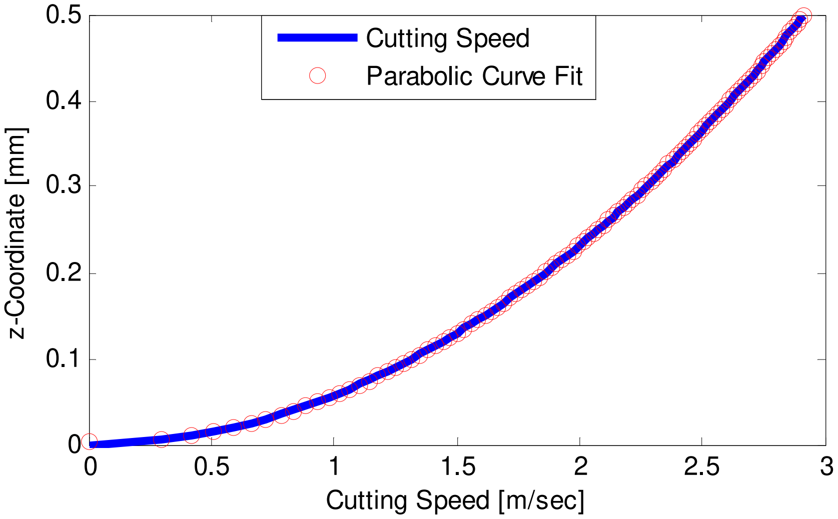

Figure 4.4: Variation of cutting speed at points close to and at the tool tip

The parabolic variation is illustrated for a one-fluted cutter for one spindle period in Figure 4.5. Curve #1 represents the portion of cutting flute in indentation zone whereas Curve #2 is the parabolic indentation depth variation, and Curve #3 represents the position of the cutting flute in indentation zone after one full spindle revolution. The axial coordinates for curve #1 and curve #2 are given as,

$$\left.\begin{aligned} z_{flute}(x) &= R_0 - \sqrt{R_0^2 - x^2} \\ z_{parabola}(x) &= \left(\frac{2f_v}{R_0^2 - \left(f_v - R_0\right)^2} \right) x^2 - f_v \end{aligned}\right\} \tag{4.1}$$

and the indentation depth can be defined by,

$$h_{ind}(z) = z_{flute}(x) - z_{parabola}(x) \tag{4.2}$$

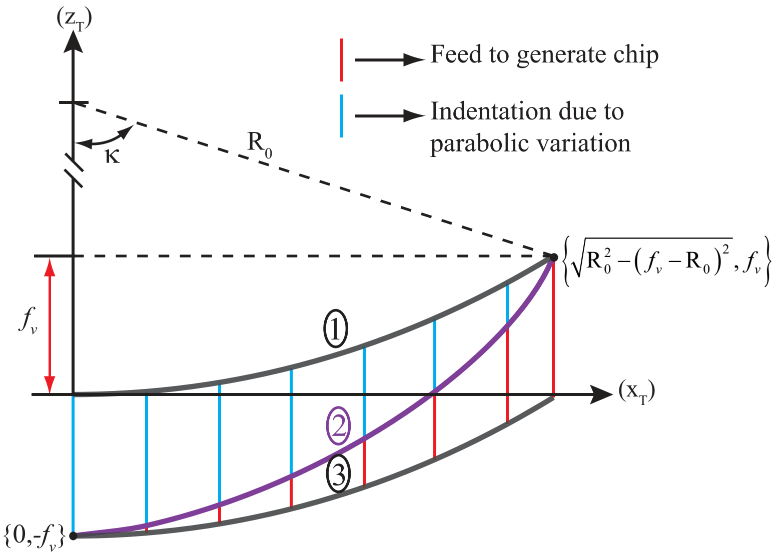
(z_T)
Feed to generate chip
Indentation due to parabolic variation
R_0
κ
f_v
$\left\{\sqrt{R_0^2-(f_v-R_0)^2}, f_v\right\}$
①
②
③
(x_T)
$\{0,-f_v\}$

Figure 4.5: Variation of the indentation along the cutting flute

From now on, the cutting flute will be examined in a smaller scale at each cutting edge element. According to ISO [43], there are two planes to define cutting edge element; horizontal and normal planes as shown Figure 4.6. The radial rake and clearance angles are used for horizontal plane representation of cutting edge element; whereas normal rake and clearance angles are used for normal plane representation. Relations between the angles in horizontal and normal planes are as follows [43],

$$\left.\begin{aligned} \tan\alpha_n &= \frac{\tan\alpha_o}{\cos\lambda_s} \\ \tan\gamma_n &= \tan\gamma_o \, \cos\lambda_s \end{aligned}\right\} \tag{4.3}$$

where, α and γ are clearance and rake angles, λ_s is tool cutting edge inclination angle and it can be assumed to be equal to local helix angle of the cutter [44].

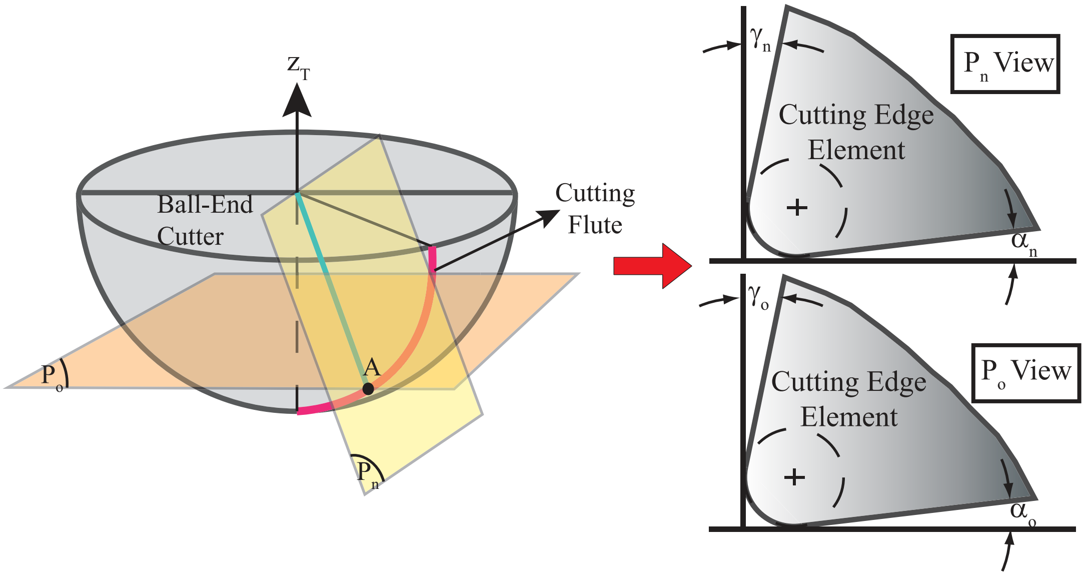
Z_T
Ball-End Cutter
Cutting Flute
A
P_o
P_n
γ_n
P_n View
Cutting Edge Element
+
α_n
γ_o
P_o View
Cutting Edge Element
+
α_o

Figure 4.6: Horizontal (P_o) and normal (P_n) planes definitions and cutting edge element at point A

4.2 Modeling Cutter Indentation for Ball-End Mills with Positive Rake Angle

4.2.1 Elastic Contact Pressure Model for Positive Rake Angle Ball-End Cutter

In this section, elastic behavior of the indentation is modeled as the penetration of cutting edge starts as an elastic contact. The indentation of cutting edge into the work material is assumed to resemble an inclined punch with rounded corners indenting into material as illustrated in Figure 4.7.

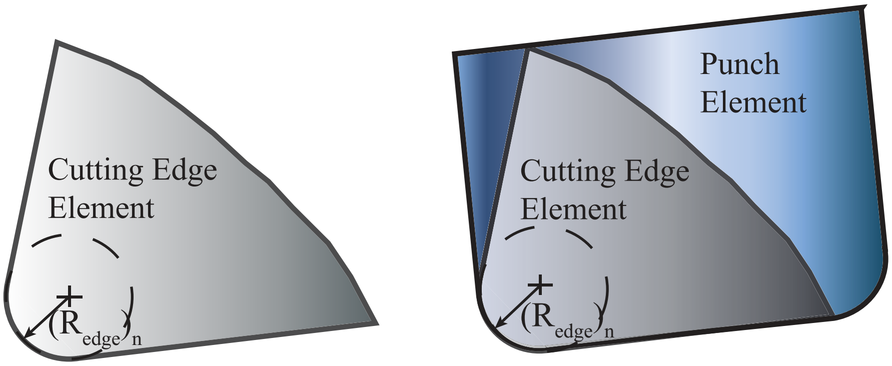
Cutting Edge Element
+
$(R_{edge})_n$
Punch Element
Cutting Edge Element
+
$(R_{edge})_n$

(a) (b)

Figure 4.7: (a) Cutting edge element for ball-end tool with positive rake angle (b) geometric similarity between inclined punch with rounded edges and cutting edge element

Figure 4.8 shows the newly introduced cutting edge coordinate system and an exaggerated view of how small cutting edge elements form the entire flute neglecting the helix angle.

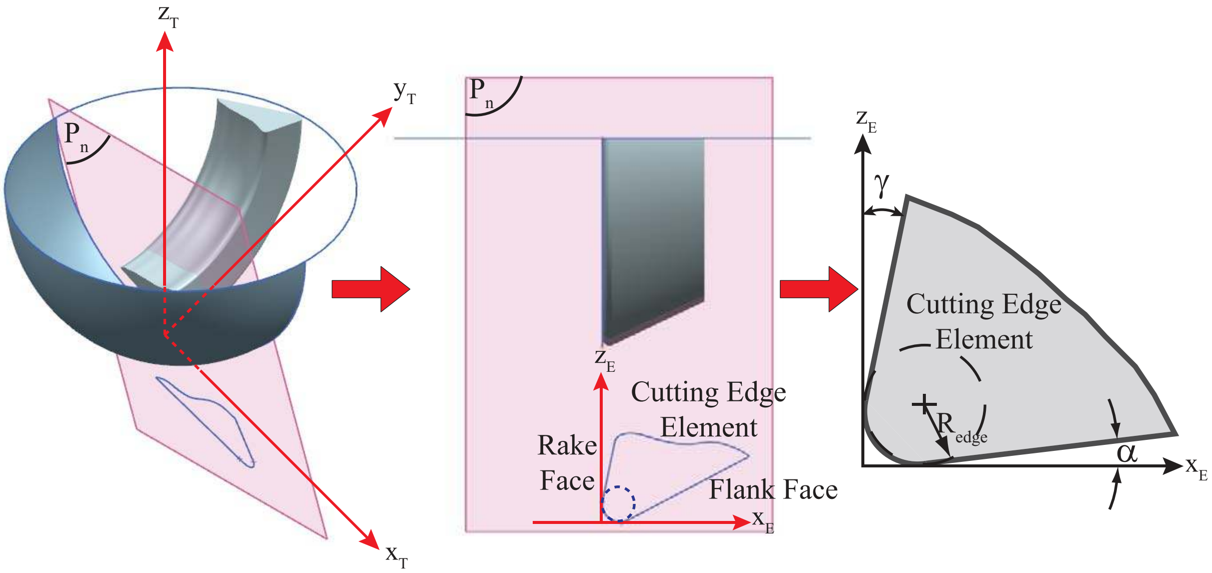
z_T
y_T
x_T
P_n
P_n
z_E
Cutting Edge Element
Rake Face
Flank Face
x_E
z_E
γ
Cutting Edge Element
R_{edge}
α
x_E

Figure 4.8: Punch indentation analogy and cutting edge coordinate system

The elastic contact model for tilted punch is applied to the indentation of cutting edge for the case illustrated in Figure 4.9 under the following assumptions;

i. The indentation of the cutting flute is modeled as a plane strain deformation with line loading,

ii. Cutting edge is assumed to penetrate the workpiece with a steady velocity,

iii. There is no friction in contact region,

iv. The cutting tool is assumed to be rigid and the work material is assumed to undergo elasto-plastic deformation,

v. The flank face of the cutting edge is straight and long enough to accommodate entire indentation, As shown in Figure 4.9, the positive rake face of the tool does not contact the work material, which is opposite to the tools with negative rake angle.

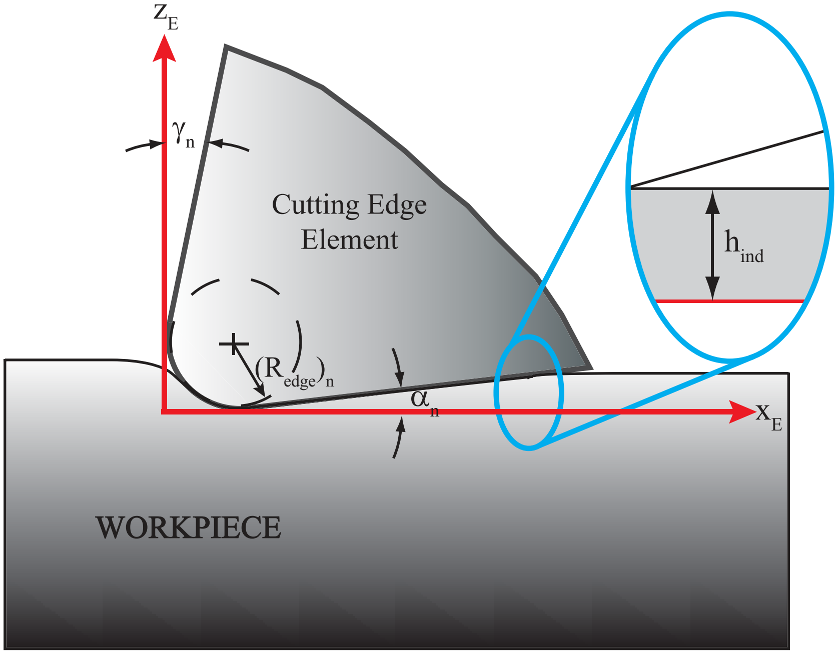

Figure 4.9: Indentation of cutting edge element into workpiece for positive rake angle

The analytical formulation of contact problem of the punch with rounded corners has been studied in the last decade by several researchers [31], [32], [33], [34]. The elastic contact formulation presented by Goryacheva et al. [33] is adapted to the cutting edge indentation in this thesis.

Since the cutting edge indentation takes place on the positive side of x_E, the punch indentation in [33] can be modified as shown in Figure 4.10. The shape of the punch can be described by,

$$f(x) = \begin{cases} -x\tan\alpha & , \quad -a < x < c \\ \dfrac{(x-c)^2}{2R_{edge}} - x\tan\alpha & , \quad c \le x \le b \end{cases} \tag{4.4}$$

The normal surface displacement in contact zone is,

$$\mathrm{v}(\mathrm{x}) = \Delta \mathrm{y} - \mathrm{f}(\mathrm{x}) \tag{4.5}$$

where, Δy is the rigid body displacement.

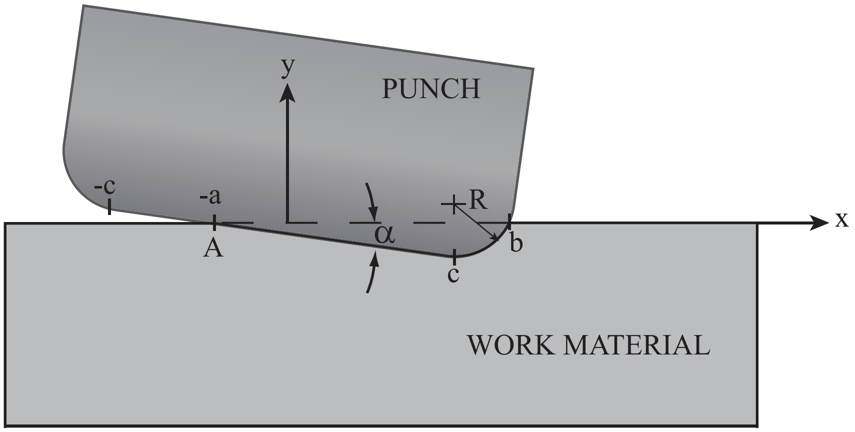

Figure 4.10: Indentation of inclined punch with rounded corners into material, adapted from [33]

For frictionless line loading conditions, the normal surface displacement gradient can be found as [30],

$$\frac{\partial \mathrm{v}}{\partial \mathrm{x}} = \mathrm{v}'(\mathrm{x}) = -\frac{2\left(1-\nu^2\right)}{\pi E}\int_{x_1}^{x_2}\frac{p(t)}{x-t}dt \tag{4.6}$$

In order to get the expression for contact pressure p(t), Eq.(4.6) needs to be inverted using Riemann-Hilbert procedure that is given in [48] as,

$$p(x) = \frac{E}{4\pi\left(1-\mathrm{v}^2\right)}\sqrt{(x+a)(b-x)}\int_{-\mathrm{a}}^{\mathrm{b}}\frac{\mathrm{v}'(t)dt}{\sqrt{(t+a)(b-t)}(t-x)} \quad , \quad x\in[-a,b] \tag{4.7}$$

where, ν is Poisson's ratio, E (MPa) the Young's Modulus of the work material. When the general case given in [33] is customized to the cutting edge indentation, the integral equation for contact pressure can be obtained as,

$$p_{elastic}(x) = \frac{E}{4\pi\left(1-\mathrm{v}^2\right)}\sqrt{(x+a)(b-x)}\left[-\tan\alpha\int_{-a}^{b}\frac{dt}{g(t)(t-x)} + \left(\frac{x-c}{R}\right)\int_{c}^{b}\frac{dt}{g(t)(t-x)} + \frac{1}{R}\int_{c}^{b}\frac{dt}{g(t)}\right] \tag{4.8}$$

The elastic contact pressure (normal surface traction) due to cutting edge element indentation can be obtained by superposing the penetration of rounded and straight parts of the edge as follows [33],

$$p_{elastic}(x)=\frac{E^{*}\left(a+b\right)}{2\pi R\left(1+y^{2}\right)}\left\{\frac{1-y^{2}}{2}\left[\frac{\pi}{2}-2\tan^{-1}\left(y_{1}\right)-\frac{\left(y-y_{1}\right)\left(1-yy_{1}\right)}{\left(1+y_{1}^{2}\right)}\ln\left(\left|\frac{y_{1}-y}{yy_{1}-1}\right|\right)\right]\right\} \tag{4.9}$$

where, $|y|\leq 1$.

$$\left.\begin{aligned}E^{*}&=\frac{E}{2\left(1-\nu^{2}\right)}\\ y&=\tan\left(\frac{1}{2}\sin^{-1}\left(\frac{2x-b+a}{a+b}\right)\right)\\ y_{1}&=\tan\left(\frac{1}{2}\sin^{-1}\left(\frac{2c-b+a}{a+b}\right)\right)\\ y_{2}&=\tan\left(\frac{1}{2}\sin^{-1}\left(\frac{-2c-b+a}{a+b}\right)\right)\end{aligned}\right\} \tag{4.10}$$

where, parameters *a*, *b* and *c* are given in Figure 4.10. *a* (mm) is the indentation width in negative x-direction in rounded part, *b* (mm) is the indentation width in positive x-direction in rounded part and *c* (mm) is the indentation width in positive x-direction in flat part.

In order to make the coordinate system given in Figure 4.10 compatible with the one given in Figure 4.9, the point A (where the contact ends) can be positioned at the origin of the x-y frame in Figure 4.10. This shifts the system origin and allows the parameter *a* to be set to zero.

As the governing equation for the elastic contact pressure is obtained, the required geometrical parameters of the indentation region can be calculated for ball-end mills with positive rake angle with two indentation conditions; indentation depth can be either less or higher than R_{edge} as illustrated in Figure 4.11. In Figure 4.11, the indices 1 and 2 denote $h_{ind}\leq R_{edge}$ and $h_{ind}>R_{edge}$ conditions, respectively.

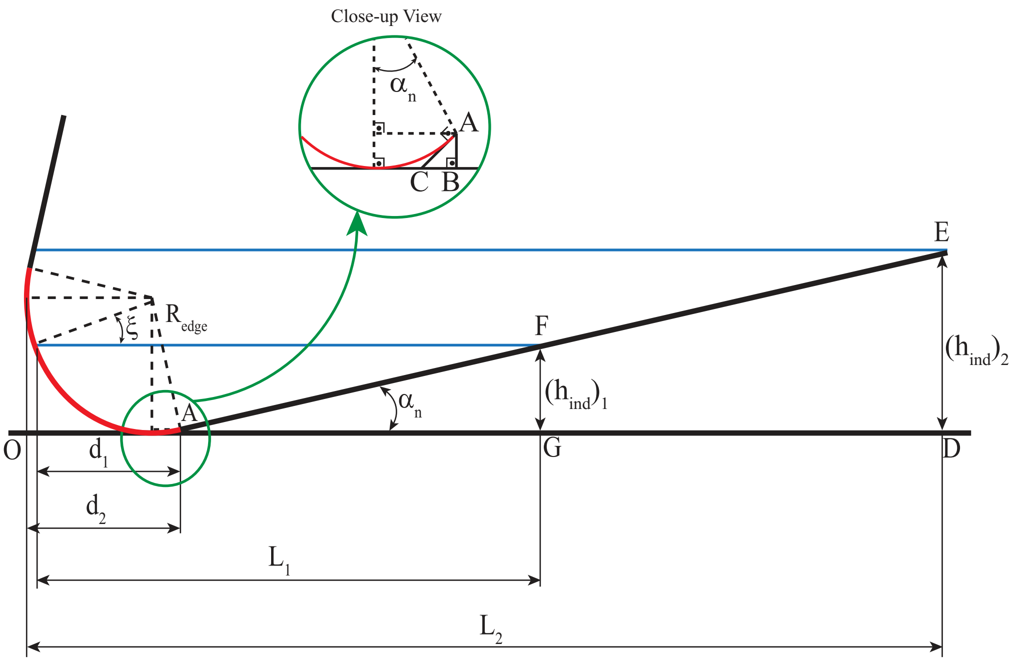

Figure 4.11: Indentation related dimensions for both conditions

The geometry of the indentation region is mainly determined by the cutting edge geometry $\left(\alpha_n \text{ and } R_{edge}\right)$, and the indentation depth. The indentation limit angle at rounded part can be expressed as,

$$\xi = \sin^{-1}\left(1 - \frac{h_{ind}}{R_{edge}}\right) \tag{4.11}$$

the projected length of rounded part on x_E is,

$$d = R_{edge}\left(\sin\alpha_n + \cos\xi\right) \tag{4.12}$$

Using the similarity of triangles CAB and CED the overall contact length on x_E can be obtained as follows,

$$L = d + \frac{h_{ind}}{\tan\alpha_n} - \frac{R_{edge}\left(1-\cos\alpha_n\right)}{\tan\alpha_n} \tag{4.13}$$

the geometrical parameters *b* and *c* in Eq.(4.10) can be expressed as,

$$\begin{aligned} b &= L \\ c &= L - d \end{aligned} \tag{4.14}$$

For the second possible case as further indentation after $h_{ind} = R_{edge}$ does not increase the indentation width at left end of cutting edge element, Eq.(4.11) to Eq.(4.14) can be used by setting $\xi = 0^0$.

For indentation of the cutting edge element, left-hand side of punch element is penetrating into the workpiece; therefore the pressure distribution is mirror version of the distribution given by Eq.(4.9) as shown in Figure 4.12.

The contact pressure distribution for cutting edge element indentation is asymmetrical because of asymmetry in indenting portion of the edge element. Also, the distribution is continuous and becomes zero at both ends. There would be a discontinuity at the tip of cutting edge element if the edge radius was not considered since discontinuity in the slope of the surface causes singularity in pressure distribution in any contact geometry [38]. As there is no atomic scale sharpness on cutters (even for brand new ones), the edge radius is a realistic assumption. The rounded part of the edge element is represented by a parabolic approximation in Eq. (4.4); therefore the pressure distribution must show a Hertzian distribution while the indentation of rounded part is dominant against the straight part of the edge element that requires $\left((b - c)/b\right) \approx 1$. As shown in Figure 4.13, the contact of the cutting edge element is Hertzian for $\left((\mathrm{b} - \mathrm{c})/\mathrm{b}\right) \approx 1$ and becomes punch indentation while $\left((\mathrm{b} - \mathrm{c})/\mathrm{b}\right) << 1$. These results are similar to previous studies of Sackfield [34] and Ciavarella [36].

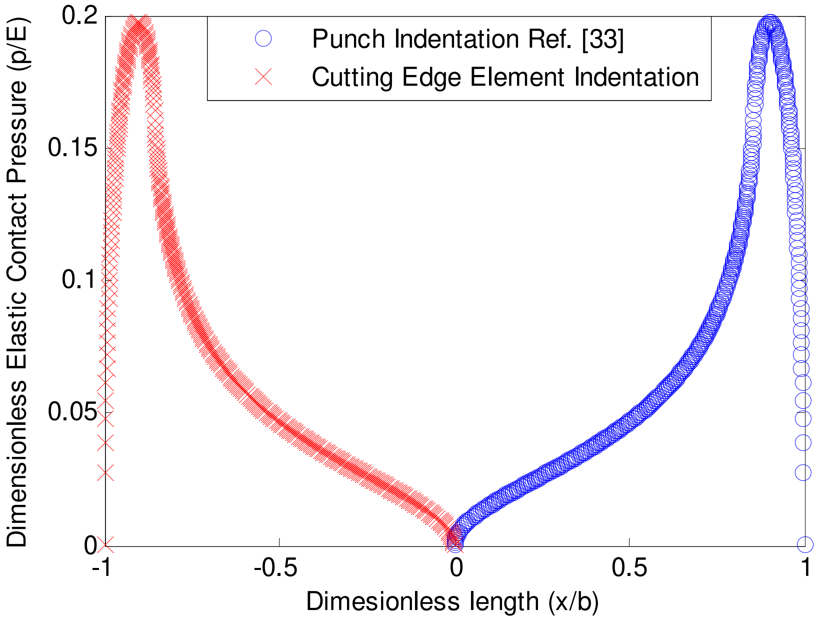

Figure 4.12: Dimensionless elastic contact pressure distribution for punch [33] and cutting edge indentations for; $h_{ind} = 5\,\mu m, R_{edge} = 10\,\mu m, d = 9.5\,\mu m, L = 66.2\,\mu m$, nominal $\alpha_n = 5^0$ and AL7050 work material

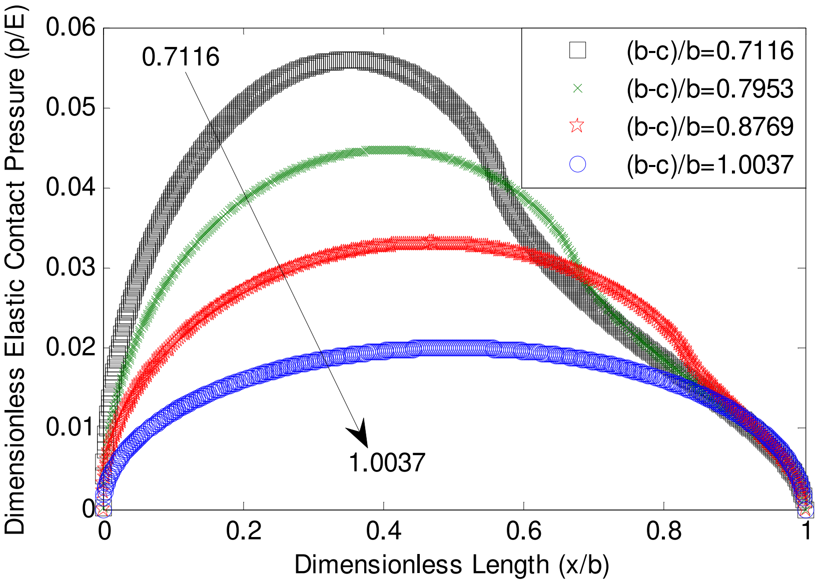

Figure 4.13: Dimensionless pressure distribution due to cutting edge indentation for different $((b-c)/b)$ values for; $R_{edge} = 10\,\mu m, \alpha_n = 5^0, \gamma_n = 12^0$ $\phi 16\,mm$ ball – end cutter and AL7050 workpiece

The presented model gives accurate elastic contact pressure results while $h_{ind} \leq R_{edge}$; however in order to calculate the contact pressure distribution for $h_{ind} > R_{edge}$, the model needs to be modified. This modification requires to define a dummy indenter (cutting edge element) for each h_{ind} that is higher than R_{edge}. That indenter sustains incomplete contact and allows Eq. (4.9) to be used to evaluate elastic contact pressure even for $h_{ind} > R_{edge}$. The following condition holds for each dummy cutting edge element,

$$\left(\mathrm{R}_{\mathrm{edge}}\right)_{\mathrm{dummy}} = \mathrm{h}_{\mathrm{ind}} > \left(\mathrm{R}_{\mathrm{edge}}\right)_{\mathrm{actual}} \tag{4.15}$$

Once the actual edge radius of the cutting edge element is replaced with $\left(\mathrm{R}_{\mathrm{edge}}\right)_{\mathrm{dummy}} = \mathrm{h}_{\mathrm{ind}}$, the total contact pressure (plastic contact pressure -that will be explained in Section 4.2.2- and elastic contact pressure) for dummy edge can be evaluated using dummy indentation dimensions. As explained in Section 4.2.2, total pressure distribution shows elastic contact only on right hand side of the indentation geometry when $h_{ind} > R_{edge}$, in other words plastic contact occurs on left side around the rounded part. Therefore, the elastic pressure solution for left side of the indentation geometry has no effect on total pressure distribution.

The assumptions for this calculation scheme are given as follows;

i. For $h_{ind} = \left(R_{edge}\right)_{actual}$ the left end of cutting edge element (rounded part) causes plastic deformation (plastic contact pressure) and elastic deformation (elastic contact pressure) takes place at right-hand side towards the end of indentation geometry,

ii. As $h_{ind} = \left(R_{edge}\right)_{actual}$ causes plastic contact pressure at rounded end, for $h_{ind} > \left(R_{edge}\right)_{actual}$ plastic contact pressure at rounded end is inevitable,

iii. The elastic contact region of dummy cutting edge element is similar to that of actual one.

The difference between the actual and dummy indenters is illustrated in Figure 4.14. The cutting edge element #1 is the dummy indenter, #2 is the actual edge element for $\left(h_{ind}\right)_1 = \left(R_{edge}\right)_A$ and #3 represents the actual edge element for $\left(h_{ind}\right)_2 > \left(R_{edge}\right)_A$. As seen, the indentation of straight parts of dummy and actual cutting edge elements are almost the same for $\left(h_{ind}\right)_2 > \left(R_{edge}\right)_A$, and shows the same indentation character that supports the last assumption made above. Justification of the first two assumptions will be given after the plastic contact pressure model is introduced in Section 4.2.2.

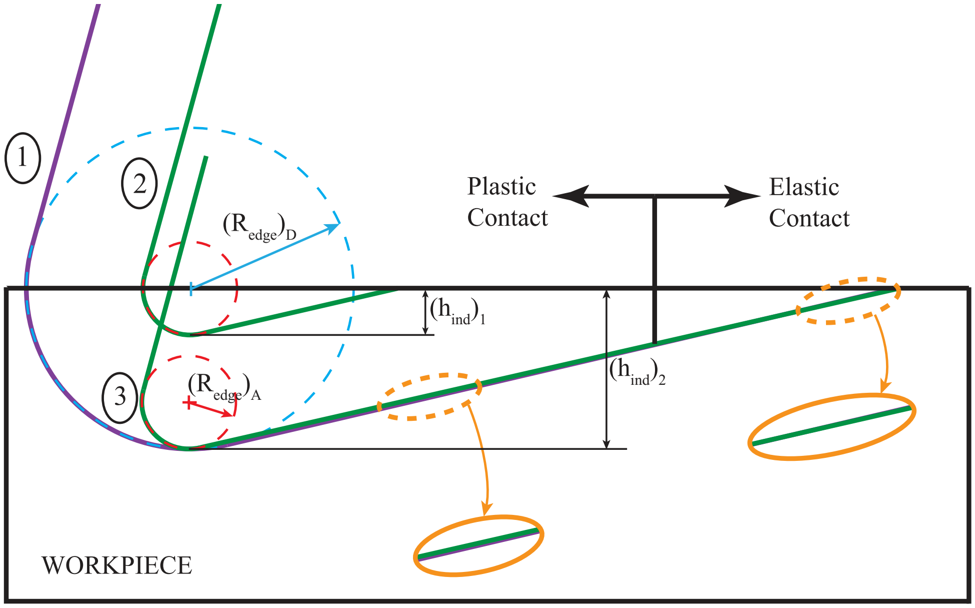

Figure 4.14: Indentation of actual and dummy cutting edges

4.2.2 Plastic Contact Pressure Model for Positive Rake Angle Ball-End Cutter

Indentation of cutting edge causes both elastic and plastic deformations [49]. Hence, the contact pressure due to plastic deformation must be included in indentation model as well. The deformable work material is assumed to show elastic-perfectly plastic material behavior.

When the yield point is first exceeded the plastic flow starts; however, even under elastic-perfectly plastic conditions, the material that starts yielding is fully contained by surrounding elastic material. As Johnson [30] pointed out, plastic and elastic strains are of the same magnitude at that stage. When the indentation advances, plastic strains become dominant over elastic ones and the material becomes free to flow plastically, so uncontained plastic deformation occurs. According to the afore mentioned deformation regime, the plastic contact pressure can be expressed as [30],

$$\begin{aligned} p_{plastic} &= C\,\sigma_Y \\ 1 \le C &\le 3 \end{aligned} \tag{4.16}$$

where, σ_Y (MPa) is the yield strength of the work material in compression (tension), and the coefficient C depends on material type, friction conditions and indenter geometry. The lower and upper limits for C characterize the onset of plastic flow and fully uncontained plastic flow respectively. Consequently, the plastic contact pressure in indentation zone is higher than yield strength of the material being indented.

For ball-end milling, the accurate value of the coefficient C can be obtained from indentation tests that are both time consuming and dangerous since either the cutter or spindle system of the machine tool might be damaged during the tests. Therefore, finite element (FE) simulations are employed instead. FE simulations can be run for different work materials, and different normal rake and clearance angles (cutting geometry) to obtain the coefficient C. The details of calibration of coefficient C from FE results are given in Chapter 5.

Similar to the projected area of Kachanov indentation [50], the total contact pressure over projected contact area can be obtained by superposing the elastic and plastic contact pressures [49] as shown in Figure 4.15.

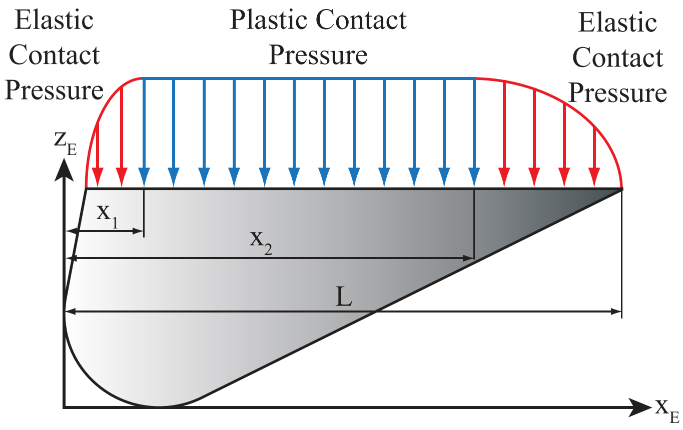

Figure 4.15: General total contact pressure distribution for positive rake angle ball-end cutter

The condition required for continuous pressure distribution at $x = x_{1,2}$ is,

$$p_{elastic}\left(x = x_{1,2}\right) = p_{plastic}\left(x = x_{1,2}\right) \tag{4.17}$$

Finally, the total contact force per unit contact length can be found as,

$$K_{ind}(x) = \int_{x_0}^{x_1} p_{elastic}(x)dx + \int_{x_1}^{x_2} p_{plastic}(x)dx + \int_{x_2}^{L} p_{elastic}(x)dx \tag{4.18}$$

where, $x_0 = R_{edge}\left(1 - cos\xi\right)$.

Total contact distributions presented in Figure 4.16 are calculated for $h_{ind} = \left(R_{edge}\right)_{actual}$ by assuming $C = C_{\max} = 3$ for now. As seen from Figure 4.16, the rounded part of the cutting edge element causes plastic deformation; and elastic contact occurs towards the right end of the contact. Thus, the result of elastic solution for left side has no effect on the overall solution. Since the indentation depth which is equal to edge radius already results in plastic contact at rounded part, even bigger indentation depths automatically provide plastic contact at the same region. These results justify the first two assumptions made for the case $h_{ind} > R_{edge}$ in Section 4.2.1.

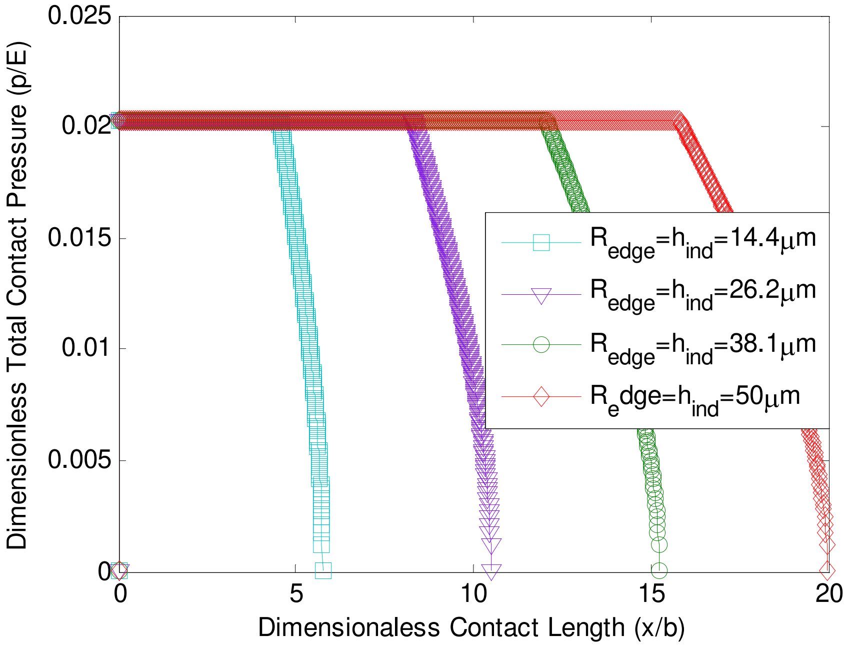

Figure 4.16: Dimensionless total contact pressure distribution for different edge radii (for each radius $h_{ind} = \left(R_{edge}\right)_{actual}$) and conditions; $\mathrm{R_{edge}} = 10\,\mu\mathrm{m}, \alpha_n = 5^0, \gamma_n = 12^0$ $\phi 16\,\mathrm{mm\ ball-end\ cutter}$ and AL7050 workpiece

In this section, the elastic and plastic contact pressure prediction models are presented for positive rake angle ball-end cutter. The solution for the problem for different cutting flute geometry, namely negative rake angle, is detailed in the following section.

4.3 Modeling Cutter Indentation for Ball-End Mills with Negative Rake Angle

Negative rake angle provides high strength to the cutting edges enabling them to resist against high impact loads in machining hard materials. Although ball-end mills usually use positive rake angles, the cutters with negative rake angle are also used for some special operations like hard milling [51]. In the following sub-sections the elastic and plastic contact models for ball-end cutters with negative rake angle are presented.

4.3.1 Elastic Contact Pressure Model for Negative Rake Angle Ball-End Cutter

Using the geometrical similarity between the cutting edge element for negative rake angle ball-end cutter and wedge geometry, the indentation of cutting edge into the work material is assumed to resemble a wedge element with rounded tip (apex) indenting into the material as shown in Figure 4.17. The only difference is asymmetrical side angles of cutting edge element.

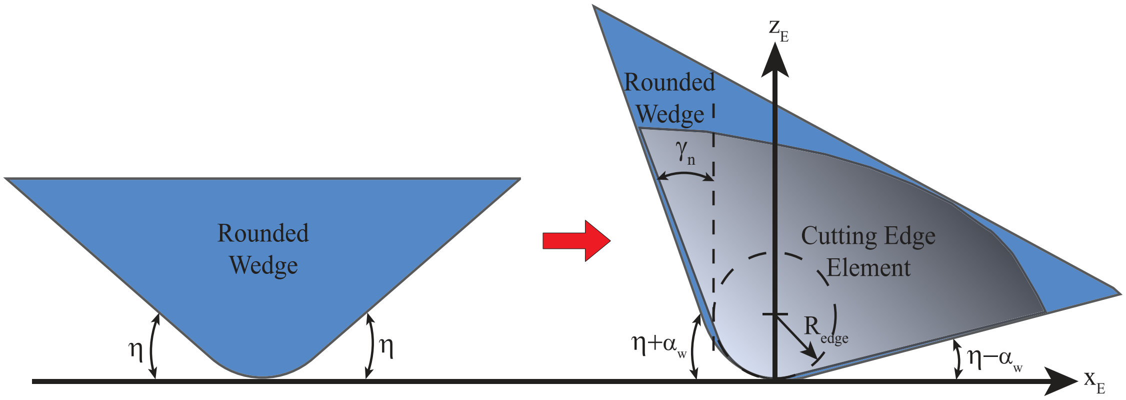
Rounded
Wedge
η
η
Rounded
Wedge
γ_n
z_E
Cutting Edge
Element
R_{edge}
$\eta+\alpha_w$
$\eta-\alpha_w$
x_E

Figure 4.17: Geometrical similarity between a wedge with rounded tip and cutting edge element

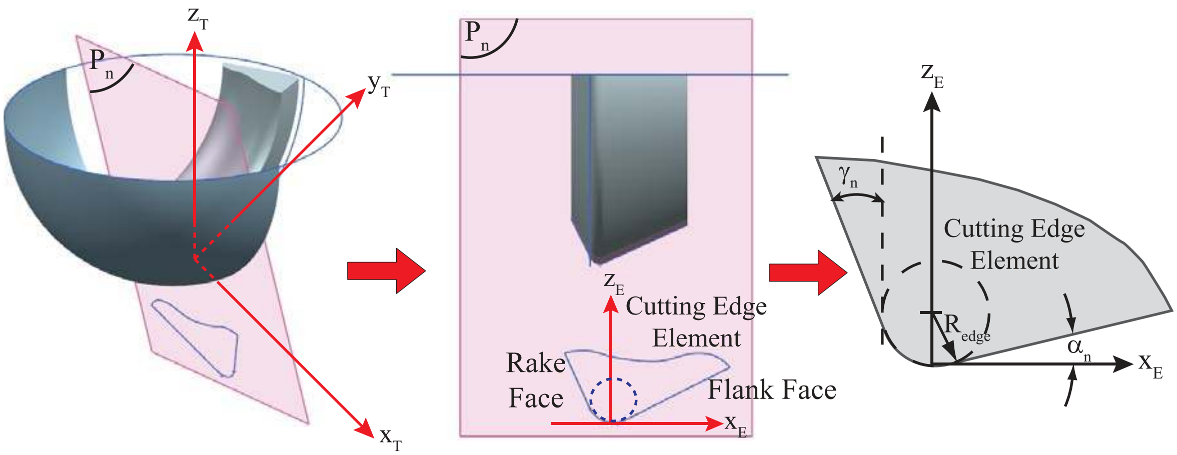
z_T
P_n
y_T
x_T
P_n
z_E
Cutting Edge
Element
Rake
Face
Flank Face
x_E
z_E
γ_n
Cutting Edge
Element
R_{edge}
α_n
x_E

Figure 4.18: Wedge indentation analogy and cutting edge coordinate system

The edge element is modeled as a tilted wedge with rounded tip as illustrated in Figure 4.18. The cutting edge and its side angles are all defined in normal plane as in Section 4.2.1; an exaggerated view of how small cutting edge elements form the entire flute neglecting helix, and cutting edge coordinate system are shown Figure 4.18.

Under the same assumptions made in positive rake angle case, the elastic contact model for tilted wedge is applied to the indentation of cutting edge for the case illustrated in Figure 4.19. Unlike the ball-end mill with a positive rake angle, the rake face of the cutter is in contact with the work material that always provides incomplete contact on the left side of the indentation region.

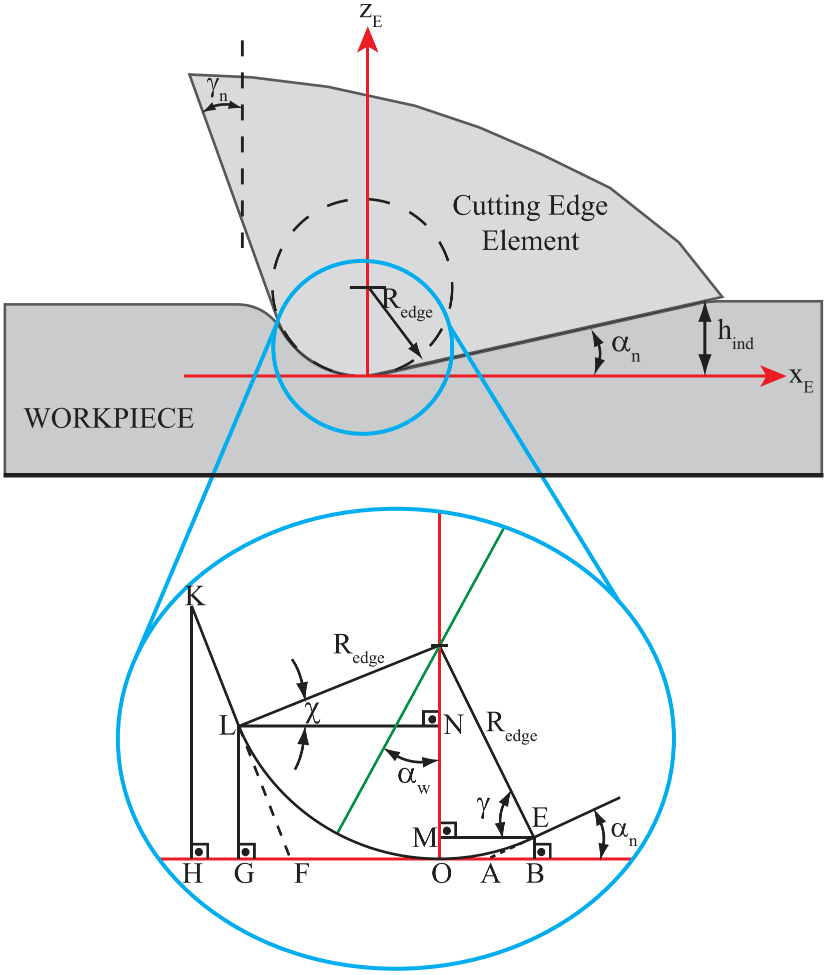

z_E
γ_n
Cutting Edge Element
R_{edge}
α_n
h_{ind}
x_E
WORKPIECE
K
R_{edge}
χ
L
N
R_{edge}
α_w
γ
E
M
α_n
H
G
F
O
A
B

Figure 4.19: Indentation of cutting edge element into workpiece for negative rake angle

Modeling the elastic contact pressure for negative rake case is achieved in two steps. First the contact pressure is modeled for edge element with no edge radius, and then the actual elastic pressure is obtained by patching the radius effect into the sharp edge solution which has a singularity at the apex point due to discontinuity in surface slope.

For a sharp nose edge element, the normal surface displacement can be expressed as [37],

$$\mathrm{v}(\mathrm{x})=\begin{cases}\Delta\mathrm{y}-(\eta-\alpha_{\mathrm{w}})\mathrm{x}\ , & 0\le x<d_2\\ \Delta\mathrm{y}+(\eta+\alpha_{\mathrm{w}})\mathrm{x}\ , & -d_1\le x<0\end{cases} \tag{4.19}$$

where, d_1 and d_2 are indentation width on negative and positive side of x_E respectively, $\Delta\mathrm{y}$ is the rigid body displacement, and angles $(\eta-\alpha_\mathrm{w})$ and $(\eta+\alpha_\mathrm{w})$ are side angles of the edge element. Using Eq. (4.6), Eq. (4.7) and a canonical interval [-1,1] instead of $[-\mathrm{d}_1,\mathrm{d}_2]$, the integral expression for elastic contact pressure can be found as given in [37],

$$p(x(r))=\frac{E\sqrt{1-r^2}}{4\pi(1-\nu^2)}\int_{-1}^{1}\frac{\mathrm{v}'(t(s))}{\sqrt{1-s^2}\,(s-r)}ds \tag{4.20}$$

where, region mapping elements are

$$\begin{aligned}x&=\frac{d_1+d_2}{2}\left(r+\frac{d_2-d_1}{d_1+d_2}\right)\\ t&=\frac{d_1+d_2}{2}\left(s+\frac{d_2-d_1}{d_1+d_2}\right)\end{aligned} \tag{4.21}$$

As the detailed derivations are given in [37], the integral in Eq. (4.20) leads to the elastic contact pressure in original coordinates as,

$$p_{sharp}(x)=\frac{-E\eta}{2\pi(1-\nu^2)}\ln\left(\left|\frac{1-\sqrt{\dfrac{1-x/d_2}{1+x/d_1}}}{1+\sqrt{\dfrac{1-x/d_2}{1+x/d_1}}}\right|\right) \tag{4.22}$$

Eq. (4.22) is singular at x=0; thus corrective term should be inserted into the equation to consider the rounded part of the edge element. Dini et al. [38] developed an asymptotic corrective expression for any kind of contact geometry that has a logarithmic singularity as in Eq. (4.22). The corrective term that accounts for roundness of the edge element is as follows,

$$p_{corrective}(x)=\frac{-E\eta}{2\pi\left(1-\nu^2\right)}\left\{\frac{1}{2}\left(1-\frac{x}{b}\right)\ln\left(\left|\frac{b}{x}-1\right|\right)+\frac{1}{2}\left(1+\frac{x}{b}\right)\ln\left(\left|\frac{b}{x}+1\right|\right)-1\right\} \tag{4.23}$$

where b is the half width of rounded apex for symmetrical wedge. In order to obtain final elastic contact pressure expression, it is convenient to rewrite Eq.(4.22) in the following form,

$$p_{sharp}(x)=\frac{-E\eta}{2\pi\left(1-\nu^2\right)}\left(\ln\left(\left|x\right|\right)+\ln\left(d_1+d_2\right)-\ln\left(\left|x\left(d_2-d_1\right)+2d_1d_2\right|\right)\right) \tag{4.24}$$

The final elastic contact pressure expression can be obtained by inserting Eq.(4.23) into Eq. (4.24) as follows,

$$p_{elastic}(x)=\frac{-E\eta}{2\pi\left(1-\nu^2\right)}\left(\begin{array}{l}\frac{1}{2}\left(1-\frac{x}{b}\right)\ln\left|\left(b-x\right)\left(d_1+d_2\right)\right|+\frac{1}{2}\left(1+\frac{x}{b}\right)\ln\left|\left(b+x\right)\left(d_1+d_2\right)\right|\\ -\ln\left(\left|x\left(d_2-d_1\right)+2d_1d_2\right|\right)-1\end{array}\right) \tag{4.25}$$

As governing equation for the elastic contact pressure is obtained, the required geometrical parameters shown in Figure 4.19 can be calculated. As seen from the close-up view, the indentation width on positive side of the indentation region, d_2, can be found as,

$$d_2=\begin{cases} R_{edge}\cos\gamma & ,\ if\ \ h_{ind}<R_{edge}\left(1-\sin\gamma\right)\\ \left(R_{edge}\cos\gamma\right)+\tan\gamma\left[h_{ind}-R_{edge}\left(1-\sin\gamma\right)\right] & ,\ if\ \ h_{ind}\geq R_{edge}\left(1-\sin\gamma\right)\end{cases} \tag{4.26}$$

The indentation width on negative side of the indentation region, d_1, is,

$$d_1=\begin{cases} R_{edge}\cos\chi & ,\ if\ \ h_{ind}<R_{edge}\\ \tan\chi\left(\frac{\left(\eta-\alpha_w\right)}{\left(\eta+\alpha_w\right)}h_{ind}-R_{edge}\left(1-\sin\chi\right)\right)+R_{edge}\cos\chi & ,\ if\ \ h_{ind}\geq R_{edge}\end{cases} \tag{4.27}$$

Half width of rounded apex for symmetrical cutting edge can be expressed by,

$$b=R_{EDGE}\cos(90^0-\eta) \tag{4.28}$$

Similar to positive rake angle case, the contact of the cutting edge element with the work material starts as Hertzian, and as the indentation advances, the contact becomes wedge indentation. In Figure 4.19, when the distance $|GB|$ is denoted by *r*, Hertzian recovery is obtained for $(r/(d_1+d_2))\approx 1$, and once the conditions for $(r/(d_1+d_2))<<1$ occur the wedge indentation becomes the dominant indentation mode. This trend is exemplified in Figure 4.20.

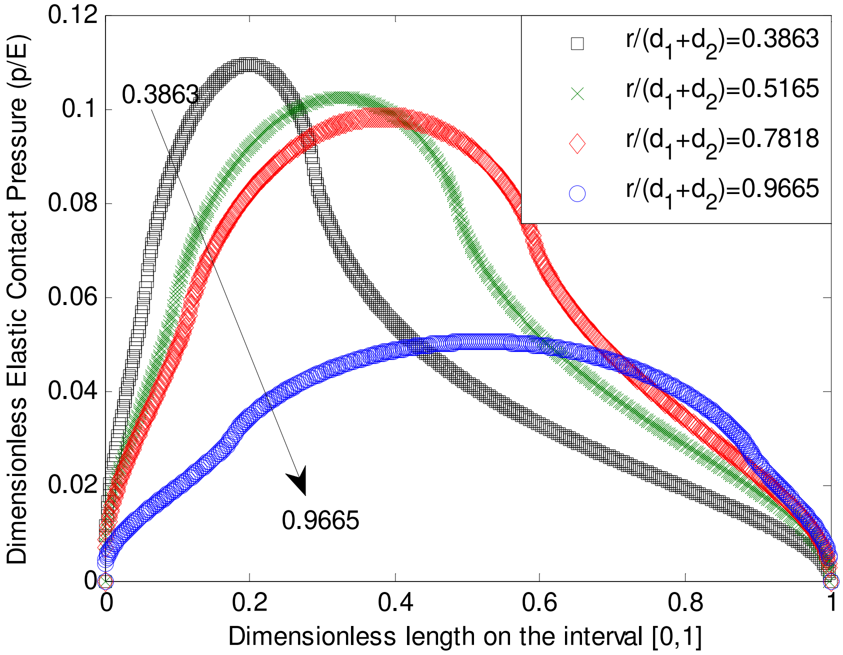

Figure 4.20: Dimensionless elastic pressure distribution due to cutting edge indentation for different $(r/(d_1+d_2))$ values for; $R_{edge}=10\,\mu m, \alpha_n=5^0, \gamma_n=-12^0$ $\phi 16\,mm$ ball – end cutter and AL7050 workpiece

4.3.2 Plastic Contact Pressure Model for Negative Rake Angle Ball-End Cutter

As explained in Section 4.4.2, indentation of negative rake angle results in both elastic and plastic deformations, and the plastic contact pressure shows the behaviour given in Eq. (4.16). Correspondingly, the superposition of these deformations gives a total contact pressure over projected contact area as illustarted in Figure 4.21. Similar to the positive rake angle case, the indentation force per unit contact length can be found using Eq. (4.18) for elastic limits $[-d_1,-x_1]$ and $[x_2,d_2]$, and plastic limit $[-x_1,x_2]$.

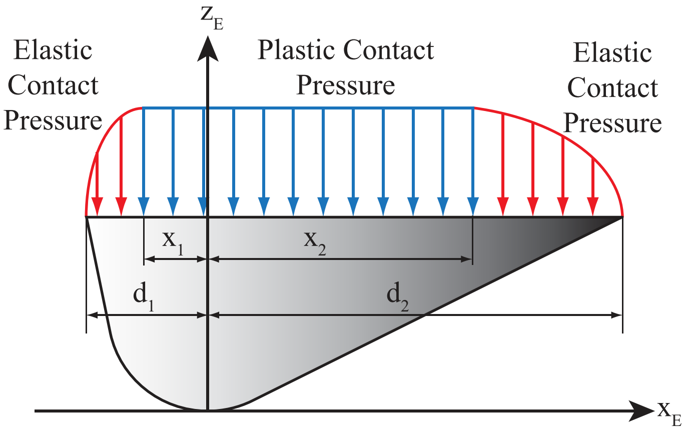
z_E
Elastic Contact Pressure
Plastic Contact Pressure
Elastic Contact Pressure
x_1
x_2
d_1
d_2
x_E

Figure 4.21: General total contact pressure distribution for negative rake angle ball-end cutter

The dimensionless total pressure distribution example given in Figure 4.22 is generated by assuming $C = C_{\max} = 3$ as in positive rake angle case to demonstrate how the plastic deformation sets the upper limit of elastic contact pressure for different indentation depths.

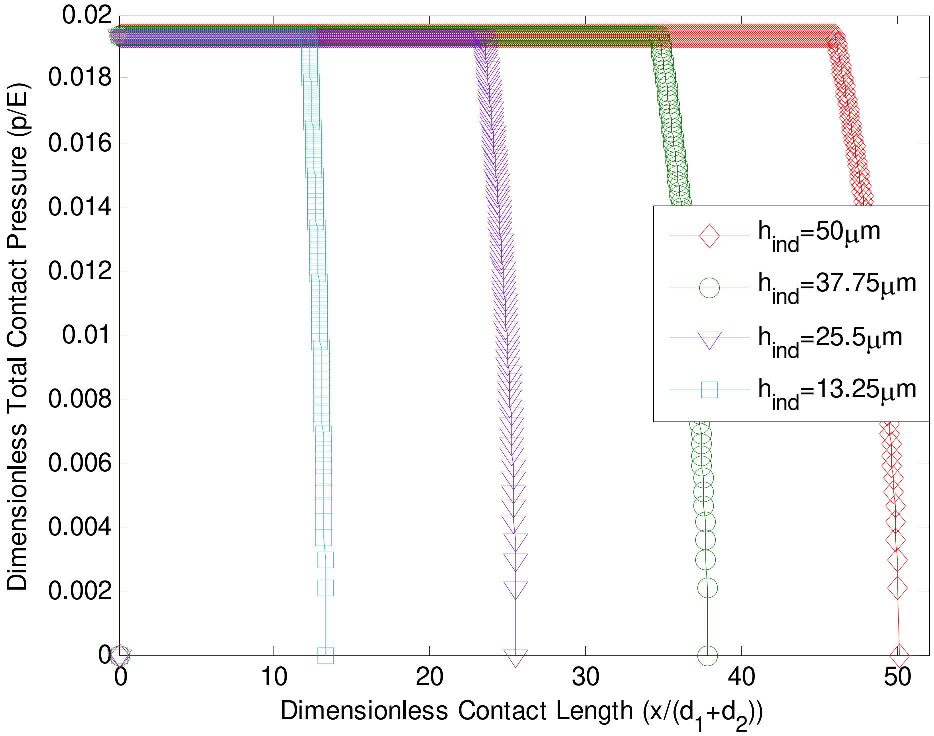

Figure 4.22: Dimensionless total contact pressure distribution for different indentation depths
$R_{edge} = 10\,\mu m, \alpha_n = 5^0, \gamma_n = -12^0$, $\phi 16$ mm ball – end cutter and AL7050 workpiece

The cutting edge indentation models introduced in Section 4.2 and Section 4.3 use mechanical properties of the work material i.e. E, σ_Y as inputs to evaluate total contact pressure distribution in indentation zone. These material properties vary with temperature, and the material is no longer at room temperature in indentation region. Therefore, the effect of temperature rise on material properties is considered in the following section.

4.4 Effect of Workpiece Temperature on Indentation Models

The temperature rise in the workpiece is assumed to have two components: temperature rise due to shearing, and, plastic deformation caused by the indentation. The combined effect of both factors can be expressed as,

$$\Delta T_{Workpiece} = \underbrace{\Delta T_{Shear}}_{due\ to\ f_h\ and\ \left(f_v\right)_{shear}} + \underbrace{\Delta T_{Indentation}}_{due\ to\left(f_v\right)_{indentation}} \tag{4.29}$$

where, f_h, $(f_v)_{shear}$, $(f_v)_{indentation}$ are horizontal feed per tooth, the portion of the vertical feed per tooth contributing to chip generation and the rest of the vertical feed per tooth causing indentation, respectively. The temperature prediction in ball-end milling is still an active research topic, and is not within the main scope of this study; hence the analytical model proposed by Komanduri et. al [52] for shear plane temperature, and workpiece temperature rise under tool flank face is adapted to ball-end milling problem in order to estimate the temperature rise in indentation zone due to shearing. The temperature rise in the workpiece can be obtained using the following equation [52],

$$\Delta T_{Shear}(x,z) = \frac{q_{pl}}{2\pi\lambda} \int_{l_i}^{L_s} e^{-\left(x - l_i \sin\varphi\right) V_c / 2a} \left\{ \begin{array}{l} K_0\left[\dfrac{V_C}{2a}\sqrt{\left(x - l_i \sin\varphi\right)^2 + \left(z - l_i \cos\varphi\right)^2}\right] \\ +K_0\left[\dfrac{V_C}{2a}\sqrt{\left(x - l_i \sin\varphi\right)^2 + \left(z + l_i \cos\varphi\right)^2}\right] \end{array} \right\} dl_i \tag{4.30}$$

where, q_{pl} is the heat generation intensity of shear plane heat source, λ thermal conductivity of the work material, φ inclination angle of shear plane heat source, L_s length of shear plane; V_c cutting speed; a thermal diffusivity of work material; K_0 modified zero order Bessel Function of second kind; and x and z are coordinates of the point where the temperature rise is sought. The main inputs of the solution are q_{pl}, L_s, V_c, and φ that is complementary angle of shear angle. In indentation region, those inputs can be calculated as follows,

$$q_{pl}\left(\phi,z\right)=\frac{\left(\tau_s\left(\phi,z\right)A_s\left(\phi,z\right)\right)V_s\left(\phi,z\right)}{A_s\left(\phi,z\right)}=\tau_s\left(\phi,z\right)V_s\left(\phi,z\right) \tag{4.31}$$

$$L_s\left(\phi,z\right)=\frac{h\left(\phi,z\right)}{\sin\phi_n\left(\phi,z\right)\cos i(z)} \tag{4.32}$$

$$V_C(z)=2\pi R(z)n \tag{4.33}$$

where, $\tau_s\left(\phi,z\right)$, $\phi_n\left(\phi,z\right)$ are already given in material database as explained in Section 3.2.2, local helix angle $i(z)$, and local cutter radius $R(z)$ can be calculated from Eq. (3.4) and Eq. (3.3) correspondingly. The shear velocity can be obtained by solving the velocity vector balance in oblique cutting [8] as,

$$V_s\left(\phi,z\right)=V_C(z)\left(\frac{\sin i(z)}{\dfrac{\tan i(z)\cos\phi_i\left(\phi,z\right)\sin\phi_n}{\cos\gamma_n(z)}+\sin\phi_i\left(\phi,z\right)}\right) \tag{4.34}$$

where, oblique shear angle $\phi_i\left(\phi,z\right)$ can be expressed as [53],

$$\phi_i\left(\phi,z\right)=\frac{\tan i(z)\sin\beta_n\left(\phi,\mathrm{z}\right)}{\cos\left(\phi_n\left(\phi,z\right)+\beta_n\left(\phi,\mathrm{z}\right)-\gamma_n(z)\right)} \tag{4.35}$$

where, $\beta_{\mathrm{n}}(\phi, z)$ is the normal friction angle and can be evaluated using the average friction angle $\beta_a(\phi, \mathrm{z})$ given in Eq. (3.21) by,

$$\beta_n(\phi, \mathrm{z}) = \tan^{-1}\left(\tan \beta_a(\phi, \mathrm{z}) \cos i(z)\right) \tag{4.36}$$

As given in Eqs. (4.31) to Eq. (4.36), the parameters used in workpiece temperature prediction vary in radial and angular directions. Hence, averaged values of the parameters are used to estimate workpiece temperature rise due to shearing in indentation region.

In order to obtain the average value of parameters, the engagement in indentation region is discretized both in angular and axial directions. After calculating the parameters at each discretized point, they are averaged, and are inserted into Eq. (4.30). While adapting the approach into ball-end milling case, all the assumptions made in [52] are followed.

i. The friction heat source on rake face of the cutter has no effect on workpiece temperature rise,
ii. The heat exchange between the environment and the work material is ignored (adiabatic conditions).

These assumptions essentially support that the shear plane heat source is inside the work material; therefore the temperature of the workpiece and the chip are affected from heat generation on shear plane. In addition to these assumptions, the cooling cycle due to intermittent cutting in milling is ignored as well, and it is assumed there is no wear on the flank face. An example for workpiece temperature rise is given in Figure 4.23. As seen, while the distance between the temperature rise calculation point and the shear plane increases, the temperature rise decreases and becomes zero at sufficiently far points.

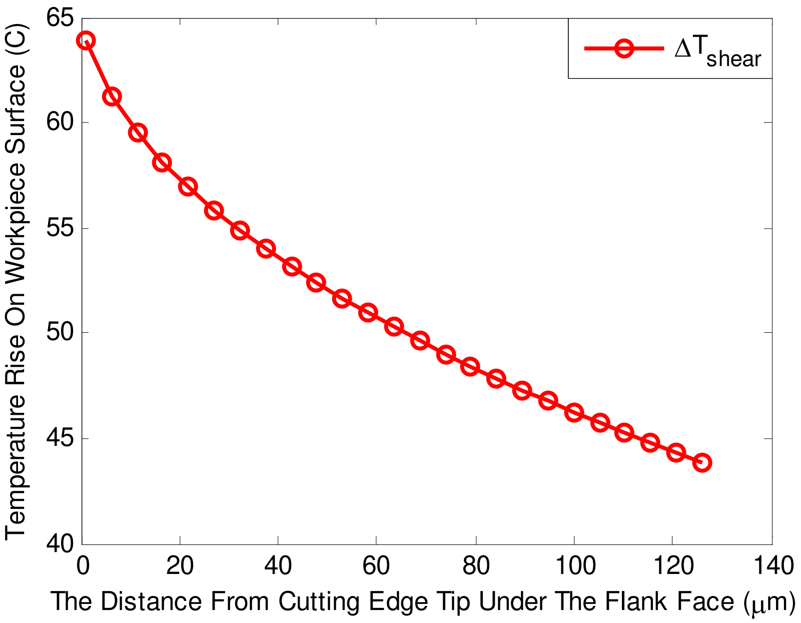

Figure 4.23: An example of workpiece temperature rise distribution under the flank face for; $f = 0.1\,\mathrm{mm/rev/tooth}, n = 7000\,\mathrm{rpm}, \alpha = 30^0, \alpha_n = 5^0, \gamma_n = 10^0$ $\phi 16\,\mathrm{mm}$ 2-fluted ball-end cutter and AL7050 workpiece

As given in Eq. (4.29), another heat source for workpiece is the heat generated by plastic deformation under the flank face, i.e. indentation. This temperature rise can be calculated as follows [54];

$$\left.\begin{aligned} &\eta_p \Delta W = \Delta Q \\ &\eta_p \int_0^{\varepsilon} \sigma d\varepsilon = \rho c_p \Delta T_{Indentation} \\ &\Delta T_{Indentation} = \frac{\eta_p}{\rho c_p} \int_0^{\varepsilon} \sigma d\varepsilon \end{aligned}\right\} \tag{4.37}$$

where, ΔW is the work done during plastic deformation; η_p percent of the work done converted to heat; ΔQ generated heat due to plastic deformation; ρ density of work material; c_p specific heat of the work material and σ, ε are the true stress and strain, respectively. Since σ, ε cannot be calculated analytically, the contribution of indentation to the workpiece temperature rise is modeled using FE, and presented in Chapter 5.

4.5 Integration of Cutting Tool Indentation Model into Cutting Force Model in Three and Five-Axis Ball-End Milling

In three-axis ball-end milling, the indentation takes place in the presence of vertical feed vector $\boldsymbol{f}_v$, as illustrated in Figure 4.24. Respecting the tool coordinate system at each map point explained in Section 3.2.2, indentation takes place when the following condition is satisfied,

$$\begin{aligned}
&(\boldsymbol{f}_L)_{\boldsymbol{TCS}_i} = f_x \boldsymbol{i}_{\boldsymbol{TCS}_i} + f_y \boldsymbol{j}_{\boldsymbol{TCS}_i} + f_z \boldsymbol{k}_{\boldsymbol{TCS}_i} \\
&(\boldsymbol{f}_v)_{\boldsymbol{TCS}_i} = f_z \boldsymbol{k}_{\boldsymbol{TCS}_i} \\
&\text{if} \quad f_z < 0
\end{aligned} \tag{4.38}$$

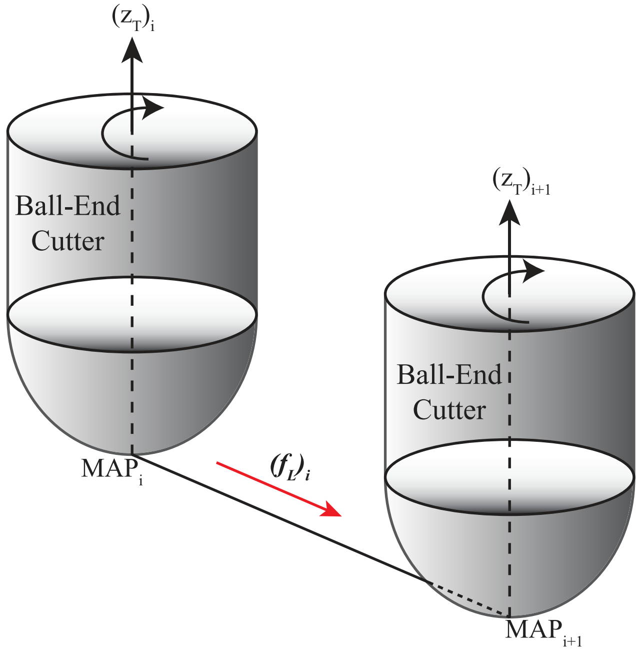

Figure 4.24: Indentation occurrence condition in three-axis ball-end milling

The linear feed/tooth vector $(\boldsymbol{f}_L)_{\boldsymbol{TCS}_i}$ is already evaluated at each map point for cutting force calculation, and the sign of its z-component determines whether there is indentation or not.

In five-axis ball-end milling, an analogy can be drawn with three-axis as the main reason for indentation has been attributed to low cutting speed. At any position, the tool axis and linear feed/tooth vector form a plane as shown in Figure 4.25. In order to check the indentation, the motion of the cutter needs to be considered in this plane that resembles the condition introduced for three-axis case. This condition can be reformulated for five-axis case as follows,

$$
\begin{aligned}
&\left(\boldsymbol{f}_{tot}(z)\right)_{\boldsymbol{TCS}_i}=\frac{\phi_p}{2\pi n}\left(\left(\boldsymbol{F}_A(z)\right)_{\boldsymbol{TCS}_i}+\left(\boldsymbol{F}_L\right)_{\boldsymbol{TCS}_i}\right)\\
&\Phi_{TCS_i}=\tan^{-1}\left(\frac{\left\|\left(\boldsymbol{f}_{tot}(z)\right)_{\boldsymbol{TCS}_i}\times\left(\boldsymbol{z}_T\right)_i\right\|}{\left(\boldsymbol{f}_{tot}(z)\right)_{\boldsymbol{TCS}_i}\bullet\left(\boldsymbol{z}_T\right)_i}\right)\\
&\text{if }\ \Phi_{TCS_i}>\frac{\pi}{2}\\
&f_v=\left|\left(\boldsymbol{f}_{tot}(z)\right)_{\boldsymbol{TCS}_i}\bullet\left(\boldsymbol{z}_T\right)_i\right|
\end{aligned}
\tag{4.39}
$$

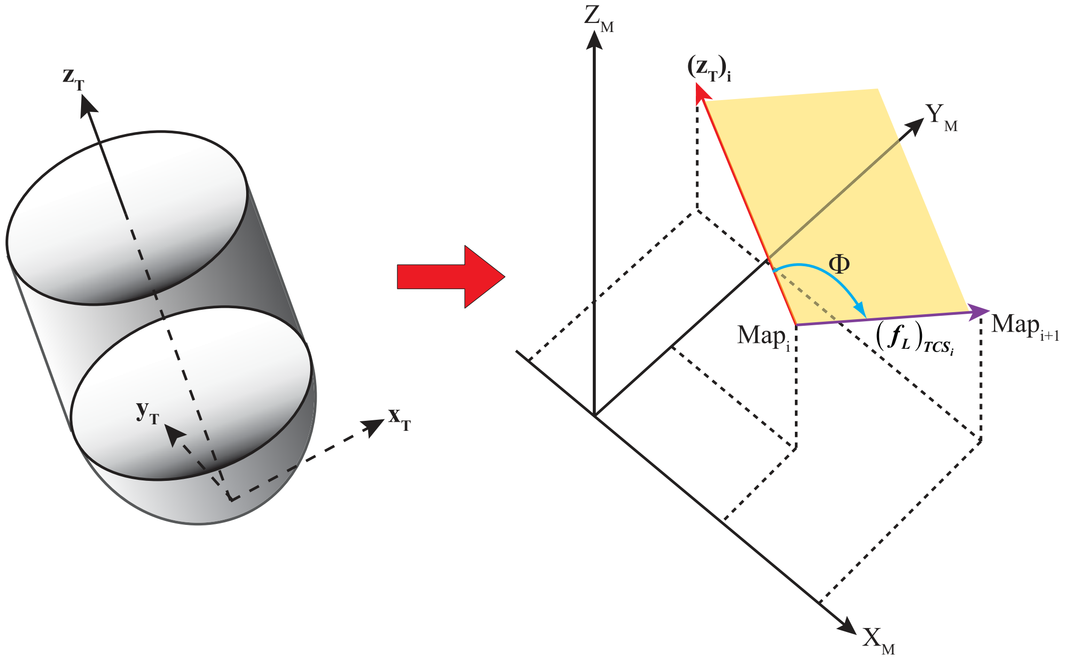

Figure 4.25: Indentation occurrence condition in five-axis ball-end milling

In Eq. (4.39), the effect of angular feed on indentation can be ignored since it is assumed in Section 3.2.4 that the rotational motions of the cutter are made about an axis passing through the tool tip. Moreover, when the angular feed is taken into account, calculation of max indentation depth along the cutter axis, f_v, becomes an iterative procedure. Therefore, Eq. (4.39) can be reduced to following without losing accuracy,

$$\begin{aligned}
&(\boldsymbol{f}_L)_{\boldsymbol{TCS}_i} = \frac{\phi_p}{2\pi n}(\boldsymbol{F}_L)_{\boldsymbol{TCS}_i} \\
&\Phi_{TCS_i} = \tan^{-1}\left(\frac{\left\|(\boldsymbol{f}_L)_{\boldsymbol{TCS}_i} \times (\boldsymbol{z_T})_i\right\|}{(\boldsymbol{f}_L)_{\boldsymbol{TCS}_i} \bullet (\boldsymbol{z_T})_i}\right) \\
&\text{if } \Phi_{TCS_i} > \frac{\pi}{2} \\
&f_v = \left|(\boldsymbol{f}_L)_{\boldsymbol{TCS}_i} \bullet (\boldsymbol{z_T})_i\right|
\end{aligned} \tag{4.40}$$

The angle Φ is the angle between linear feed/tooth $\boldsymbol{f_L}$ and unit tool axis $\boldsymbol{z_T}$ vectors as shown in Figure 4.25.

In the cutting force model (Eq. (3.11)), the forces resulting from non-cutting actions were named as edge forces in Section 3.2.2, and their impact is proportional to cutting edge length in cut region. Similarly, the additional force arising from indentation is a non-cutting force, and can be classified as indentation edge force. The indentation edge force acting in radial direction was already calculated per unit cutting edge length in indentation zone using Eq. (4.18). This force component is integrated into existing force model as follows,

$$\begin{aligned}
&dF_r(\phi) = K_{rc}(z)h_j(\phi, z)\,db(z) + K_{re}(z)\,dS(z) \\
&dF_{ind}(z) = K_{ind}(z)\,dS(z) \\
&(dF_r)_{tot}(\phi) = K_{rc}(z)h_j(\phi, z)\,db(z) + \left(K_{re}(z) + K_{ind}(z)\right)dS(z)
\end{aligned} \tag{4.41}$$

where, K_{ind} (N/mm) is called indentation force coefficient in radial direction.

The overall algorithm of how the indentation is checked along three and five-axis toolpaths, and how the algorithm is merged with existing force model is summarized in Figure 4.26.

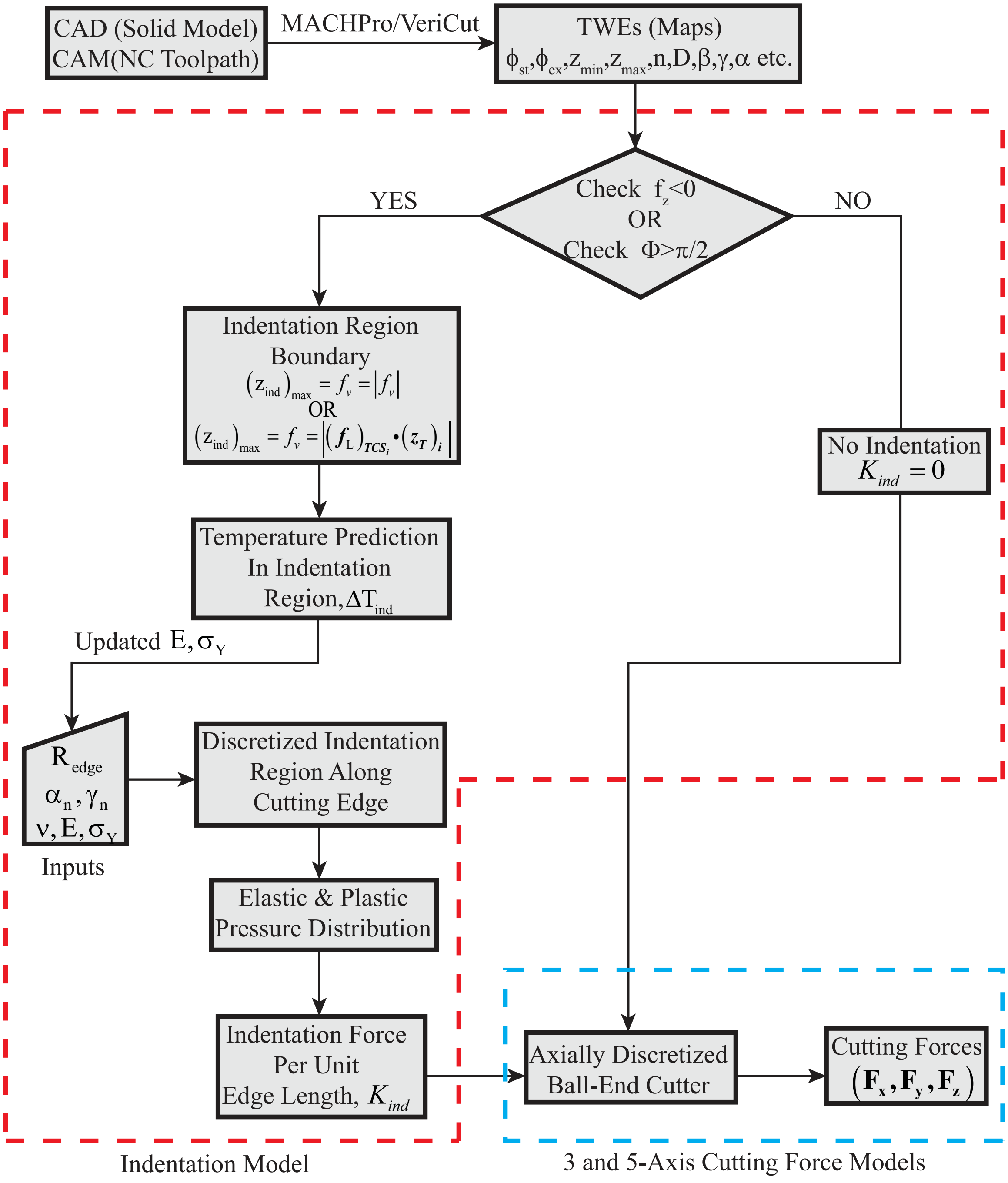
CAD (Solid Model)
CAM(NC Toolpath)
MACHPro/VeriCut
TWEs (Maps)
$\phi_{st}, \phi_{ex}, z_{min}, z_{max}, n, D, \beta, \gamma, \alpha$ etc.
Check $f_z<0$
OR
Check $\Phi>\pi/2$
YES
NO
Indentation Region Boundary
$(z_{ind})_{max} = f_v = |f_v|$
OR
$(z_{ind})_{max} = f_v = |(f_L)_{TCS_i} \cdot (z_T)_i|$
No Indentation
$K_{ind} = 0$
Temperature Prediction In Indentation Region, ΔT_{ind}
Updated E, σ_Y
R_{edge}
α_n, γ_n
ν, E, σ_Y
Inputs
Discretized Indentation Region Along Cutting Edge
Elastic & Plastic Pressure Distribution
Indentation Force Per Unit Edge Length, K_{ind}
Axially Discretized Ball-End Cutter
Cutting Forces
$(\mathbf{F_x}, \mathbf{F_y}, \mathbf{F_z})$
Indentation Model
3 and 5-Axis Cutting Force Models

Figure 4.26: Flow chart for integration of indentation model into three and five-axis cutting force models

Using the algorithm, the cutting forces for the experimental conditions given in Figure 3.16 are simulated again and presented in Figure 4.27. Since there is no indentation in the first case of down-ramping, the indentation model does not change the prediction results; however for

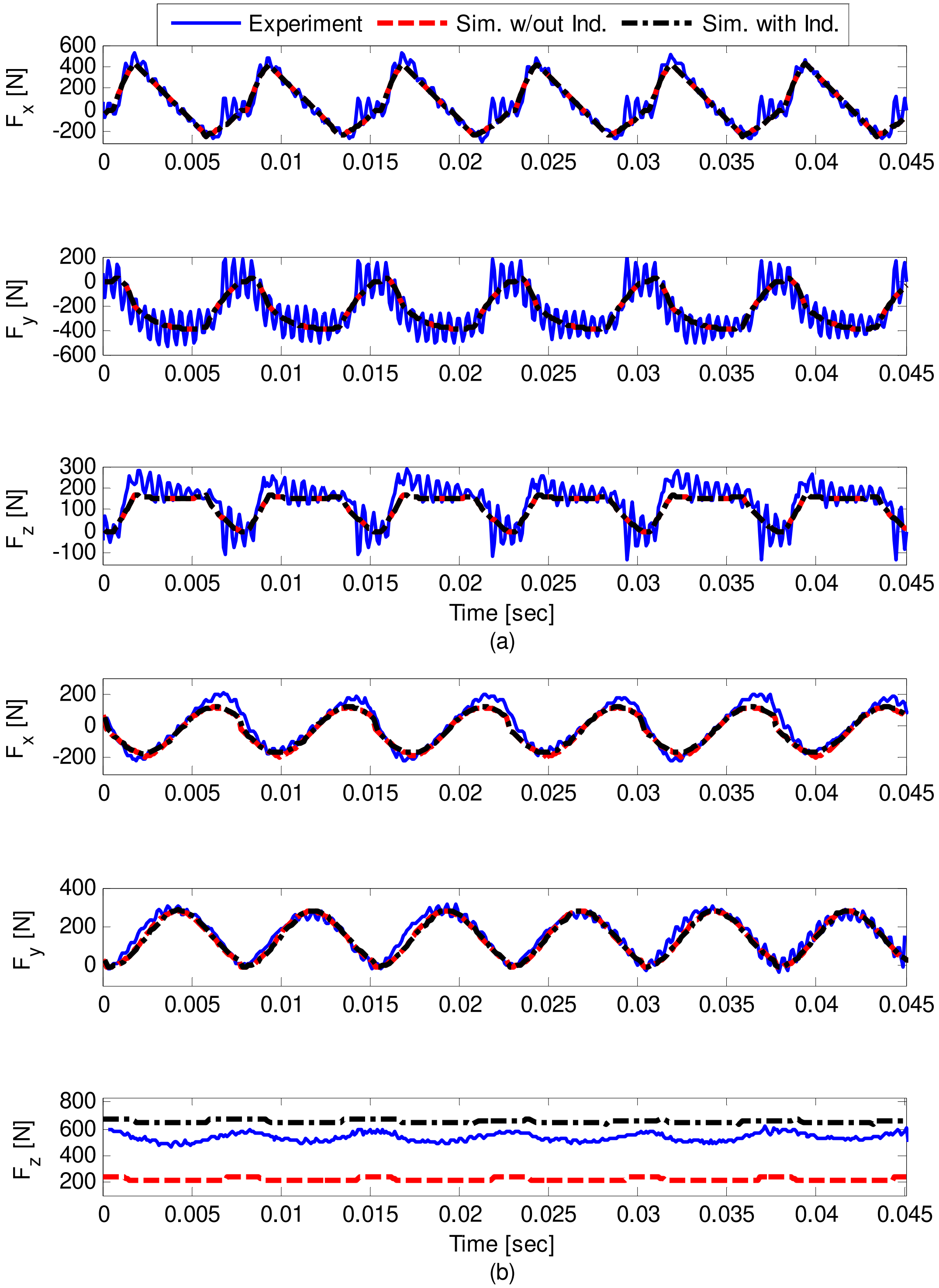

Figure 4.27: Comparison of experimental and predicted forces for 2 cases of downward direction inclined surface ball-end milling for $R_0 = 8\,\mathrm{mm}$, $f = 0.1\,\mathrm{mm/rev/tooth}, N = 2$ $n = 4000\,\mathrm{rpm}$, AL7050 workpiece a) $\alpha = 45^0, a_p = 2\,\mathrm{mm}$ b) $\alpha = 30^0,\ a_p = 5\,\mathrm{mm}$

the second case of down-ramping in which low speed region of the tool is in contact with the workpiece the predictions in z-direction has remarkable improved, and the prediction error has become 10% that is quite reasonable for milling applications.

4.6 Summary

In this chapter, a new indentation model is developed to address the penetration problem arising from low cutting speed region on the ball-end cutter. Geometrical properties of the cutter $\left(R_{edge}, \alpha_{\mathrm{n}}, \gamma_{\mathrm{n}}\right)$ and mechanical properties of the work material $\left(\nu, E, \sigma_{\mathrm{Y}}\right)$ are specified as inputs for the analytical contact model that can calculate additional indentation forces acting on the cutter. This is done for two possible geometries of the cutting flute (i.e. cutter with positive and negative rake angles) to obtain a general model. Also, the effect of temperature on material properties those have direct impact on the solution in indentation zone is shown.

In the following chapter, the constant C that is used in analytical contact pressure predictions is obtained from FE modeling, and analytical and numerical (FE) results are compared. Moreover, the contribution of indentation to temperature rise in indentation zone is achieved using FE modeling.

5 Finite Element (FE) Modeling of Cutting Edge Indentation

5.1 Introduction

Finite Element (FE) simulations have extensively been used to simulate and investigate the different aspects of indentation mechanism [55], [56], [57], [58] and [59]. In this chapter, the Finite Element Method (FEM) is used to simulate the cutting edge indentation to obtain the coefficient C that characterizes the plastic contact; and, to quantify the contribution of cutting edge indentation to workpiece temperature rise in indentation region. FE simulations are carried out for different cutting edge geometries and indentation depths to obtain the constant C for an aluminum alloy (AL7050) that is employed in verification cutting tests. Once the coefficient C is calibrated, the analytical (the model developed in Chapter 4) and the numerical (FE) contact pressure predictions are compared. Also, the rise in work material temperature due to indentation is obtained at a range of local surface inclination angles and feedrates. Since the thermal effect is material specific as well, it is investigated only for the same aluminum alloy. Although the analysis in this chapter is limited to AL7050, the developed FE model is a general method and can be applied for any cutting tool and work material combinations just by changing the tool geometry, and workpiece material parameters.

5.2 Finite Element Model of Contact Pressure Due to Cutting Edge Indentation

The proposed mechanics model in Chapter 4 utilizes inclined punch and wedge indentations to predict the contact pressure at cutting edge and work material interface. The deformation zone is classified as elastic and plastic regions. Based on the elastic-perfectly plastic work material model, the plastic contact pressure is quantified by the coefficient C that is calibrated for AL7050 by modeling the cutting edge indentation in FE environment. Details of the FE model and the procedure for obtaining the constant *C* are presented in subsections 5.2.1 and 5.2.2, accordingly.

5.2.1 Finite Element Model

The present study utilizes the commercial finite element code ABAQUS/Explicit®. In the FE model, the cutting edge is assumed to be a rigid body, and the workpiece is treated as an elastic-perfectly plastic material in plain strain and frictionless contact conditions. As the cutting edge is a rigid body, it is not necessary to model (mesh) the punch or wedge shaped cutting edge in the FE model, only the workpiece is meshed and its response is simulated. In order to find the best element type and the shape function for mesh elements of the workpiece, simulations are run with triangular and quadrilateral elements, and linear and quadratic shape functions for different cases are listed in Table 5.1. According to the results of the first runs, the representation of the workpiece is finalized in terms of meshing strategy. The selection criterion for the best combination of element type and shape function is decided to be the minimum number of elements for rounded part of the cutting edge element that can completely capture the material behavior around the edge radius and provide accurate simulation results in turn. At model development stage, two different meshing type, two distinct plane elements, and two different shape functions for a fixed indentation depth are used. The details of tested strategies are given in Table 5.1 where “roundness” denotes the cutting edge radius, and adaptive meshing means remeshing.

Table 5.1: Details of different meshing strategies used at FE model development stage

NON-ADAPTIVE MESHING				
			Indentation Depth, h_{ind}	Edge Radius, R_{edge}
Triangular Element	Linear Shape Function (LSF)	1 Element For Roundness	21.4 μm	10 μm
		2 Elements For Roundness	21.4 μm	
	Quadratic Shape Function (QSF)	1 Element For Roundness	21.4 μm	
		2 Elements For Roundness	21.4 μm	
Quadrilateral Element	Linear Shape Function (LSF)	1 Element For Roundness	21.4 μm	
		2 Elements For Roundness	21.4 μm	
ADAPTIVE MESHING				
			Indentation Depth, h_{ind}	Edge Radius, R_{edge}
Triangular Element	Linear Shape Function (LSF)	1 Element For Roundness	21.4 μm	10 μm
		2 Elements For Roundness	21.4 μm	
Quadrilateral Element	Linear Shape Function (LSF)	1 Element For Roundness	21.4 μm	
		2 Elements For Roundness	21.4 μm	

Figure 5.1 shows the dimensions of the indented material with adaptive meshing and quadrilateral elements. The mesh elements around edge radius where the highest deformation takes place are generated by built-in adaptive algorithms in ABAQUS/Explicit®. Although the cutting edge indentation is a static process, dynamic solver is used in simulations to obtain the simulation results at each discrete time step. Also, explicit solver is employed, and possible instability of explicit solver is internally avoided by ABAQUS/Explicit® by defining small time steps for simulation process. FE analysis, in general, is carried out either with the force input and solving the system of equations for displacement, or with the displacement input and solving the system for forces. The problem modeled here belongs to the latter case as displacement (indentation depth) is known a priori and given as an input to the system.

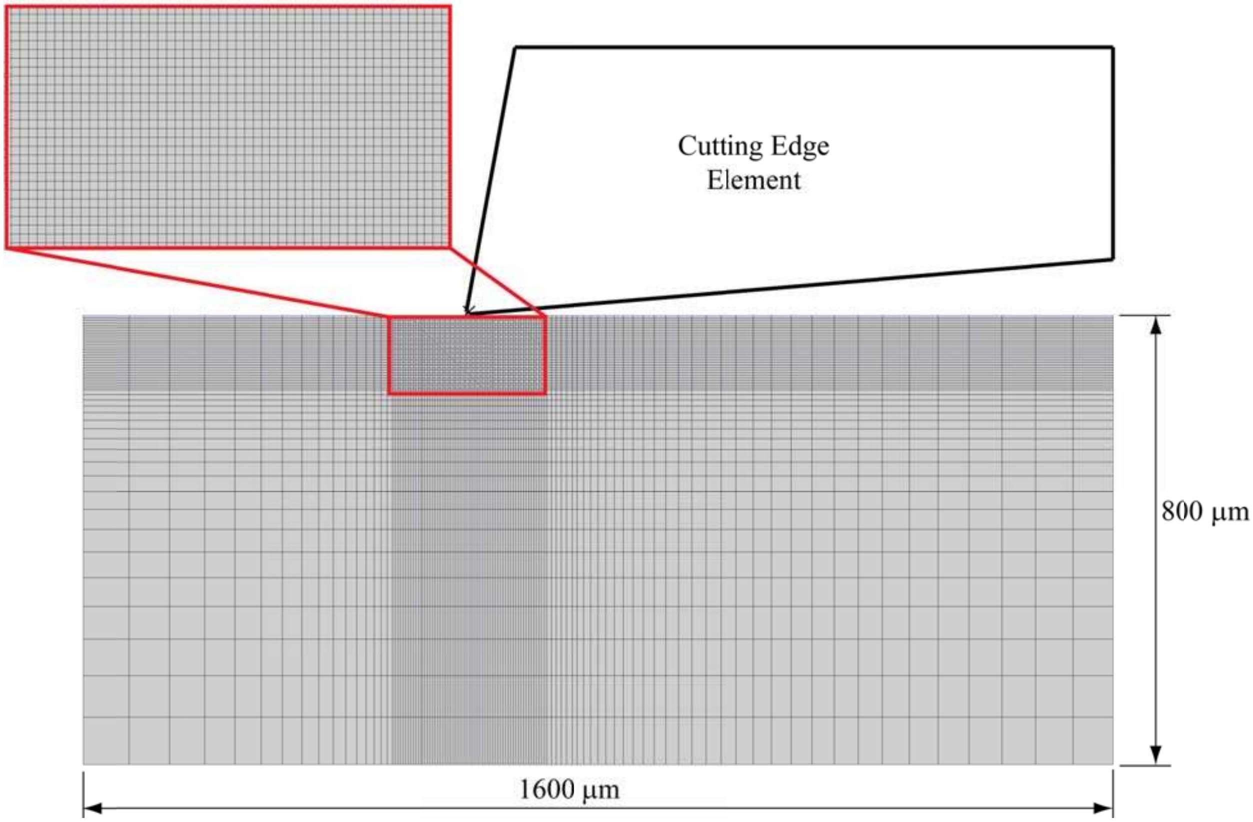

Figure 5.1: A sample meshing strategy for workpiece and dimensions of work material

Total contact pressure prediction using the different simulation conditions in Table 5.1 are presented in Figure 5.2 and Figure 5.3 in terms of ratio of the contact pressure to yield strength of AL7050 with dimensionless contact length for one and two mesh elements around rounded part of the cutting edge, respectively. Each simulation case in Table 5.1 converges and gives the theoretically expected result for constant *C* in fully plastic deformation conditions $\left(\frac{p}{\sigma_Y} \approx 2.5\right)$ corroborating that the developed FE model can simulate cutting edge indentation accurately. Even though both one and two elements for edge radius give pretty similar results, it is decided to use two elements model for further simulations since it can better capture the deformation around the rounded part for higher indentation depths. Comparison of one and two-element models is given in Figure 5.4, and for both models there is no excessive element distortion and element node inside the cutting edge.

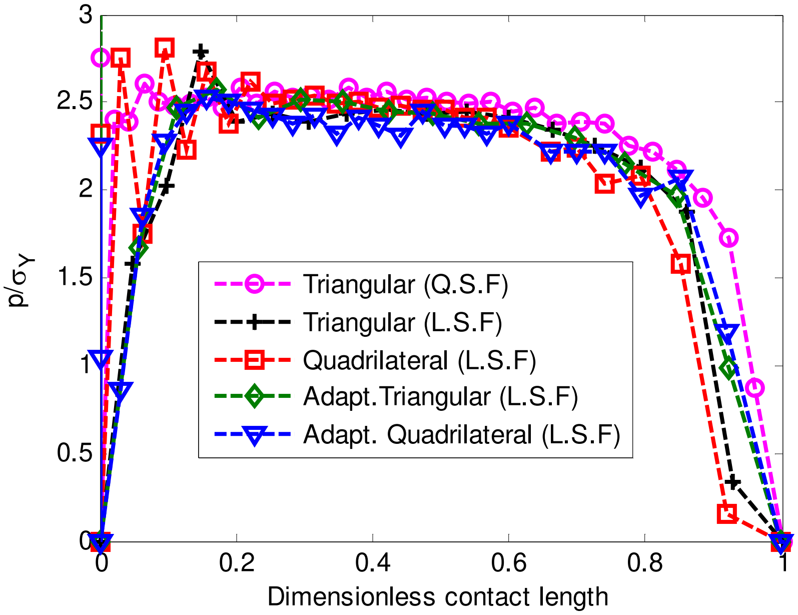

Figure 5.2: Dimensionless total contact pressure for AL7050 with one mesh element around edge radius

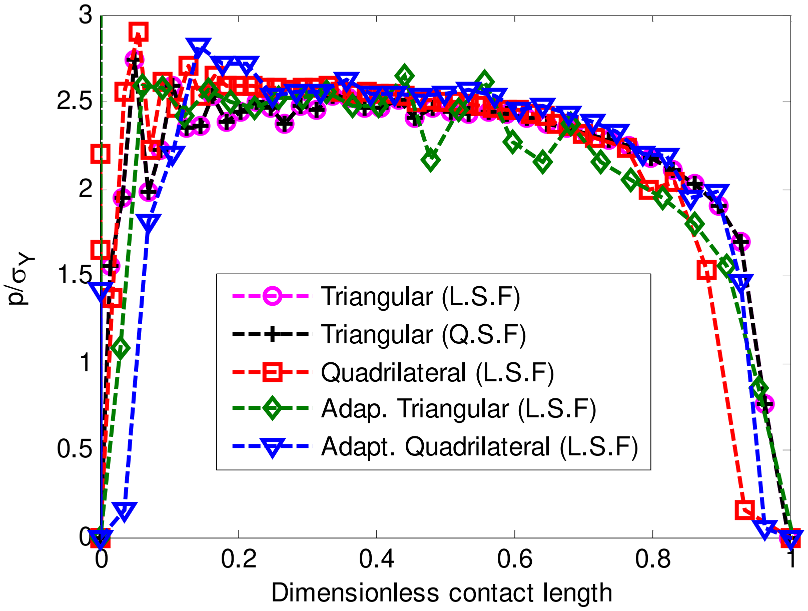

Figure 5.3: Dimensionless total contact pressure for AL7050 with two mesh elements around edge radius

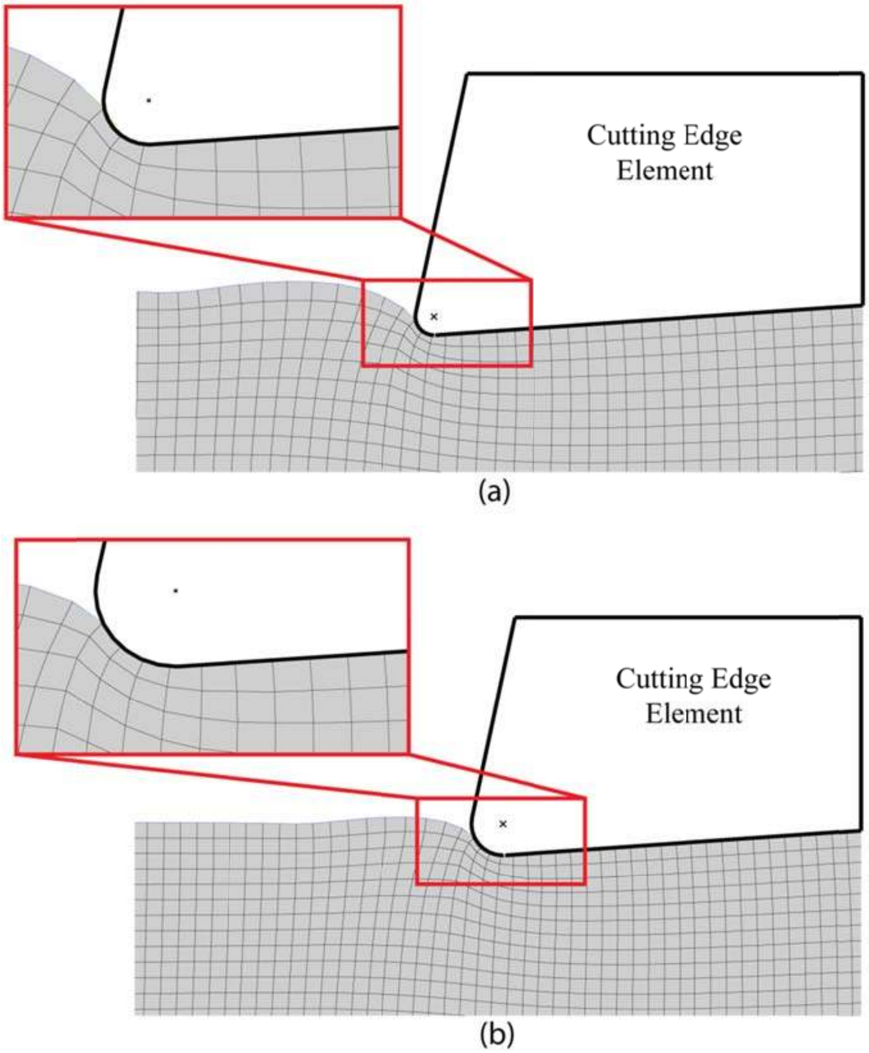

Figure 5.4: A sample deformation around edge radius; **(a)** with 1-element quadrilateral mesh **(b)** with 2-element quadrilateral mesh

In the light of the first runs, the FE model is fixed for cutting edge indentation as the one shown in Figure 5.1. The workpiece is represented by quadrilateral (four-noded) elements (CPE4R) with linear shape function since the workpiece is modeled as rectangle. The workpiece size is 1600x800 μm and it is composed of 5500 mesh elements. Remeshing is desired to avoid excessive distortion of elements that diverges the solution, and it is only limited to the region detailed in Figure 5.1 as the highest deformation occurs there. The density of the mesh gradually decreases with the distance from indentation zone and becomes coarse at unconcerned regions.

The boundary conditions imposed into the model are; constrained workpiece displacement, constrained tool velocity and rotation. Under these conditions, the nodes at the base of the workpiece are fixed (stationary) and the tool only moves downward to provide intended indentation. Since the contact is localized at the upper surface of the workpiece, the boundary condition imposed for the bottom surface of the workpiece does not affect the solution. This FE model is used to obtain the coefficient *C* for the plastic contact pressure in the analytical model introduced in Chapter 4.

5.2.2 Calibration of Coefficient *C* for AL7050

In cutting edge indentation, the plastic deformation is dominant over the elastic deformation; therefore the coefficient *C* has a direct effect on analytical contact pressure prediction. As it is the limiting value of the total pressure distribution, accurate calibration of this constant for a specific material is crucial in order to maintain high prediction accuracy. For that purpose, FE analysis is chosen as a tool in which all parameters can be readily controlled, and desired boundary conditions for the experiment can be imposed.

Calibration is carried out for a feasible range of cutting edge geometry and cutting parameters as given in cutter manufacturer's catalogues [60], [61], and is not valid for customized cutting tools. When a special purpose ball-end tool is used in an operation, the re-calibration for this specific cutter has to be done. In order to minimize this possibility, a wide range for cutter parameters is selected containing ball-end mills with negative and positive rake angles. As explained in Chapter 4, the coefficient *C* is friction, material, and indenter geometry dependent. Since the analytical model is developed for frictionless conditions, FE model is also built on the same assumption for the sake of consistency. Also, the calibration is done particularly for AL7050. These two limitations reduce C to be indentation geometry dependent only as given in Eq. (5.1).

$$\begin{aligned} C &= f(\text{Friction, Material, Geometry}) \\ C_{reduced} &= f(\text{Geometry}) = f\left(\frac{\mathrm{h}_{\mathrm{ind}}}{\mathrm{R}_{\mathrm{edge}}}, \gamma_{\mathrm{n}}, \alpha_{\mathrm{n}}\right) \end{aligned} \tag{5.1}$$

The selected feasible ranges for the parameters in Eq. (5.1) are given in Table 5.2.

Table 5.2: Selected feasible range for geometrical quantities

Indentation depth to edge radius ratio	**Rake Angle**	**Clearance Angle**
$\frac{\mathrm{h}_{\mathrm{ind}}}{\mathrm{R}_{\mathrm{edge}}}$ = 1.5, 3, 5, 8, 11, 14	$\gamma_{\mathrm{n}} = \left[-20^0, 20^0\right]$	$\alpha_{\mathrm{n}} = \left[0^0, 15^0\right]$

The indentation depth to edge radius ratio has an effect on indentation geometry, especially on the rake face side, and its range is determined by considering allowed minimum and maximum feed per tooth values (0.05 and 0.2 mm/rev/tooth) for standard ball-end cutters, and a feasible local surface inclination range. These two selection criteria and corresponding maximum indentation depths are given in Table 5.3.

Table 5.3: Maximum indentation depths domain for feasible local inclination angles and feed per tooth values

Local Inclination Angle (°)	**Feed per Tooth (mm/rev/tooth)**	**Max. Indentation Depth, h_{ind} (μm)**
15	0.05	12.94
	0.1	25.88
	0.15	38.82
	0.2	51.76
30	0.05	25.00
	0.1	50.00
	0.15	75.00
	0.2	100.00
45	0.05	35.35
	0.1	70.71
	0.15	106.06
	0.2	141.42

Since the local surface inclination less than 15^0 can be assumed as horizontal plane cutting and the inclination above 45^0 is no longer point milling, the definition of inclined surface in this study is limited to the local inclination range $\left[15^0, 45^0\right]$. Extremes of this interval lead to the indentation depth to edge radius ratios ≈ 1.5 and ≈ 14 for an average edge radius of brand-new cutters ($10\,\mu\text{m}$ measured in this study). New cutter gives the maximum range for $\frac{h_{ind}}{R_{edge}}$; hence $\frac{h_{ind}}{R_{edge}}$ is selected as given in Table 5.2 for *C* calibration. The FE model developed in Section 5.2.1 is used for the geometrical quantities in Table 5.2 with 5^0 increment for rake and clearance angles. Simulation result for the extreme case $\frac{h_{ind}}{R_{edge}} = 14$ is shown in Figure 5.5 as an example.

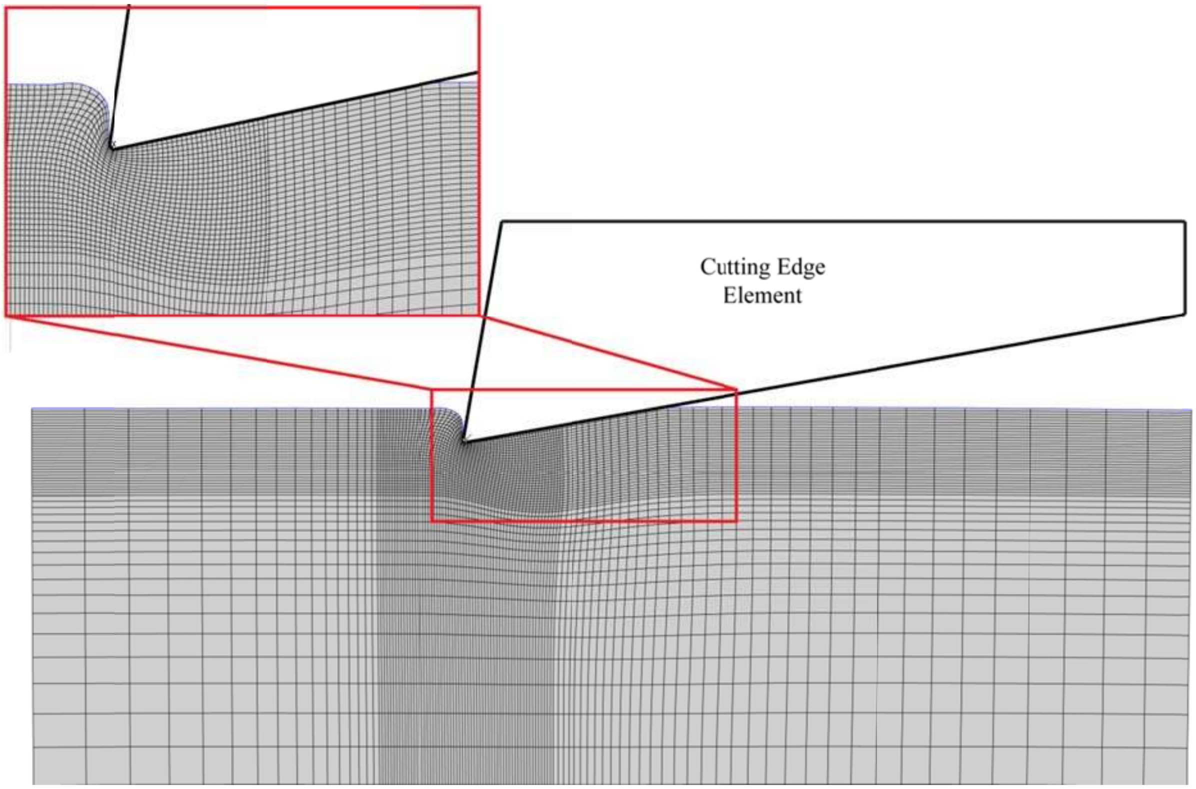

Figure 5.5: Sample FE simulation result for C calibration

In the calibration simulations, the elastic modulus at room temperature is employed because *C* is independent of elastic properties. Also, elastic-perfectly plastic material model of the workpiece allows to use the yield strength at room temperature since *C* is defined as the ratio of plastic contact pressure (which is constant) to material yield strength. The temperature of the indentation zone increases during cutting and causes the yield strength and plastic contact pressure to decrease; however $\frac{p_{plastic}}{\sigma_Y}$ remains the same. Hence, *C* is not affected by the temperature of the indentation region.

FE simulations are designed based on available standard cutter information, and when the simulations are extended to all of the cases in Table 5.2, in total 216 simulations are completed, and for each case the average coefficient *C* for fully plastic contact is obtained using the definition given in Eq. (4.16). FE calibration results are presented in Figure 5.6 where each data point has a contact pressure distribution as given in Figure 5.3. As evident, *C* has a decreasing trend with increasing $\frac{h_{ind}}{R_{edge}}$ which can be attributed to unequal change in the contact force and area (or length) due to non-linear variation of contact area.

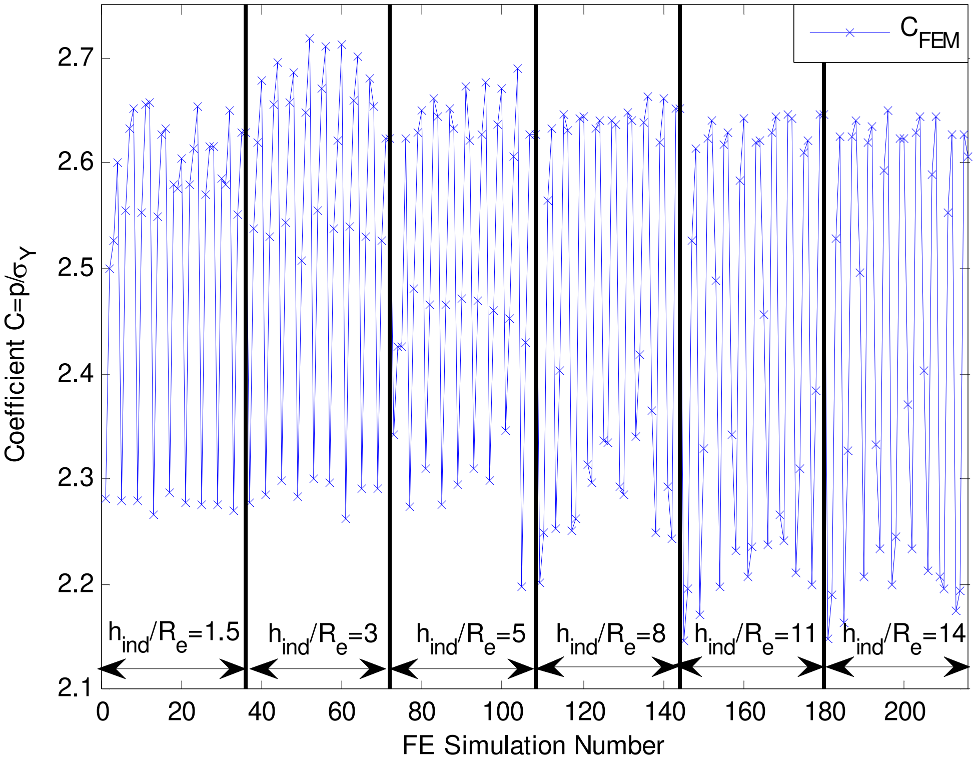

Figure 5.6: The calibration results for AL7050 extracted from FE simulations

In Figure 5.7, a detailed view of a section from $h_{ind}/R_{edge}=14$ is shown and that variation trend is present in the entire calibration domain. Between the points A, B, C and D clearance angle of the cutting edge is increasing from 0^0 to 15^0 while all the other geometrical parameters are fixed; and from points A to E, B to F, C to G and D to H the only varying parameter is rake angle (from -20^0 to 20^0). Clearly, higher clearance angles cause the coefficient *C* to increase from points A to D; on the other hand, rake angle does not seem to have a notable effect on *C* since it is not the dominant geometrical parameter in contact area variation under the limitation of maximum negative rake angle -20^0 in this study. If more negative rake angles were tried, rake face side would contribute to the contact area more and would affect *C* in turn.

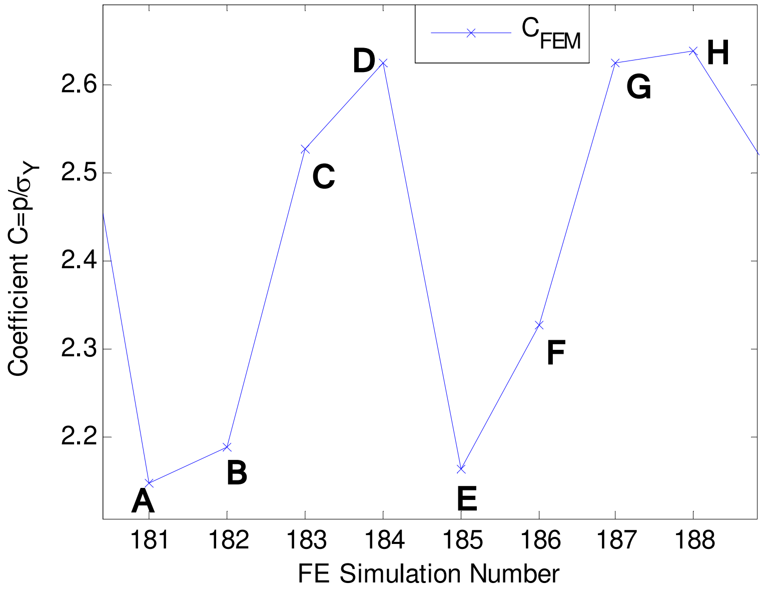

Figure 5.7: Details of FE calibration results for $h_{ind}/R_{edge}=14$

In order to provide a practical meaning to FE results, they are decided to be represented as a continuous function of the effective parameters in Figure 5.6. As shown, *C* varies almost periodically; thus utilizing the periodicity of the trigonometric functions, the following curve is fitted to FE results,

$$C = A_1 + A_2 \left| \cos\left(A_3 \left(\frac{h_{ind}}{R_{edge}} \right) + A_4 \gamma_n + A_5 \alpha_n + A_6 \right) \right|$$

where,

$$A_1 = 2.2380$$
$$A_2 = 0.4621 \tag{5.2}$$
$$A_3 = 0.9878$$
$$A_4 = 1.2553$$
$$A_5 = 1.6482$$
$$A_6 = 1.5281$$

In curve fitting analysis Eq. (5.2) is classified as non-linear in coefficients as it requires a non-linear curve fitting algorithm to find $A_q \, (i = 1.....6)$. Since developing a non-linear curve fitting algorithm is not within the scope of this thesis, a commercial program called Microsoft Solver® is used that is capable of doing non-linear curve fitting. Once the original data is extracted from FE, the shape of the desired fitting curve (trigonometric function) is given as input and the coefficients A_q are obtained. More importantly, Eq. (5.2) is not a global solution because the calculated coefficients are optimum solution around the initial guess for A_q. Thus, the curve fitting procedure was repeated to refine the solution until the absolute error between actual and fitted results stopped changing. As a result of this refinement procedure, the overall variation of the FE results is represented with 2.74% average absolute error and 9.72% maximum absolute error, and Eq. (5.2) is only valid within the range of the fitted data. Comparison of original FE results and fitted function is presented in Figure 5.8.

Using the fitted data, total contact pressure predictions of the analytical model introduced in Chapter 4 and numerical (FE) model are compared for positive and negative rake angle cases in Figure 5.9 and Figure 5.10, respectively.

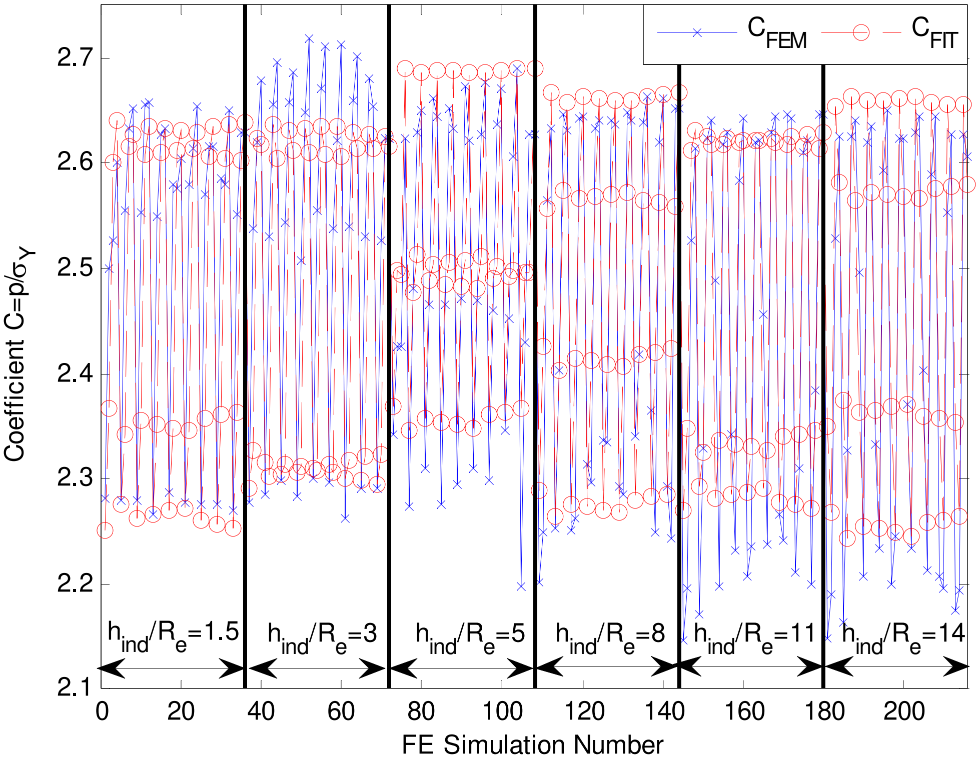

Figure 5.8: Original FE results and fitted function

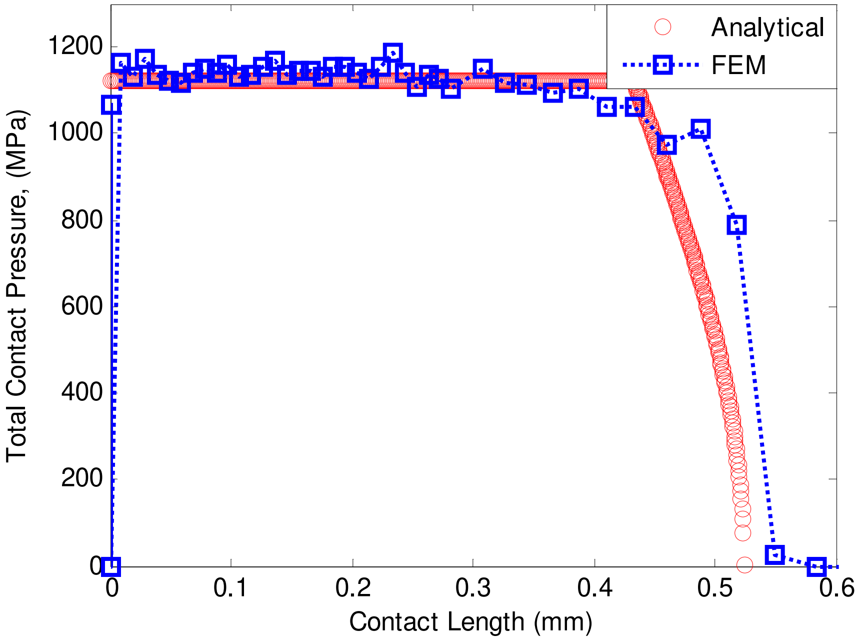

Figure 5.9: Comparison of FE and analytical total contact pressure distribution for; $h_{ind} = 50\,\mu m$, $\gamma_n = 10^0$, $\alpha_n = 5^0$

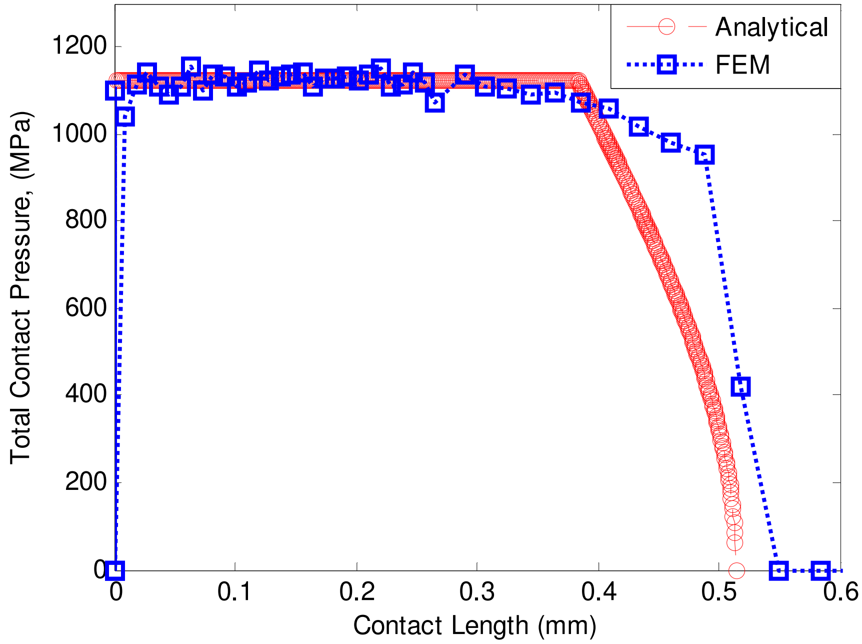

Figure 5.10: Comparison of FE and analytical total contact pressure distribution for; $h_{ind} = 50\,\mu m$, $\gamma_n = -15^0$, $\alpha_n = 5^0$

As expected, FE and analytical model results match within the plastic contact region since the output *C* of FE is given as input to the analytical model. Also, both models are in good agreement in the elastic contact region.

As explained in Section 4.4, there are two mechanisms affecting the temperature in indentation region, and the first mechanism (shearing) was already detailed in Section 4.4. The second mechanism that stems from plastic deformation is discussed in the following section

5.3 Finite Element Model of Workpiece Temperature Rise Due to Cutting Edge Indentation

In this section, the temperature rise in the work material (AL7050) is investigated using the FE model developed in Section 5.2.1 with some modifications. The purpose is to examine the relative contribution of indentation related temperature rise to the total temperature rise in the workpiece under the same boundary conditions defined in Section 5.2.1.

In order to run the simulations for temperature, the workpiece is represented with quadrilateral coupled temperature and displacement elements (CPE4RT) that account for temperature effect as well. This necessitates the explicit coupled temperature and displacement solver to be used, and thermal properties at room temperature are used rather than using temperature dependent ones due to explicit solver. Also, it is assumed that 90% of plastic deformation energy is converted to heat as suggested in [62].

The feasible cutting and indentation conditions given in Table 5.3 for different cutting edge geometries are used to study the temperature effect, and a sample FE simulation result is presented in Figure 5.11. As expected, the maximum temperature rise occurs at the contact region, and temperature rise continuously decreases with the distance from the contact area and finally workpiece temperature becomes equal to the room temperature which is taken as 24^0C in this study.

When FE simulations are run for different cutting edge geometries as outlined in Table 5.2, it is observed that the geometry does not have a notable effect on temperature rise at workpiece surface because of indentation. Therefore, only three sets of the results are summarized in Figure 5.12 for clarity.

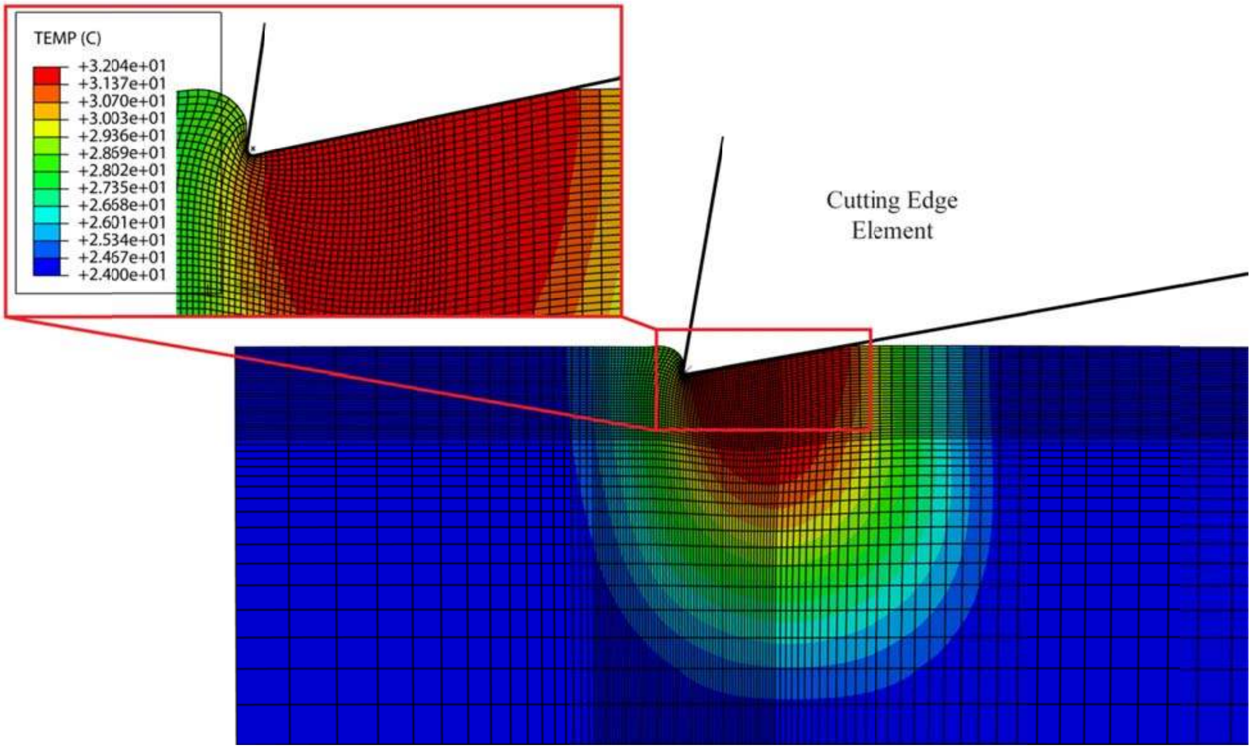
TEMP (C)
+3.204e+01
+3.137e+01
+3.070e+01
+3.003e+01
+2.936e+01
+2.869e+01
+2.802e+01
+2.735e+01
+2.668e+01
+2.601e+01
+2.534e+01
+2.467e+01
+2.400e+01
Cutting Edge Element

Figure 5.11: FE simulation of workpiece temperature rise for; AL7050, $h_{ind} = 50\,\mu m$, $\gamma_n = 10^0$, $\alpha_n = 10^0$

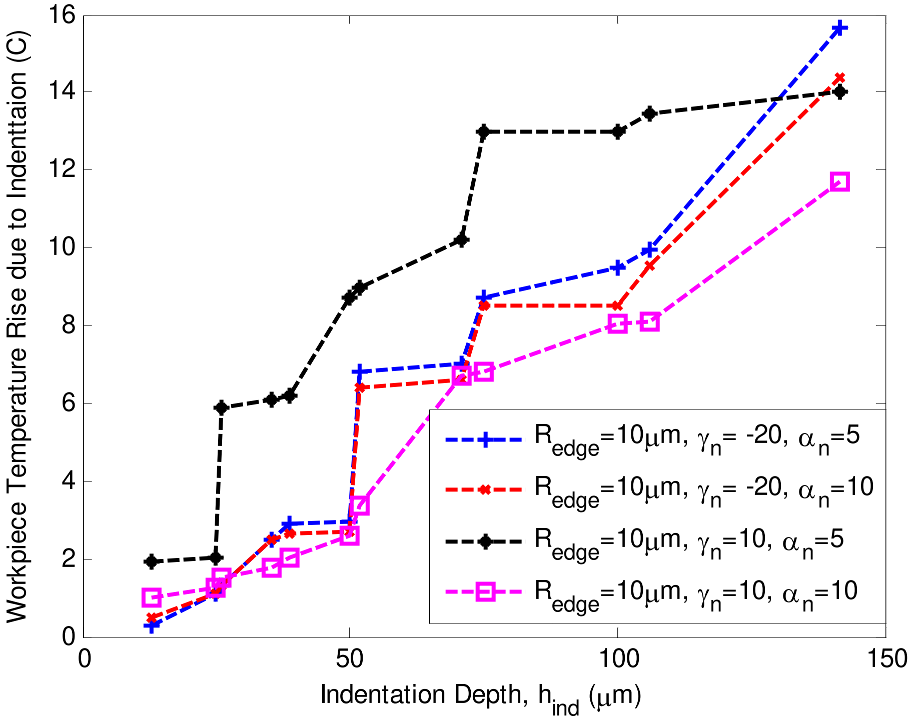

Figure 5.12: FE workpiece temperature rise results for AL7050 with different cutting edge geometries

As shown, temperature rise on the workpiece surface increases as a function of indentation depth, since bigger depths cause higher deformations. More importantly, temperature rise of the workpiece due to indentation is quite low compared with Figure 4.23 where average surface temperature rise due to shearing was estimated as $\approx 55^0\mathrm{C}$ for $f = 0.1\,\mathrm{mm/rev/tooth}$, $\alpha_n = 30^0$ ($50\mu\mathrm{m}$ indentation depth). However, for the same indentation depth the temperature increase in Figure 5.12 is less than $10^0\mathrm{C}$ for all geometries.

The effect of edge radius and material type on workpiece surface temperature rise due to indentation is given in Figure 5.13. For AL7050, a higher edge radius increases the temperature rise which can be attributed to increase in thickness of plastically deformed layer under the workpiece surface [62]. Also, for the same geometry, AISI 1045 steel gives higher temperature rise than AL7050 since AISI 1045 has a lower thermal conductivity than AL7050 that leads to localized heat.

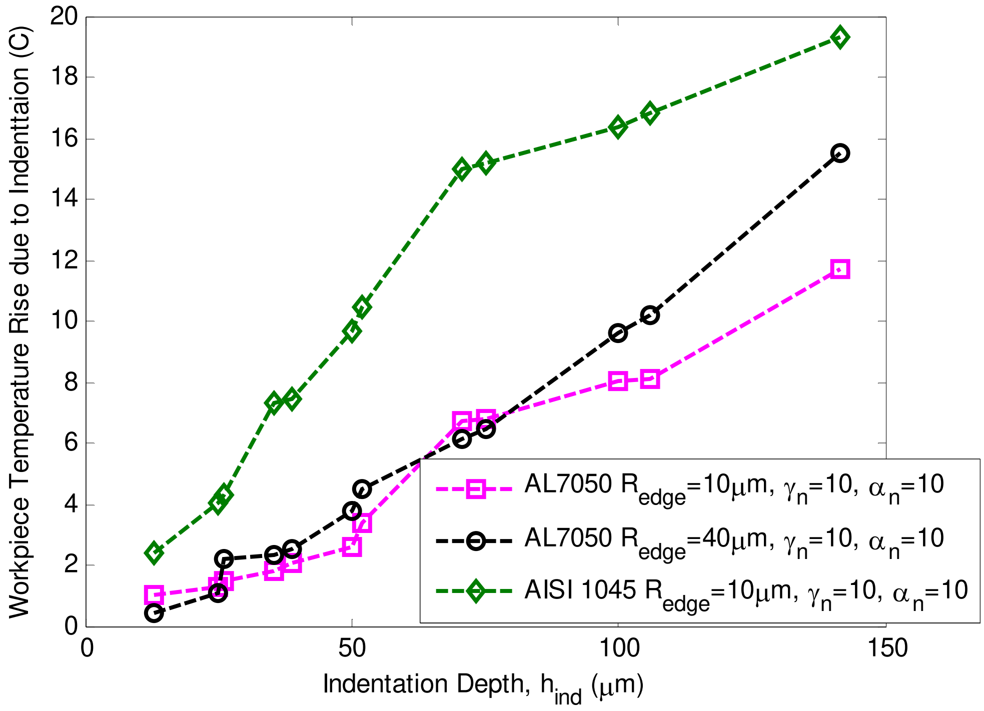

Figure 5.13: Comparison of workpiece temperature rise for 2 different geometries and materials

With the above discussion in mind, it can be said that, the workpiece temperature increase due to the cutting edge indentation is fairly low for AL7050 alloy. Other than the geometry of the indenter, indentation speed contributes to the temperature rise; however the indentation speed is also sufficiently low due to low vertical feed per tooth. Furthermore, elastic-perfectly plastic material model does not consider deformation rate effect. Hence, even at high spindle speeds, we would get approximately the same temperature results shown in Figure 5.12 and Figure 5.13 with the current material model. Therefore, the effect of indentation on workpiece temperature can either be neglected or taken as an average value $\left(\approx 10^0\mathrm{C}\right)$ for AL7050 within the domain defined in Table 5.2. In this study, the first option is followed and this effect is not considered in calculations. In case, this effect needs to be included, then, the workpiece temperature rise due the cutting edge indentation can be substituted into Eq. (4.29).

5.4 Summary

In this chapter, the analytical indentation model is complemented by obtaining the coefficient *C* in plastic contact pressure prediction by developing a two-dimensional (2D) FE model in commercial platform ABAQUS/Explicit®. The FE model considers the cutting edge as a rigid body and simulates the deformation of the work material whose behavior is assumed to be elastic-perfectly plastic. *C* is calibrated for a feasible range of cutting edge geometry and cutting conditions defined by the tool manufacturers. In order to make FE calibration results a practical tool to be used in process simulations, a curve fitting method is applied to represent the calibration data by a continuous function. Once this function is obtained, analytical and numerical total contact pressure distributions are compared, and they show a good agreement both in plastic and elastic contact regions. Also, the effect of indentation on workpiece surface temperature rise is investigated for the material (AL7050) used in the model verification phase, and concluded that this effect can either be ignored or replaced by a constant (average) temperature rise to increase the calculation accuracy.

In the following chapter, the analytical model is validated by comparing the results of cutting experiments against the predictions of the developed analytical model.

6 Experimental Verification

6.1 Introduction

Several cutting experiments have been conducted to verify the proposed ball-end milling force prediction model. The experiments have been conducted on Mori Seiki NMV5000 five-axis milling center. The experiments have been grouped as: plunge milling; three-axis inclined surface machining; three-axis free-form surface machining; and, five-axis airfoil surface machining with ball-end mill. The cutting conditions used in the experiments are given in Table 6.1, and each experiment was repeated twice to check the repeatability of the results. The specifications of the ball-end mill used in all experiments are given in Table 6.2.

Table 6.1: Details of model verification experiments

Experiment Name	Spindle Speed [rpm]	Linear Feed [mm/rev/tooth]	Axial depth/Drilling depth [mm]
Plunge Milling 1	3000	0.04	20
Plunge Milling 2	3000	0.1	20
Inclined Surface 1	4000	0.1	5
Inclined Surface 2	7000	0.1	5
3-Axis Free Form	4000	0.1	0.6-6
5-Axis Airfoil	4000	0.1	0.25-4

Table 6.2: Specifications of the tool used in verification experiments

Tool Type	Nominal Tool Diameter	Nominal Helix Angle	Nominal Normal Rake Angle	Nominal Normal Clearance Angle	Flute Length	Max. Allowable feed by Sandvik Coromant	Drilling Function
2-fluted Solid Ball-end Cutter (Sandvik Coromant: R216.42-16030-AK26A H10F)	ϕ16mm	30^0	12^0	5^0	26 mm	0.161 feed/rev/tooth	Yes

All measurements were done on an initially flat surface in dry cutting conditions and measurement data was collected using the data acquisition module MALDAQ of the machining engineering software CutPro®. Three-component Kistler 9257B table type, and two-component Kistler 9125-001 rotary dynamometers were used for cutting force measurements in three-axis (including plunge milling) and five-axis cutting experiments, respectively. In the following sections, for each test type, the finished workpiece surface is shown along with the machined surface generated in Computer aided Manufacturing (CAM) environment using the commercial software NX 7.5®.

In cutting force simulations, the overall algorithm outlined in Figure 4.26 in Section 4.5 was followed by applying the orthogonal to oblique transformation method.

6.2 Exprimental Results

6.2.1 Plunge Milling Experiments

The purpose for plunging experiments was to check the model validation in pure vertical feed conditions. In order to obtain a steady cut while plunging with a ball end mill, ball part of the tool has to engage with the workpiece from tool tip to ball-cylindrical part transition level. Once entire ball-part engages with the workpiece, engagement conditions do not change in the following feed movements of the cutter, and cylindrical part does not contribute to cutting. To make sure these conditions hold true, plunging was carried out for 20 mm depth which is lower than the flute length of the tool. As the cutter is not a pure plunging tool, the chip removal during drilling such a hole would be a problem and could cause tool breakage. In order to avoid this, half holes are drilled instead. Picture of the drilled half holes and their 3D CAD model are demonstrated in Figure 6.1. For the plunge milling tests parameters in Table 6.1, measured and simulated cutting forces in all three cartesian coordinates of the machine tool are compared in Figure 6.2 and Figure 6.3.

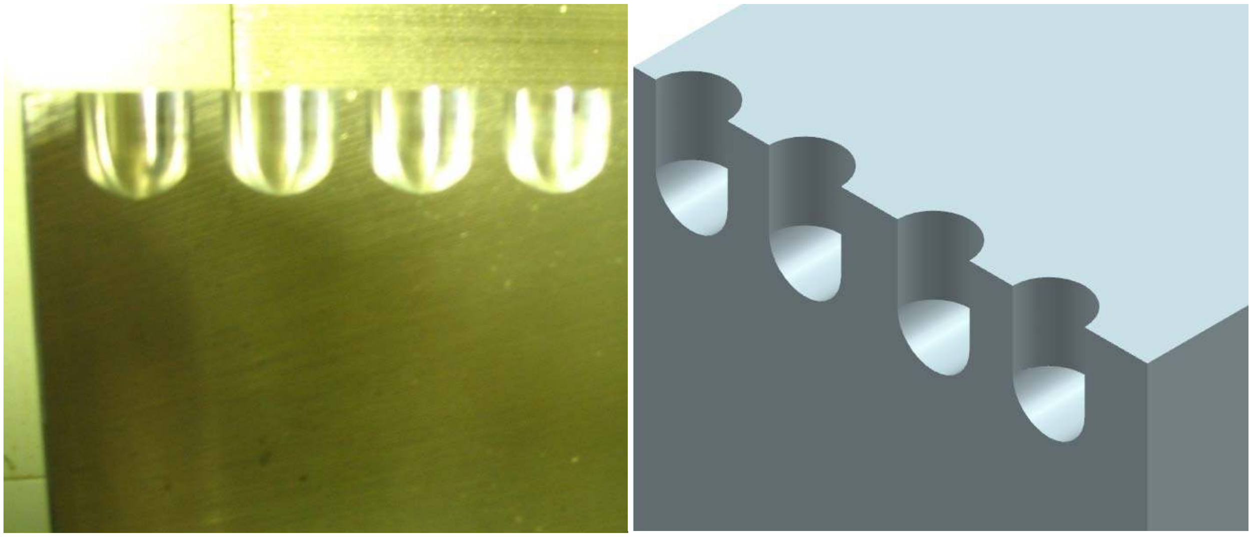

Figure 6.1: Drilling test workpiece (left) and its 3D CAD model (right)

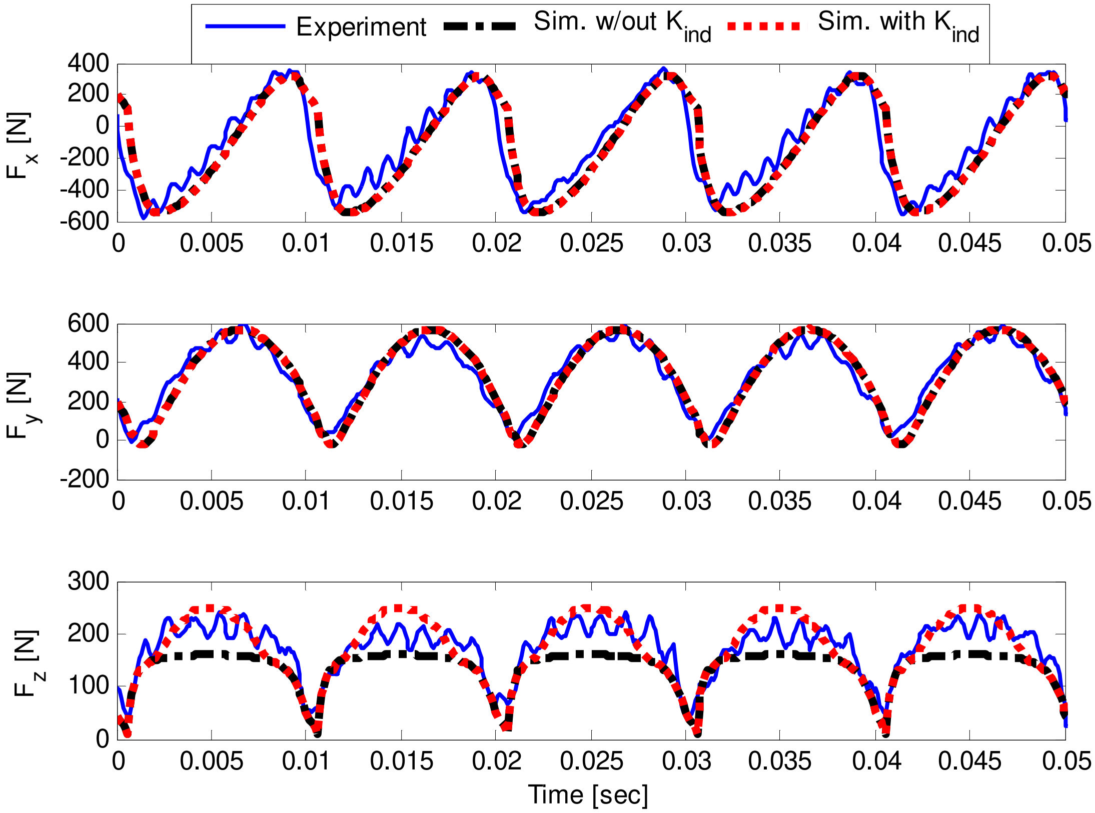

Figure 6.2: Comparison of experimental and predicted cutting forces in the first drilling experiment for; n=3000 rpm, $f = 0.04$ mm/rev, half hole 20 mm in depth, AL7050 workpiece

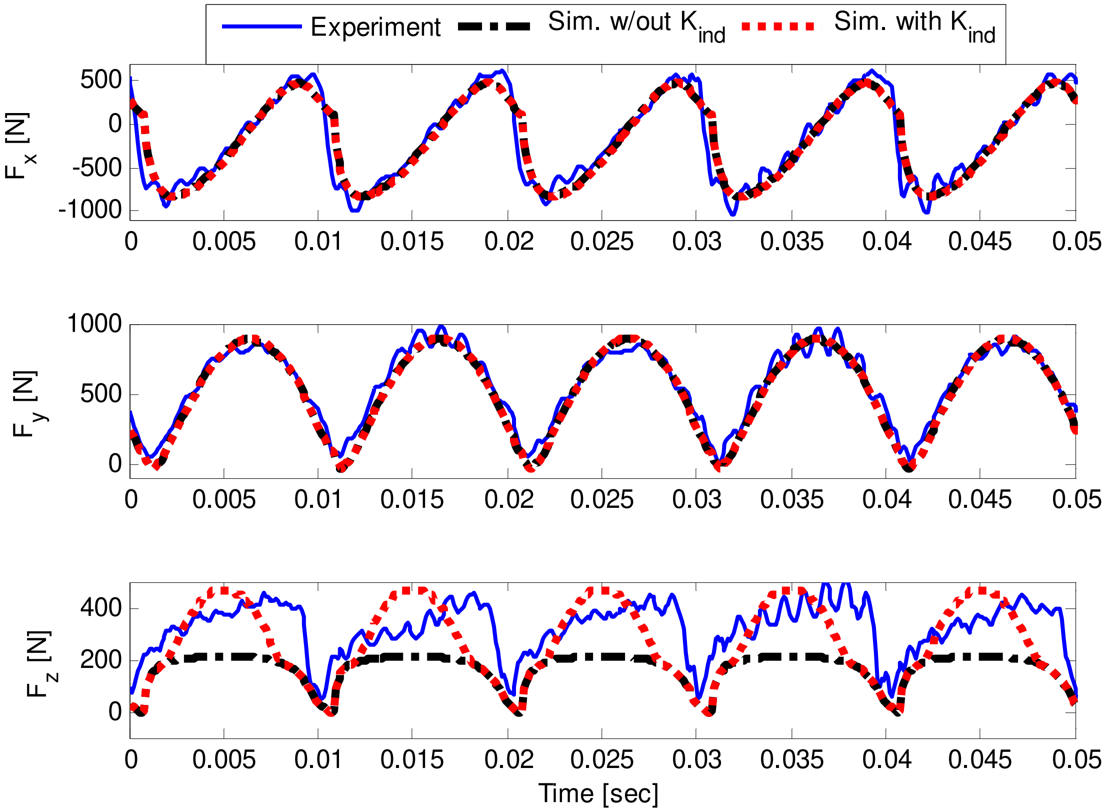

Figure 6.3: Comparison of experimental and predicted cutting forces in the second drilling experiment for; n=3000 rpm, f = 0.1 mm/rev, half hole 20 mm in depth, AL7050 workpiece

As seen from Figure 6.2 and Figure 6.3, the proposed ball-end milling cutting force prediction model with indentation model does not affect forces in x-y plane where tangential cutting force is dominant; however the prediction in z-direction where radial force is dominant towards the tool tip is improved by 14% and the average error in this direction becomes 13%.

6.2.2 Three-Axis Inclined Surface Experiments

The purpose for inclined surface experiments was to check the model validation in partially horizontal and downward feed conditions since this is essential for many industrial free-form machining applications.

Downward direction inclined surface ball-end milling experiments which were also used at problem identification stage were conducted since they are the simplest ball-end milling cases experiencing the indentation effect. As shown in Figure 6.4, the machine tool table on which the workpiece is mounted was tilted and the cutter was commanded to cut initially flat workpiece surface. The simulation of the cutting process in CAM environment is also shown in Figure 6.4.

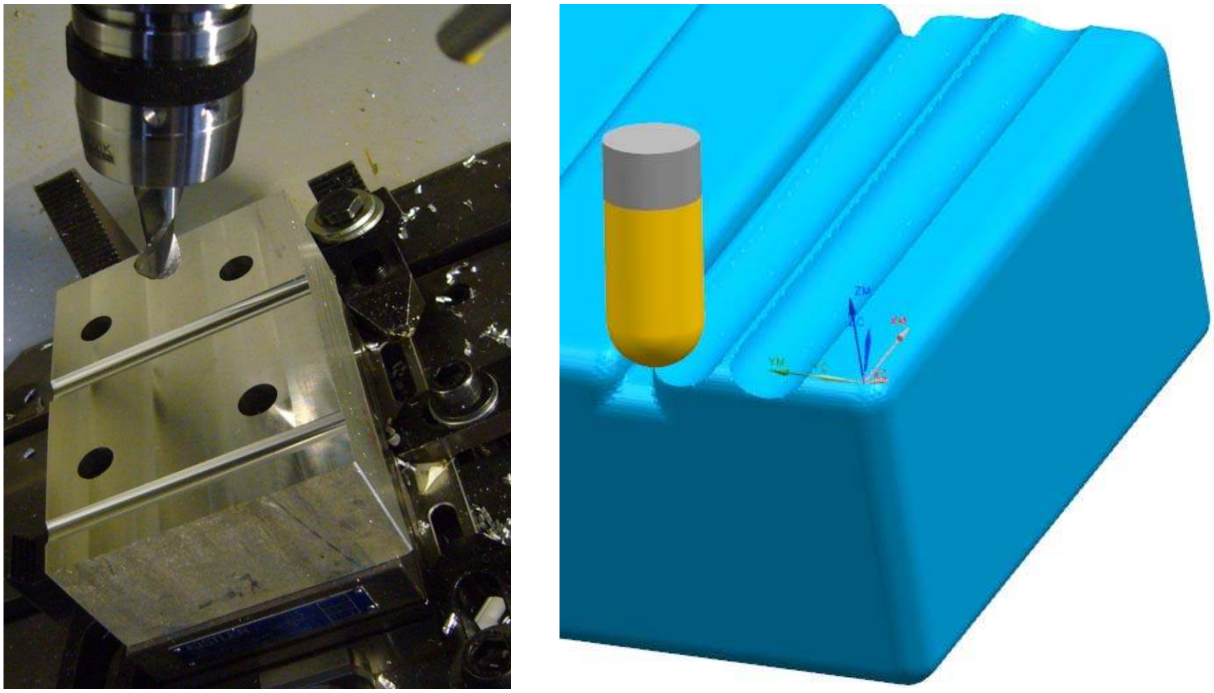

Figure 6.4: Inclined plane test surface and workpiece (left), and CAM model of cutting (right)

Measured and simulated cutting forces in all three principal directions of the machine tool are compared for two different surface inclination angles and results are presented in Figure 6.5 and Figure 6.6, accordingly.

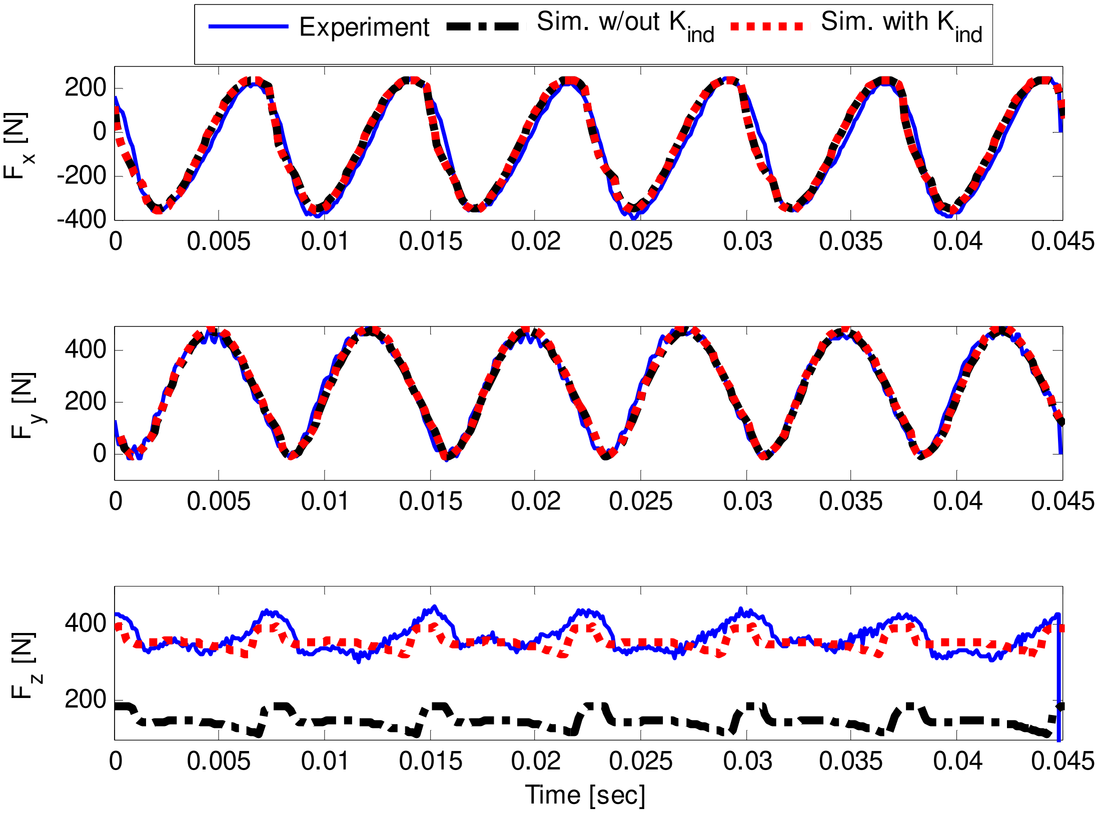

Figure 6.5: Comparison of experimental and predicted cutting forces for; n=4000 rpm, $\alpha = 15^0$ $f = 0.1$ mm/rev/tooth, $a_p = 5$ mm, AL7050 workpiece

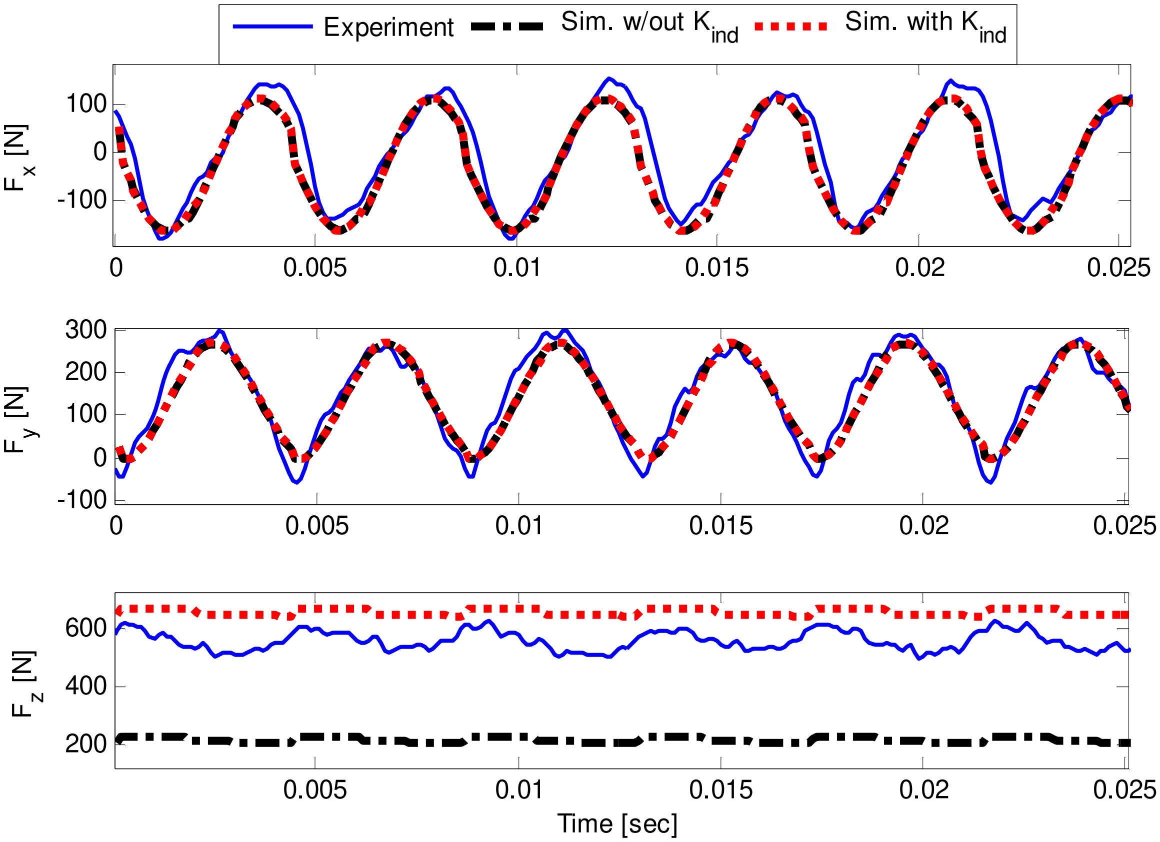

Figure 6.6: Comparison of experimental and predicted cutting forces for; n=7000 rpm, $\alpha = 30^0$ $f = 0.1$ mm/rev/tooth, $a_p = 5$ mm, AL7050 workpiece

As observed from Figure 6.5 and Figure 6.6, the proposed ball-end milling cutting force prediction model behaves same as plunge milling experiments both in x-y plane and z-direction. The error between experimental and predicted force in z-direction is more than 50% when indentation effect is ignored; however this error becomes less than 10% while indentation forces are taken into account.

6.2.3 Three-Axis Free-Form Surface Experiment

Another set of three-axis ball-end milling experiments have been conducted on a free-form surface which is composed of several inclined sections for roughing operation. Since the surface has several upward and downward inclined segments, a three-axis toolpath was generated using NX 7.5® for 4000 rpm spindle speed, 0.1 mm/rev/tooth feed per tooth, and 6 mm maximum axial depth of cut. The actual cut surface and related CAM surface are demonstrated in Figure 6.7. Free-form shape of the surface led to varying local surface inclination angle between 5^0 and 33^0 along the toolpath.

In order to simulate the cutting forces for varying immersion and tool positions along the toolpath, tool-workpiece engagements (TWEs) were extracted from MACHpro-Virtual Machining System following the procedure in Figure 3.4 in Section 3.2.2. In order to capture true tool-workpiece intersections the sampling distance was selected as 1 mm, which in turn generated 1398 map points. Due to the nature of the surface, (TWEs) also continuously varied along the path and led to random engagement profiles that have different engagement angles $(\phi_{st}$ and $\phi_{ex})$ along tool axis as exemplified in Figure 6.8.

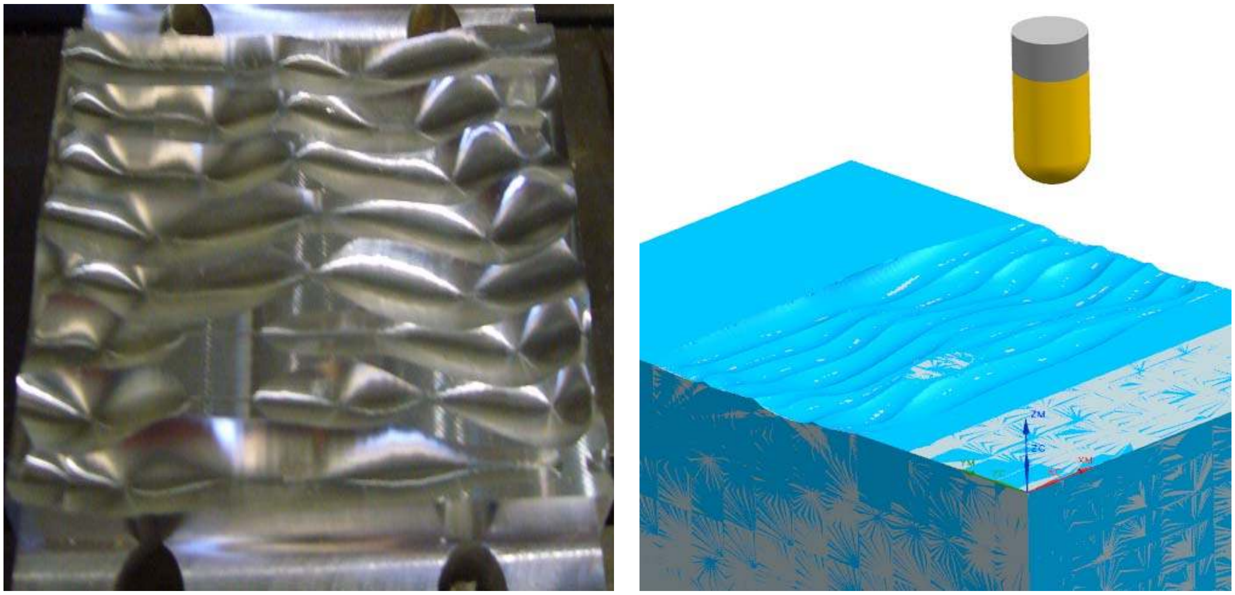

Figure 6.7: Three-axis free-form surface cutting test workpiece (left), and CAM model of cutting (right)

Measured and simulated cutting forces in three cartesian coordinates of the machine tool are compared in Figure 6.9, and a detailed comparison plot for cutting force in z-direction is presented in Figure 6.10.

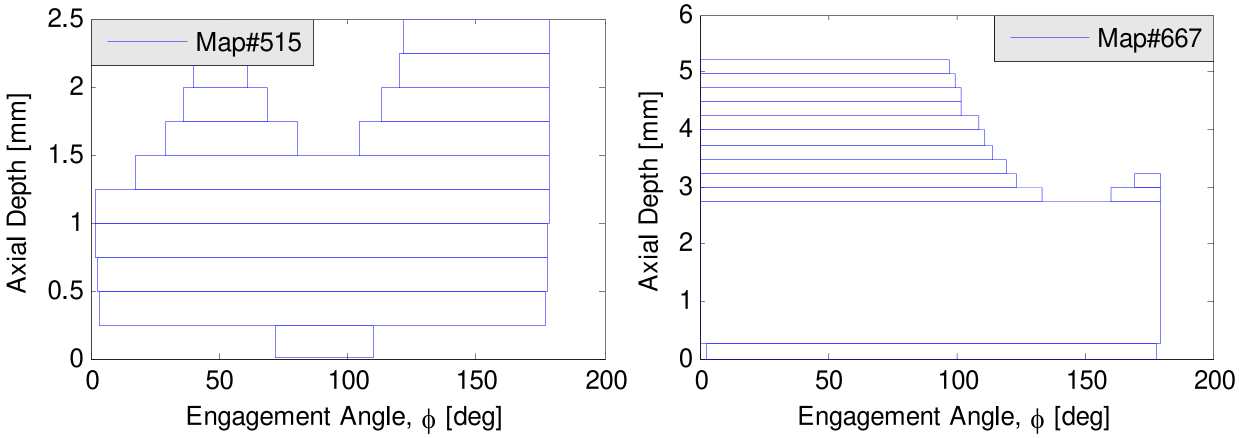

Figure 6.8: Sample 2D engagement maps for three-axis free-form surface test

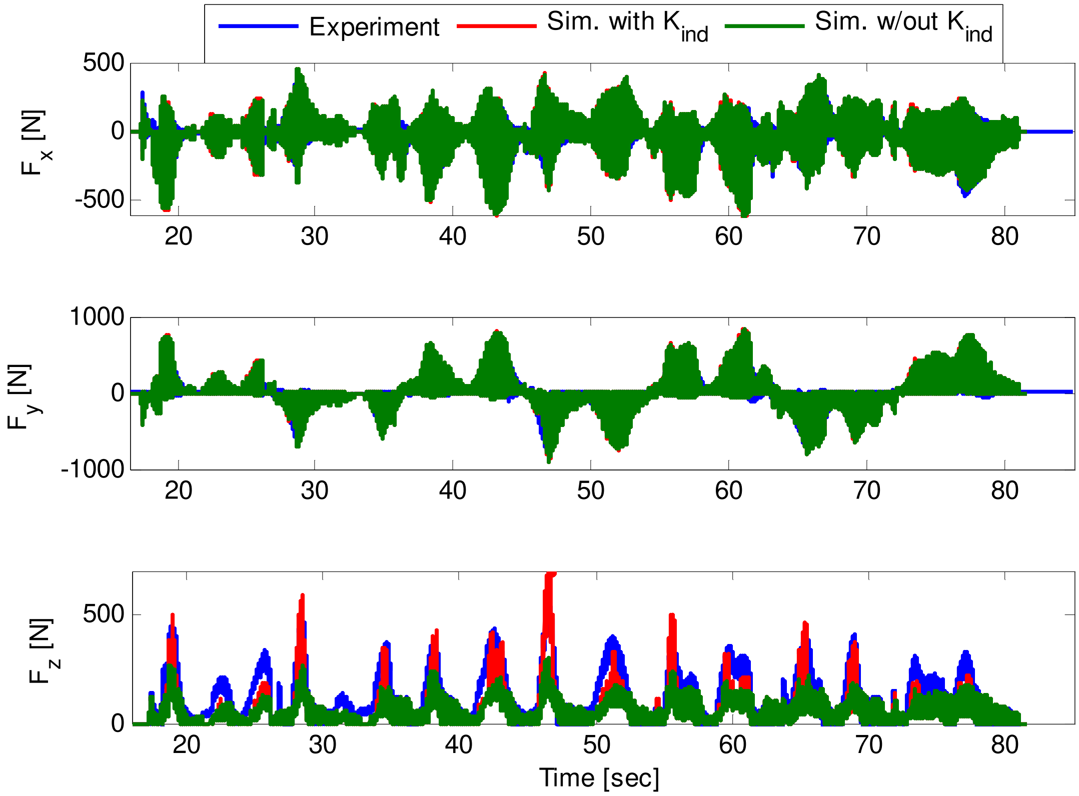

Figure 6.9: Comparison of experimental and predicted cutting forces for; n=4000 rpm, $f = 0.1$ mm/rev/tooth, $(a_p)_{max} = 6$ mm, AL7050 workpiece

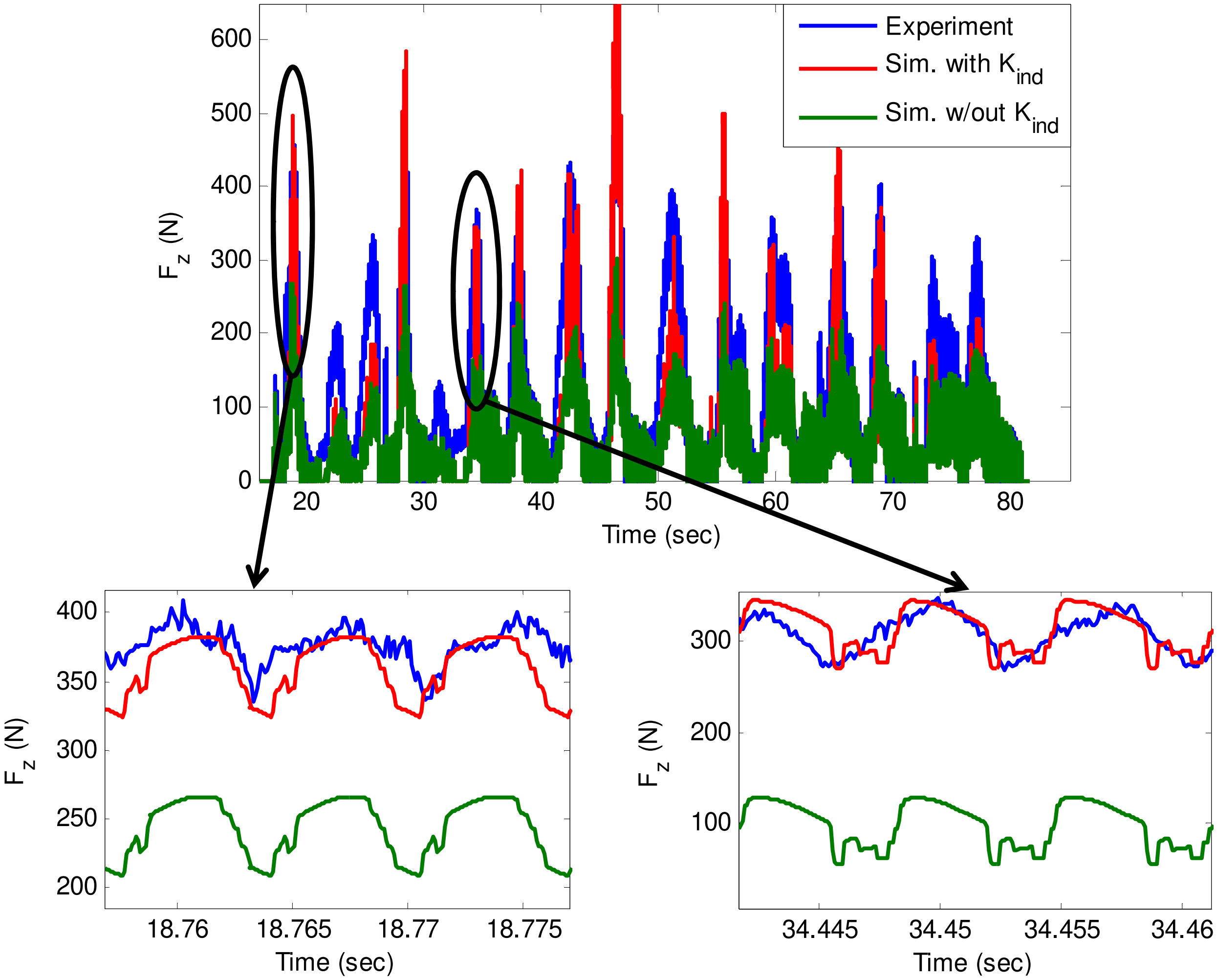

Figure 6.10: Comparison of experimental and predicted z-forces for; n=4000 rpm, $f = 0.1$ mm/rev/tooth, $\left(a_p\right)_{max}$ = 6 mm, AL7050 workpiece

Figure 6.9 and Figure 6.10 show that, the proposed indentation model has no effect on the forces in x and y directions while improving the predictions in z-direction by 35% in the presence of indentation.

6.2.4 Five-Axis Free-Form Surface (Airfoil) Experiment

Last set of experiments have been conducted on an airfoil shape surface which provides a smooth change in tool orientation for a five-axis toolpath. The purpose of the experiment was to check the indentation detection capability of the model in five-axis cutting conditions. A five-axis toolpath was generated using NX 7.5® for 4000 rpm spindle speed, 0.1 mm/rev/tooth feed per tooth, and 4 mm maximum axial depth of cut by defining tool orientation relative to airfoil surface. The generated toolpath led to varying tool orientation angles as shown in Figure 6.11. The actual cut surface and related CAM surface are shown in Figure 6.12.

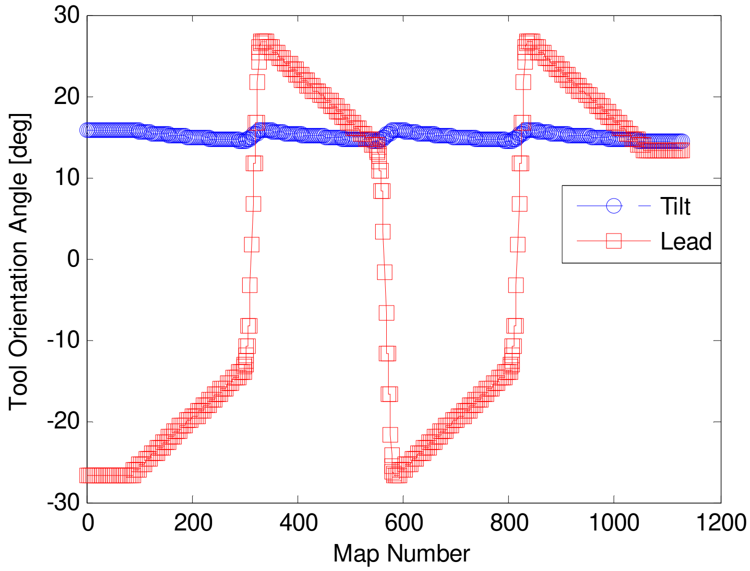

Figure 6.11: Variation of tool orientation angles along the toolpath

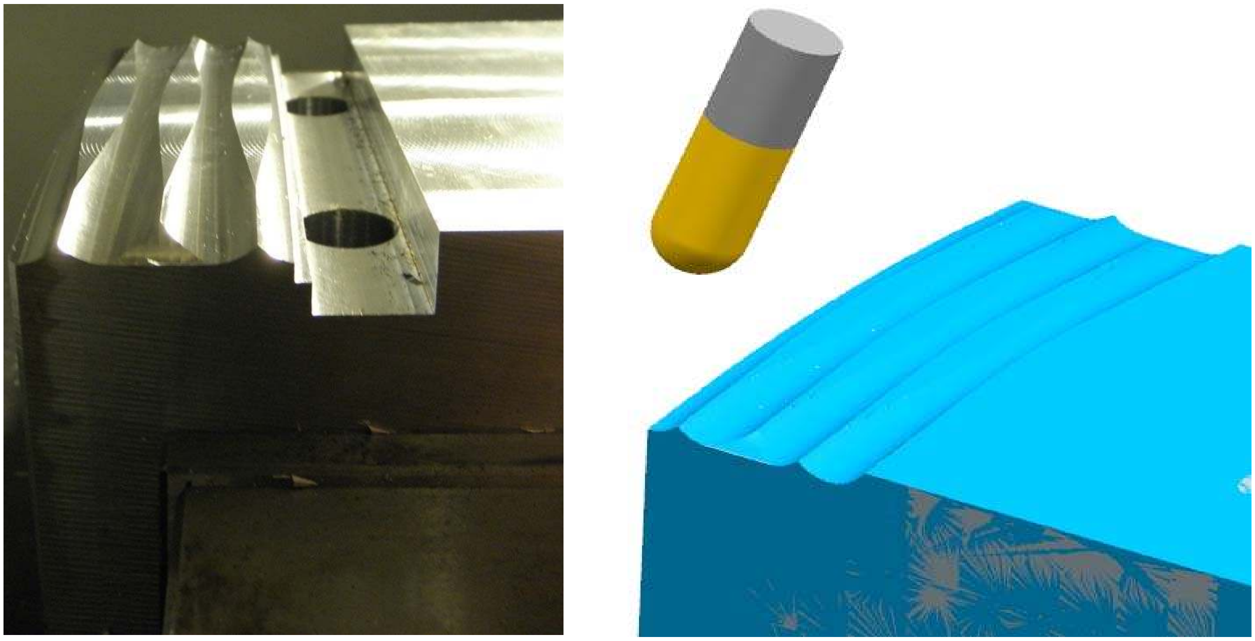

Figure 6.12: Five-axis airfoil surface cutting test workpiece (left), and CAM model of cutting (right)

TWEs were extracted from MACHpro-Virtual Machining System with a 0.5 mm sampling distance, which in turn generated 1129 map points. Two of these engagement maps are shown in Figure 6.13 as example.

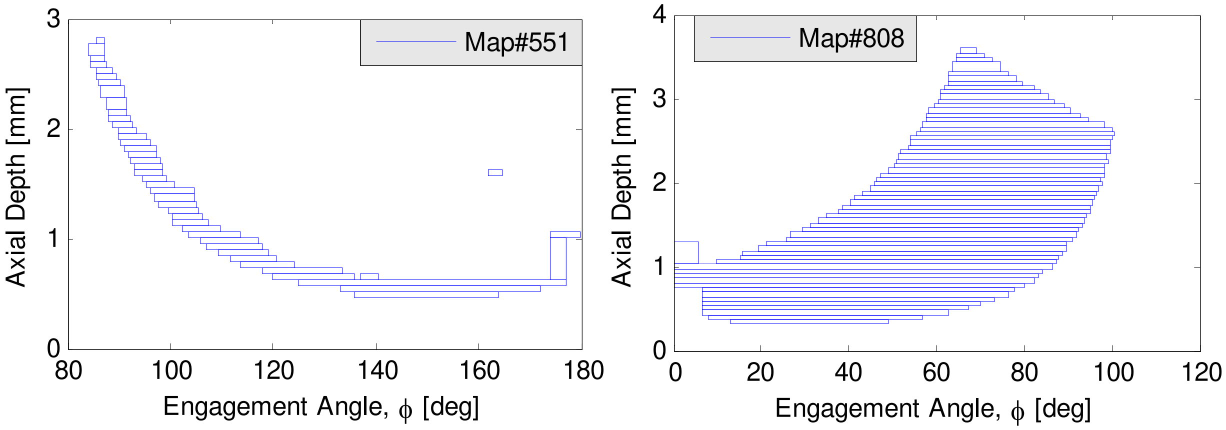

Figure 6.13: Sample 2D engagement maps for five-axis airfoil surface test

Measured and simulated cutting forces in z-direction of the machine tool are compared in Figure 6.14 where each pass of the toolpath is compared seperately as experimental and simulated process times did not match. This can be attributed to drive dynamics of the machine tool which are not included in force prediction simulations. The benefit of pass by pass comparison is that, the toolpath was generated in such a way that the tool tip is completely out of cut (no indentation condition) in the last pass to check the reaction of the model to the transition from cutting with indentation to without indentation conditions. As observed from the last plot of Figure 6.14, the prediction with K_{ind} gives the same results as without K_{ind} simulation for no indentation conditions.

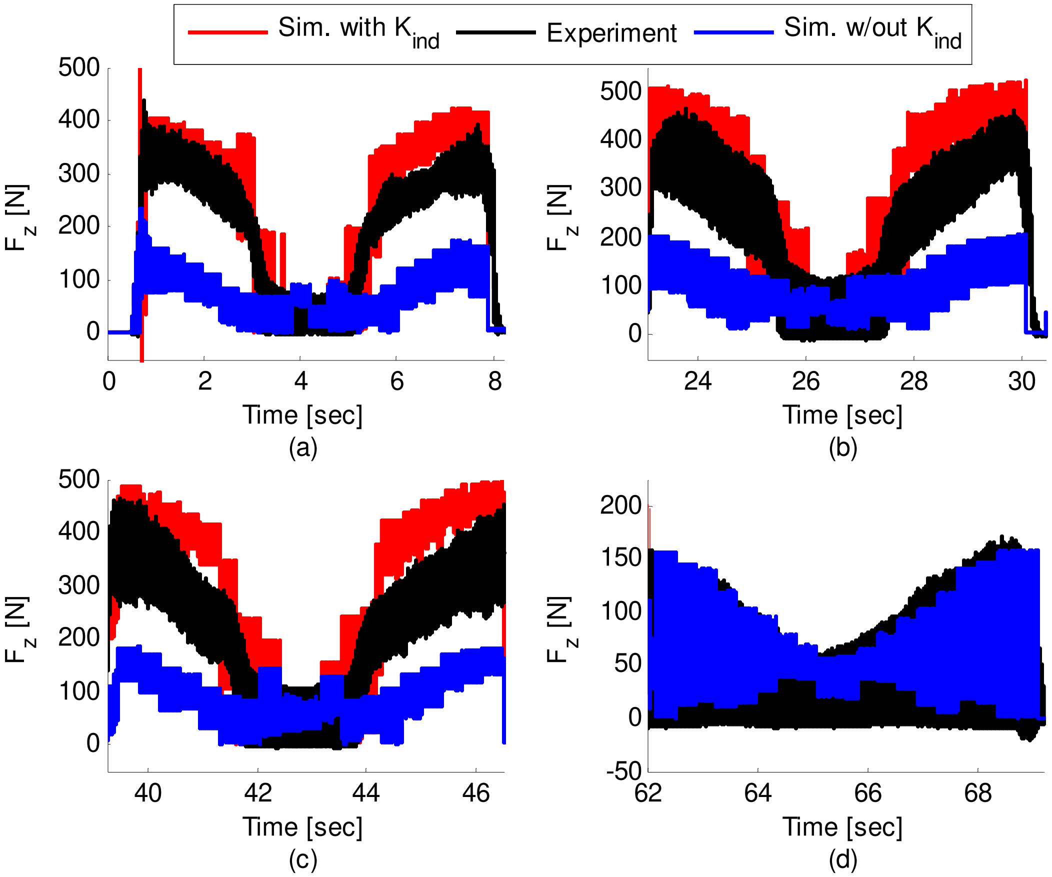

Figure 6.14: Comparison of experimental and predicted cutting forces for; **(a)** first pass **(b)** second pass **(c)** third pass **(d)** fourth pass, for; n=4000 rpm, $f =$ 0.1 mm/rev/tooth, $(a_p)_{max} = 4$ mm, AL7050 workpiece

Comparisons of measured and simulated cutting forces for all experiments showed that, predictions of the proposed cutting force prediction model agree well with experimentally measured forces in horizontal directions (x,y) with and without considering the indentation effect. However, the prediction of the axial (z) cutting force component is quite poor in presence of indentation unless the proposed indentation model is used.

The comparison results of measured and simulated z-forces for all verification experiments are summarized in Table 6.3 by average absolute error at indentation occurring regions.

Table 6.3: Summary of verification experiments results for z-forces

Experiment Name	**Average Absolute Error Without** $\mathrm{K}_{\mathrm{ind}}$	**Average Absolute Error With** $\mathrm{K}_{\mathrm{ind}}$
Plunge Milling 1	27%	13%
Plunge Milling 2	33%	18%
Inclined Surface 1	52%	8.5%
Inclined Surface 2	62%	9%
3-Axis Free Form	53%	18%
5-Axis Airfoil	53%	25%

Regarding the error values for all experiments, it can be said that the cutting force prediction in presence of indentation is improved by newly introduced ball-end milling mechanics model. Although the error value is different for distinct set of experiments, it ranges from 8% to 18% except for five-axis airfoil experiment. The increased error may be partially attributed to measurement equipment (rotary dynamometer), increased temperature effect in indentation region and error introduced by tool-workpiece engagements (TWEs).

Mostly the proposed model over-predicts the experimental forces within an error band (8-18%). This might have resulted from overestimation of material dependent parameters $\left(E,\sigma_Y\right)$ in the model; in other words underestimation of the temperature rise in the indentation region. The workpiece temperature calculation method which was adapted from orthogonal cutting for sharp edge tools automatically eliminates the friction and related heat generation around the edge radius of actual cutting edge.

Engagement conditions for three-axis free-form and five-axis airfoil cutting experiments were extracted from MACHpro/VeriCut®; however for plunge milling and inclined surface experiments engagements were calculated analytically as they have relatively simple tool-workpiece intersections. Even though MACHpro/VeriCut® provided pretty good engagement map information for three-axis, its output included some noise for the five-axis experiment. This might have caused the error in force prediction to increase.

6.3 Summary

In this chapter, verification of the proposed ball-end milling mechanics model is presented via plunging, three-axis inclined and free-form surfaces, and five-axis airfoil experiment with ball-end cutter. Tests were designed to cover a range of indentation cases from the simplest to very complex indentation mechanisms. It is observed that, the proposed force prediction model reduces the error in prediction of z-forces significantly. The thesis is ended with the concluding remarks, contributions of this study and future research directions in next chapter.

7 Conclusions

The improved ball-end milling force model is required to simulate the process accurately and improve the productivity in machining of parts with free-form surfaces. In this thesis, three and five-axis mechanics of ball-end milling are studied. Indentation free mechanics of three and five-axis ball-end milling are mainly adapted from [12] and [26]. The generic chip thickness calculation method introduced in [45] is extended to five-axis ball-end milling. Existence of cutting edge indentation problem is validated through the inclined surface cutting tests. The physical reason behind the tool penetration phenomenon is investigated.

A novel analytical indentation force calculation and detection model has been developed by utilizing the geometrical similarity between the cutting edge element and punch or wedge shape indenters. The model uses the properties of the work material and cutting edge geometry as inputs. The model has the ability to identify the plastic and elastic contact regions, which in turn leads to plastic and elastic contact pressure distributions. Also, generalized model is valid for all cutting edge geometries including positive and negative rake angles.

The effect of temperature on mechanical properties of the work material is investigated as well by defining two main heat sources for the work material; shearing and cutting edge indentation. The contribution of shearing is included in analytical indentation force calculation method by implementing the approach of [52] into ball-end milling.

Cutting edge indentation mechanics is also studied through finite element modeling (FEM) for various combinations of cutting edge geometries and indentation depths. Under the assumption of elastic-perfectly plastic material behavior for the work material, the FE model used in this study can be employed to obtain the constant quantifying the magnitude of plastic contact pressure for any kind of cutting edge and material combinations just by changing the geometry and material dependent parameters. Since a single material type namely AL7050 is used in this thesis, results are reported for this material only.

The proposed analytical indentation force prediction model has been experimentally verified through plunge, three-axis inclined surface, three-axis free-form surface, and five-axis milling experiments. The comparison between the experimental and simulated cutting forces in axial (z) direction show the prediction error is reduced noticeably.

The main contributions of this thesis can be summarized as follows:

- A comprehensive cutting edge indentation model which is capable of identifying indentation conditions and calculating related forces is developed both for three and five-axis ball-end milling applications using the punch and wedge shape indenter geometries. As opposed to the reported studies in the literature, the indentation problem is modeled and solved analytically.
- The cutting tool indentation, which is specific to the cutters that have a zero radius at the tool tip such as ball-end cutters, is defined. The effect of indentation on ball-end milling mechanics is introduced with physical reasoning for the first time in ball-end milling literature.
- A general finite element (FE) model for cutting edge indentation is developed. The FE model can either be directly used to obtain indentation force/pressure, or, as in this thesis, be used as a calibration tool to obtain the constant (*C*) quantifying the plastic contact pressure for any kind of material.

Currently, the cutting edge indentation model only covers the penetration related forces, and does not explain what happens to the material being spread (extruded) during penetration process. It can be either left on the workpiece surface as a burr, or it is pushed up in axial direction and removed by upper portions of the cutting flute. When this is the case, the chip thickness at these higher regions of the flute might increase; but this is not included in the model. Moreover, depending on the type of the work material, indentation can cause material pile-up or sink-in around the penetration region. Again the model does not consider this phenomenon in indentation geometry calculations.

Although the base model for analytical prediction of the additional forces in tool z-direction resulting from the cutting edge indentation is developed and presented in this study, there is still some room for further improvement. Since temperature dependent mechanical properties of the work material are employed in the model, the accuracy of the predictions can be enhanced by integrating an advanced temperature prediction model for ball-end milling into the proposed analytical indentation model.

As shown in Chapter 6, the model needs to be verified for more complex free-form surfaces with five-axis toolpaths experienced in industry. Also, the proposed model can be applied to chatter stability predictions at low speeds that cause tool flank face to penetrate into the wavy workpiece surface, which is called “process damping effect”. For that case, the amplitude of the waves on the workpiece surface has to be given to the model as an input to evaluate the indentation depth. In addition, the wavelength of the vibrations imprinted on the workpiece surface needs to be known in order to check multiple contacts at the interface of the flank face and the workpiece.

Bibliography

[1] B.U. Guzel, I. Lazoglu, An Enhanced Force Model for Sculptured Surface Machining, Machining Science and Technology, 8 (2004) 431-448.

[2] M. Fontaine, A. Devillez, A. Moufki, D. Dudzinski, Predictive force model for ball-end milling and experimental validation with a wavelike form machining test, International Journal of Machine Tools and Manufacture, 46 (2006) 367-380.

[3] N. Zeroudi, M. Fontaine, K. Necib, Prediction of cutting forces in 3-axes milling of sculptured surfaces directly from CAM tool path, Journal of Intelligent Manufacturing, (2010) 1-15.

[4] A. Azeem, H.-Y. Feng, L. Wang, Simplified and efficient calibration of a mechanistic cutting force model for ball-end milling, International Journal of Machine Tools and Manufacture, 44 (2004) 291-298.

[5] C.-L. Tsai, Y.-S. Liao, Cutting force prediction in ball-end milling with inclined feed by means of geometrical analysis, The International Journal of Advanced Manufacturing Technology, 46 (2008) 529-541.

[6] C.-L. Tsai, Y.-S. Liao, Cutting force prediction in ball-end milling with inclined feed by means of geometrical analysis, The International Journal of Advanced Manufacturing Technology, 46 (2010) 529-541.

[7] S.D. Merdol, Virtual Three-Axis Milling Process Simulation and Optimization, PhD Thesis in The University of British Columbia, 2008.

[8] Y. Altintas, Manufacturing Automation : Metal Cutting Mechanics, machine Tool Vibrations and CNC Design, Cambridge University Press, New York, 2000.

[9] A.J.P. Sabberwal, Chip section and cutting force during the milling operation, Annals of CIRP, 10 (1961) 197-203.

[10] E.J.A. Armarego, C.J. Epp, An investigation of zero helix peripheral up-milling, International Journal of Machine Tool Design and Research, 10 (1970) 273-291.

[11] E. Budak, Y. Altintas, E.J.A. Armarego, Prediction of Milling Force Coefficients From Orthogonal Cutting Data, Journal of Manufacturing Science and Engineering, 118 (1996) 216-216.

[12] P. Lee, Y. Altintas, Prediction of ball-end milling forces from orthogonal cutting data, International Journal of Machine Tools and Manufacture, 36 (1996) 1059-1072.

[13] S. Engin, Mechanics and dynamics of general milling cutters. Part I: helical end mills, International Journal of Machine Tools and Manufacture, 41 (2001) 2195-2212.

[14] M.E. Martelotti, An analysis of the milling process, Transactions of ASME, 63 (1941) 677-700.

[15] H.-Y. Feng, C.-H. Menq, The prediction of cutting forces in the ball-end milling process I. Model formulation and model building procedure, International Journal of Machine Tools and Manufacture, 34 (1994) 697-710.

[16] H.-Y. Feng, C.-H. Menq, The prediction of cutting forces in the ball-end milling process II. Cut geometry analysis and model verification, International Journal of Machine Tools and Manufacture, 34 (1994) 711-719.

[17] H.-Y. Feng, N. Su, A mechanistic cutting force model for 3D ball-end milling, Transactions of ASME, 123 (2001) 23-29.

[18] B.W. Ikua, H. Tanaka, F. Obata, S. Sakamoto, Prediction of cutting forces and machining error in ball end milling of curved surfaces -I theoretical analysis, Precision Engineering, 25 (2001) 266-273.

[19] B.W. Ikua, H. Tanaka, F. Obata, S. Sakamoto, T. Kishi, T. Ishii, Prediction of cutting forces and machining error in ball end milling of curved surfaces -II experimental verification, Precision Engineering, 26 (2002) 69-82.

[20] M. Fontaine, A. Moufki, A. Devillez, D. Dudzinski, Modelling of cutting forces in ball-end milling with tool surface inclination: Part I: Predictive force model and experimental validation, Journal of Materials Processing Technology, 189 (2007) 73-84.

[21] A. Lamikiz, L.N. Lapez de Lacalle, J.A. Sanchez, M.A. Salgado, Cutting force estimation in sculptured surface milling, International Journal of Machine Tools and Manufacture, 44 (2004) 1511-1526.

[22] Y. Sun, F. Ren, D. Guo, Z. Jia, Estimation and experimental validation of cutting forces in ball-end milling of sculptured surfaces, International Journal of Machine Tools and Manufacture, 49 (2009) 1238-1244.

[23] P.A. Clayton, M.A. Elbestawi, T. El-Wardany, D. Viens, A mechanistic force model of the 5-axis milling process, Manufacturing in Engineering Division, 11 (2000) 979-987.

[24] B.K. Fussell, R.B. Jerard, J.G. Hemmett, Modeling of cutting geometry and forces for 5-axis sculptured surface machining, Computer-Aided Design, 35 (2003) 333-346.

[25] E. Ozturk, E. Budak, MODELING OF 5-AXIS MILLING PROCESSES, Machining Science and Technology, 11 (2007) 287-311.

[26] W.B. Ferry, Virtual Five-Axis Flank Milling of Jet Engine Impellers, in, The University of British Columbia, Vancouver, 2008.

[27] G. Dongming, R. Fei, S. Yuwen, An Approach to Modeling Cutting Forces in Five-Axis Ball-End Milling of Curved Geometries Based on Tool Motion Analysis, Journal of Manufacturing Science and Engineering, 132 (2010) 041004-041008.

[28] Y. Boz, H. Erdim, I. Lazoglu, Modeling Cutting Forces for 5-Axis Machining of Sculptured Surface, in: 2nd International Conference, Process machine Interactions, Vancouver, 2010.

[29] ISO, International Standards 6506-1 : Metallic materials - Brinell hardness test - Part 1: Test method, Part 2: Verification and calibration of testing in, 2005.

[30] K.L. Johnson, Contact Mechanics, First Edition ed., Cambridge University Press, 1985.

[31] J. Jaeger, New analytical solutions for a flat rounded punch compared with FEM Methods, WIT Press, 2001.

[32] J. Jaeger, New analytical and numerical results for two-dimensional contact profiles, International Journal of Solids and Structures, 39 (2002) 959-972.

[33] I.G. Goryacheva, H. Murthy, T.N. Farris, Contact problem with partial slip for the inclined punch with rounded edges, International Journal of Fatigue, 24 (2002) 1191-1201.

[34] A. Sackfield, D. Dini, D.A. Hills, The finite and semi-infinite tilted, flat but rounded punch, International Journal of Solids and Structures, 42 (2005) 4988-5009.

[35] C.E. Truman, A. Sackfield, D.A. Hills, Contact mechanics of wedge and cone indenters, International Journal of Mechanical Sciences, 37 (1995) 261-275.

[36] M. Ciavarella, D.A. Hills, G. Monno, Contact problems for a wedge with rounded apex, International Journal of Mechanical Sciences, 40 (1998) 977-988.

[37] A. Sackfield, D. Dini, D.A. Hills, The tilted shallow wedge problem, European Journal of Mechanics - A/Solids, 24 (2005) 919-928.

[38] D. Dini, J.R. Barber, C.M. Churchman, A. Sackfield, D.A. Hills, The application of asymptotic solutions to contact problems characterised by logarithmic singularities, European Journal of Mechanics - A/Solids, 27 (2008) 847-858.

[39] J.W. Sutherland, R.E. Devor, An improved method for cutting force and surface error prediction in flexible and milling systems, Transactions of ASME, Journal of Engineering for Industry, 108 (1986) 269-279.

[40] A.E. Bayoumi, G. Yucesan, L.A. Kendall, An analytic mechanistic cutting force model for milling operations:a theory and methodology, Transactions of ASME, 116 (1994) 324-330.

[41] T.C. Ramaraj, E. Eleftheriou, Analysisi of the mechanics of machining with tapered end milling cutters, Transactions of ASME, 116 (1994) 398-404.

[42] I. Lazoglu, S.Y. Liang, ANALYTICAL MODELING OF FORCE SYSTEM IN BALL-END MILLING, Machining Science and Technology, 1 (1997) 219-234.

[43] ISO, International Standards 3002-1 : Basic quantities in cutting and grinding - Part 1 in, ISO, Geneva, 1992.

[44] E.J.A. Armarego, R.H. Brown, The Machining of Metals, Prentice-Hall, Englewood Cliffs, 1969.

[45] S. Merdol, Y. Altintas, Virtual cutting and optimization of three-axis milling processes, International Journal of Machine Tools and Manufacture, 48 (2008) 1063-1071.

[46] J. Gradisek, M. Kalveram, K. Weinert, Mechanistic identification of specific force coefficients for a general end mill, International Journal of Machine Tools and Manufacture, 44 (2004) 401-414.

[47] G.V. Stabler, The chip flow law and its consequences, Advances in Machine tool Design and Research, (1964) 243-251.

[48] G.M.L. Gladwell, Contact problems in the classical theory of elasticity / by G.M.L. Gladwell, Sijthoff & Noordhoff, Alphen aan den Rijn, The Netherlands :, 1980.

[49] W. Yu, Theoretical and Numerical Analysis of the Indentation of Elastic-Plastic and Creeping Solids, in, University of Wisconsin - Madison, 1995.

[50] L.M. Kachanov, Foundations of the theory of plasticity / L.M. Kachanov, North-Holland, Amsterdam :, 1971.

[51] M. Jin, I. Goto, T. Watanabe, J.-i. Kurosawa, M. Murakawa, Development of cBN ball-nosed end mill with newly designed cutting edge, Journal of Materials Processing Technology, 192-193 (2007) 48-54.

[52] R. Komanduri, Z.B. Hou, Thermal modeling of the metal cutting process: Part I: Temperature rise distribution due to shear plane heat source, International Journal of Mechanical Sciences, 42 (2000) 1715-1752.

[53] M. Kaymakci, Generalized Modeling of Metal Cutting Mechanics, in, The University of British Columbia, Vancouver, 2009.

[54] R. Kapoor, S. Nemat-Nasser, Determination of temperature rise during high strain rate deformation, Mechanics of Materials, 27 (1998) 1-12.

[55] A.K. Bhattacharya, W.D. Nix, Finite element simulation of indentation experiments, International Journal of Solids and Structures, 24 (1988) 881-891.

[56] K.R. Jayadevan, R. Narasimhan, Finite element simulation of wedge indentation, Computers &amp; Structures, 57 (1995) 915-927.

[57] C. Jacq, D. NeÌ lias, G. Lormand, D. Girodin, Development of a Three-Dimensional Semi-Analytical Elastic-Plastic Contact Code, Journal of Tribology, 124 (2002) 653-653.

[58] B. Taljat, Development of pile-up during spherical indentation of elastic?plastic solids, International Journal of Solids and Structures, 41 (2004) 3891-3904.

[59] R.L. Jackson, I. Green, A Finite Element Study of Elasto-Plastic Hemispherical Contact Against a Rigid Flat, Journal of Tribology, 127 (2005) 343-343.

[60] Sandvik, Coromant, General Milling Catalogue, in, 2011.

[61] Kennametal, Solid End-Milling Catalogue, in, 2011.

[62] M.N.A. Nasr, E.G. Ng, M.A. Elbestawi, Modelling the effects of tool-edge radius on residual stresses when orthogonal cutting AISI 316L, International Journal of Machine Tools and Manufacture, 47 (2007) 401-411.